University of California
Los Angeles

Lateral Quantum Dots for Quantum Information Processing

A dissertation submitted in partial satisfaction
of the requirements for the degree
Doctor of Philosophy in Physics

by

Matthew Gregory House

2012

Abstract of the Dissertation

Lateral Quantum Dots for Quantum Information Processing

by

Matthew Gregory House

Doctor of Philosophy in Physics

University of California, Los Angeles, 2012

Professor Hong Wen Jiang, Chair

The possibility of building a computer that takes advantage of the most subtle nature of quantum physics has been driving a lot of research in atomic and solid state physics for some time. It is still not clear what physical system or systems can be used for this purpose. One possibility that has been attracting significant attention from researchers is to use the spin state of an electron confined in a semiconductor quantum dot. The electron spin is magnetic in nature, so it naturally is well isolated from electrical fluctuations that can a loss of quantum coherence. It can also be manipulated electrically, by taking advantage of the exchange interaction. In this work we describe several experiments we have done to study the electron spin properties of lateral quantum dots. We have developed lateral quantum dot devices based on the silicon metal-oxide-semiconductor transistor, and studied the physics of electrons confined in these quantum dots. We measured the electron spin excited state lifetime, which was found to be as long as 30 ms at the lowest magnetic fields that we could measure. We fabricated and characterized a silicon double quantum dot. Using this double quantum dot design, we fabricated devices which combined a silicon double quantum dot with a superconducting microwave resonator. The microwave resonator was found to be sensitive to two-dimensional electrons in the transistor channel, which we measured and characterized.

We developed a new method for extracting information from random telegraph signals, which are produced when we observe thermal fluctuations of electrons in quantum dots. The new statistical method, based on the hidden Markov model, allows us to detect spin-dependent effects in such fluctuations even though we are not able to directly observe the electron spin. We use this analysis technique on data from two experiments involving gallium arsenide quantum dots and use it to measure spin-dependent tunneling rates. Our results advance the understanding of electron spin physics in lateral quantum dots, in silicon and in gallium arsenide.

The dissertation of Matthew Gregory House is approved.

Kang Wang

Karoly Holczer

Stuart Brown

Hong Wen Jiang, Committee Chair

University of California, Los Angeles

2012

For my parents John and Susan

Table of Contents

List of Figures

List of Tables

Acknowledgments

The most important ingredient of stardom is the rest of the team.

- J. R. Wooden

Success in any great endeavor is never an individual accomplishment. I am well aware that although my name is the only one that appears as author of this dissertation, the sum of others' contributions to it is actually greater than my own. I feel incredibly grateful to all those who have contributed to my research and to my education, only a fraction of which I can name here.

My advisor Hong Wen Jiang gave me a great opportunity to work in his lab and just the right amount of support and guidance, while also giving me freedom to pursue my own projects. It has been my pleasure to work for him.

I depended a lot on the other members of my lab, and this dissertation necessarily contains a lot of their work too. Ming Xiao developed the silicon MOSFET quantum dot devices that made most of my own research possible, and taught me most of what I know about them and how to study them. Giovanni Mazzeo went out of his way to teach me a lot of the basics of device fabrication and measurement techniques when I first came to work in the lab. It has also been a pleasure to work with Hong Pan and Xiaojie Hao; we have all consistently helped each other and made a good team.

The microwave resonator experiment was done in collaboration with Irfan Siddiqi and his research group at UC Berkeley. The original design for the resonator experiment was developed by Ofer Naaman. Andy Schmidt and Ned Henry also made important contributions.

I benefitted from discussing my work with any number of people in our research field, but especially Charlie Tahan, Rusko Ruskov, and Dimi Culcer. Several of the UCLA physics faculty gave me outstanding instruction, but I would like to mention Karoly Holczer especially who taught me condensed matter physics and microwave electronics topics that I applied

directly to my research.

Craig Reeves and his staff did a great job of keeping our facilities in good tune and our lab in the good graces of EHS, without which we could not have done any lab work at all. Likewise, the skill and professionalism of Harry Lockart and his staff at the physical sciences machine shop made my life easy when I needed custom parts.

Laura Griffin took my time away from writing this dissertation, and even when I was at my desk working on it she was constantly distracting my thoughts. For everything she did that hurt the final quality of this document, I thank her.

I could never name all of the teachers and colleagues over the years who have taught me, in science and otherwise, without whom I never would have reached this point. I am very grateful for all of them, but an outstanding few who went above and beyond their normal duties to encourage me and shape my path are Dean Mimmack, James Kroger, Vicente Honrubia, Jean-Noel LeBoeuf, and Paul Mountcastle.

My parents are the undoubtedly the two most important teachers I've had. Without the immeasurable gift of their love and support I would not be a scientist or anything else worthwhile.

Vita

1998–2001	Research Assistant UCLA School of Medicine, Los Angeles, California
2001	B.S. in Applied Mathematics with Specialization in Computing University of California, Los Angeles
2001–2005	Systems Engineer Xontech Inc. and Northrop Grumman Inc., Huntington Beach, California
2005–2008	Teaching Assistant UCLA Department of Physics and Astronomy
2006	M.S. in Physics University of California, Los Angeles
2008–2011	Graduate Student Researcher UCLA Department of Physics and Astronomy
2011–2012	UCLA Graduate Division Dissertation Year Fellowship University of California, Los Angeles

Publications

M. G. House, H. Pan, M. Xiao, and H. W. Jiang. (2011) *Non-equilibrium charge stability diagrams of a silicon double quantum dot.* Applied Physics Letters, **99**, 112116.

M. Xiao, M. G. House, and H. W. Jiang. (2010) *Parallel spin filling and energy spectroscopy in few-electron Si metal-on-semiconductor-based quantum dots.* Applied Physics Letters, **97**, 032103.

M. Xiao, M. G. House, and H. W. Jiang. (2010) *Measurement of the spin relaxation time of single electrons in a silicon metal-oxide-semiconductor-based quantum dot.* Physical Review Letters, **104** (9), 096801.

M. G. House, X. C. Zhang, and H. W. Jiang. (2009) *Analysis of electron tunneling events with the hidden Markov model.* Physical Review B, **80** (11), 113308.

M. G. House. (2008) *Analytic model for electrostatic fields in surface-electrode ion traps.* Physical Review A, **78** (3), 033402.

M. G. House and V. Honrubia. (2003) *Theoretical Models for the Mechanisms of Benign Paroxysmal Positional Vertigo.* Audiology and Neuro-Otology, **8** (2), 91-99. Erratum in: Audiology and Neuro-Otology, **8** (5), 303.

C. G. Hobbs, M. G. House, J. N. Leboeuf, J. M. Dawson, V. K. Decyk, and R. D. Sydora. (2001) *Effect of toroidal rotation on ion temperature gradient turbulence and resistive kink stability in a large aspect ratio tokamak.* Physics of Plasmas, **8** (11), 4849-4855.

V. Honrubia and M. G. House. (2001) *Mechanism of Posterior Semicircular Canal Stimulation in Patients with Benign Paroxysmal Positional Vertigo.* Acta Otolaryngologica, **121**, 234-240.

CHAPTER 1

Introduction

Make each day your masterpiece.

- J. R. Wooden

1.1 Background

Our studies of physics today are necessarily a continuation of the work of thousands upon thousands of physicists, natural philosophers, and ordinary people who have made and codified observations of the natural world around us for generations. Through the years the study of physics has evolved, becoming increasingly specialized and technologically challenging, but the fundamental desire to explain the world around us remains our driving motivation. As we gain more and more detailed knowledge, we study physical phenomena that are more subtle, more delicate, and more complex. The smallest physical systems can only be explained by the theory of quantum mechanics, with its sometimes strange and counterintuitive implications. Quantum mechanics has been vital to the development of modern chemistry and materials science, most notably being crucial to the vast technological advancement in semiconductor electronics over the past 70 years that has had an enormous impact on our society and culture. As our understanding of quantum physics advances, the level of detail in which we are able to study and manipulate tiny systems opens new avenues for research and technology.

The theory of quantum mechanics was originally developed in the early 20^{th} century, in response to what were at the time unusual observations about the nature of atoms and

their interaction with light. From the late 19^{th} century on there were clear indications that atoms did not radiate light as would be expected from the simplest extensions of classical electrodynamics. It was not until the 1920s that a clear picture of quantum mechanics emerged with a theory that explained the behavior of microscopic particles.

At about the same time, modern solid state physics was born when Max von Laue and collaborators first discovered in 1912 that crystalline solids diffract x-rays. Shortly after that William Henry Bragg and William Lawrence Bragg used x-ray diffraction to make important early advances in the understanding of the physical structure of crystals. For his efforts, Laue was awarded the 1914 Nobel Prize in Physics; the Braggs shared the 1915 Nobel Prize. Already as early as 1900 the Drude model of electronic conduction had been developed and could explain much about the behavior of electrical conduction in metals. But it turns out that, as in isolated atoms, many of the details of the behavior of solid state systems can only be understood in terms of quantum mechanics. Understanding the electronic properties of crystals had to wait for quantum mechanics to catch up. Only after the development of the Schrodinger wave function theory in 1926 could work move forward to explain the density of electronic states and their electrical and thermal conduction properties in metals, semiconductors, and insulators. In 1928 Bloch developed the wave theory of electrons in crystalline solids that underpins our understanding of the allowed states of electrons in solids and their conduction properties. From there the field of solid state electronics blossomed as many different types of materials could be studied and understood under the new theories. The success of the quantum theory of solids led directly to the demonstration of the first solid state transistor at Bell Labs in 1947, and to the semiconductor technology revolution which followed it. But for all of this success, commercial semiconductor technology today still does not make direct use of the most subtle and delicate aspect of quantum mechanical systems: the coherent evolution of quantum states.

Students of quantum mechanics are familiar with the fact that a particle's wavefunction has both an amplitude and a phase, and that two quantum states can be entangled so that they can no longer be thought of as independent objects. Although these aspects of

quantum mechanics are well known, they can be difficult to realize in practice because they are very sensitive to the influence of their surrounding environment. It is difficult to design an experiment in which a tiny quantum system can be manipulated yet simultaneously remain well isolated from any effects that are not under the control of the experimenter. This is especially true in solid state systems where the microscopic object being studied is surrounded by a solid which has many, many degrees of freedom with which it may interact. Generally there is a trade-off to be made because those systems which are well isolated from their environment are correspondingly difficult to deliberately manipulate. For example, the spin states of nuclei are coupled only very weakly to the electromagnetic field, so the interaction with the environment is very small, but because they have only weak interactions they can only be controlled at relatively slow rates, and it usually takes an ensemble of many spins to produce a net effect large enough to be detected, for example in a nuclear magnetic resonance (NMR) experiment. Other systems that are easier to work with cannot maintain quantum coherence over a useful period of time. Only recently has coherent manipulation of individual quantum systems in a solid state environment become feasible.

We are entering a new era in solid state physics and technology as we are gaining the ability to maintain and manipulate the quantum states of solid state particles and systems coherently. The major technological goal driving research in this direction is the possibility of using coherent systems to construct a *quantum information processor* or *quantum computer*. It has been shown theoretically that such a computer, which takes advantage of quantum coherent behavior, can perform certain calculations exponentially faster than one that relies only on incoherent states. But the difficulty of producing useful coherent states has left us with a challenge. It is not yet clear which type of quantum system (or systems) will serve well to represent information. Therefore to achieve the goal of realizing a quantum information processor we must study the physics of microscopic systems with potential to determine how well their quantum states can be controlled experimentally, and how well they maintain their quantum coherence.

This dissertation focuses on one particular way that quantum coherent behavior can be

realized and studied: by electrons trapped in quantum dots in a silicon crystal. Electrons trapped in sufficiently small potential wells have quantized energy levels, as well as other quantum degrees of freedom: the conduction band valley quantum number and spin, which we will discuss in more detail. It is the electron's spin state in particular that shows significant promise as a possible basis for studies of quantum coherence and demonstrations of a quantum information processing device, so that is where we have focused much of our research effort over the past few years. But we have not ignored other aspects of the physics of quantum dots, which are interesting for scientific reasons independent of any technological goal.

Regardless of the technological goals that give focus to our research the physics we study here is very much rooted in a fundamental question of quantum mechanics: how does the classical behavior of large systems emerge from the quantum mechanical world which we know exists at the smallest scales? Our understanding of how interactions between quantum systems and its environment lead to the loss of coherence has been advancing over the past decade but it cannot yet be said that we completely understand the "collapse of the wavefunction" in quantum systems. Research towards a quantum information processing system necessarily must probe that boundary between quantum and classical physics and help us to better understand how the classical world of our everyday experience emerges from the quantum world of microscopic systems. The combination of technological goals with fundamental scientific questions make this an exciting time for doing research in quantum mechanics.

1.2 Quantum information processing

To build a quantum information processing device (or quantum computer) we must first have a physical system which can store and represent information. The simplest possible system is a quantum system with only two allowed states, which can be called a *two level system* or a *qubit*. Qubit is a portmanteau of the words *quantum* and *bit*. The qubit is the quantum

mechanical analogue of the bit in a classical computer. Where the bit can store information as the binary digits 0 and 1, a qubit is composed of two independent quantum states which may be labeled $|0\rangle$ and $|1\rangle$. But whereas in a bit only the two states 0 and 1 are possible, a qubit can represent information in superpositions of its two basis states, $\alpha|0\rangle + \beta|1\rangle$. More importantly, multiple qubits can be entangled, producing states such as $(|0\rangle|0\rangle + |1\rangle|1\rangle)/\sqrt{2}$. In an entangled state the two individual qubits do not have a definite state of their own. Such states have no analogue in a classical computer. The number of possible entangled states that can be constructed scales exponentially with the number of qubits in a system, which is what gives quantum information processing such enormous potential. A classical computer with N bits has 2^N unique states, while a quantum computer with N qubits has 2^{2N} unique states, a difference which becomes enormous even for modest values of N. The theory of quantum computing is a thriving field unto itself; it would be well outside the scope of this thesis to go into the possibilities that quantum computing presents, but there are a number of good books and other resources available [NC04, Mer07].

Quantum computing is now a well developed field in theory but experimentally it is still in its infancy. In order to access this potential computing power there are several challenges that must be overcome. One that has already been discussed is the coherence of the qubit: we must be able to set the state of a qubit and have it maintain that state for as long as it takes to complete a calculation. Fortunately, it has been shown theoretically that if the decoherence is small enough compared to the rate at which qubit operations can be performed, it is possible to implement quantum error correction codes that will allow the quantum state to be maintained indefinitely [BDS96, KLV00]. A major, immediate goal for almost all experimentalists working in quantum information science is to demonstrate a system that can meet the threshold at which any errors can be corrected. The ability to correct errors will depend on the nature of the errors, but it is generally agreed that the threshold for fault-tolerant quantum computing is that we must be able to execute on the order of 10^4 qubit operations before an error occurs. So far this threshold has not yet been demonstrated in any physical system. A major point of experimental research is to find a

physical system appropriate for quantum information processing and demonstrate how to maintain its quantum coherence to meet this threshold.

Scalability is another important property for any potential quantum computing system. The most rapid experimental progress early on in efforts to demonstrate a quantum computer were in liquid state NMR experiments, in which a simple version of Shor's factoring algorithm [Sho97] was demonstrated [VSB01]. In spite of the success of such experiments, it is not expected that a liquid state NMR experiment can demonstrate more than about 10 qubits at a time, as there is simply no viable way to scale up this type of system. Similarly, quantum coherence in trapped ions has been studied extensively and they have shown excellent promise as qubits, but it is difficult (but perhaps not impossible) to scale them up to a system of a size large enough to do interesting quantum computations. Solid state systems, on the other hand, have an advantage because of the manufacturing technology that exists to produce large quantities of tiny electronic systems. The modern semiconductor industry can routinely pattern millions and millions of transistors and other circuit elements into a compact, reliable, relatively inexpensive chip. Although solid state systems are generally inferior to nuclear spins or atomic ion states in terms of maintaining coherence, they have the enormous potential advantage of scalability. If a quantum system in the solid state can be identified with all of the needed properties for quantum computing and a long coherence time, it will likely be a major advancement for quantum information science.

Another issue that arises when considering how to build a quantum computer is the communication of quantum information. Although it may possible to build a quantum computer using only interactions between neighboring particles, it is likely to be useful or necessary to be able to communicate quantum state information coherently across significant distances and between different types of quantum systems. One possible way to communicate quantum information over long distances is to entangle localized quantum states with photons. Photons in a high-quality waveguide can be transmitted coherently and without significant loss over long distances, where "long" distances might mean millimeters to kilometers. Entanglement can be achieved by placing a qubit in an electromagnetic resonator with a sufficiently

high quality factor to enable strong coupling between the qubit and the photons in the cavity, a field of experiments known as cavity quantum electrodynamics (CQED). Such experiments have been the domain of atomic physics for decades; recently (and motivated by quantum computation possibilities) it has expanded into solid state physics with great success.

1.3 Quantum dots

A potential well in a solid state system which confines electrons in one dimension but leaves them free to move in two dimensions is called a *quantum well*. When the electrons are confined in two dimensions and free to move in one dimension the system is known as a *quantum wire*. When a potential well is constructed that traps electrons in all three dimensions it is known as a *quantum dot*. When confined in a quantum dot, the particles' energies become fully quantized. The particles can be confined in one of several ways. The most common type of confinement is to use a combination of III-V semiconductor materials such as GaAs, AlGaAs, or InGaAs, in which the band structure can be carefully engineered to create two-dimensional quantum wells that confine in one dimension. The remaining confinement can be made by etching the well into narrow pillars, forming *vertical quantum dots* [KAT01], or by placing a set of metal gates on top of the structure and using them to spatially shape the conduction band of the quantum well so that electrons are further confined into *lateral quantum dots*. Another way quantum dots are made is by epitaxial growth of tiny particles of material, which are known as *self-assembled quantum dots* [Wan08].

The type of quantum dot we are concerned with in this dissertation are lateral quantum dots that confine electrons. Another term used for them is *electrostatically-defined* quantum dots. This type of quantum dot was pioneered in GaAs/AlGaAs quantum well heterostructures [KMM97, HKP07]. Over the past several years there has been an increasing interest and progress in developing similar quantum dots in silicon, in either Si-SiGe heterostructures or, as we study in our own lab, Si-SiO_2 metal-oxide-semiconductor (MOS) structures. Electrostatically defined quantum dots have the major advantage that they are highly tun-

able. Since the confinement (in two out of three dimensions) is provided by gate voltages, by changing these voltages we can change the depth of the potential well, the number of electrons held in the well, and the tunneling rate of electrons to and from the quantum dot. Because of this tunability, lateral quantum dots have the most promise for realizing quantum information systems in electronic quantum dots.

1.4 Quantum dots as qubits

The chief goal of experimental quantum information science at this time is to identify a system or systems which will serve well as a qubit, a quantum two-level system. Even within the context of electronic quantum dots, there are a number of possible ways this could be achieved. All that is required are two distinct quantum states that can be well controlled experimentally, yet simultaneously well isolated from unwanted interactions. We can consider using the charge state of a double quantum dot, for example, which is relatively easy to manipulate using electric fields, but is highly susceptible to decoherence from fluctuating electric fields in its environment. The spin states of the electron are immune to electric field fluctuations but they are not directly influenced by electric fields, making them harder to manipulate. Therefore there is rationale for more than one type of qubit in quantum dots. Here we discuss a few of the possibilities.

1.4.1 Charge qubit

A charge qubit is a system that can be approximated as a two-level system, where the two states correspond to two different positions of a charged particle, *e. g.* a single electron (or hole). In a quantum dot system, this is usually implemented as a double quantum dot, a system with two potential wells in close proximity to one another, with a potential barrier between them small enough that an electron may tunnel between the two dots. There may be any number of electrons in each quantum dot, but for charge qubit operation the two dots are tuned so that one electron is close to equal energy between the two dots. Then small

changes in the voltages on the gates may push the electron from one dot into the other. The two states of the qubit can be represented as the electron sitting one dot, or the other. If the two dots are tuned so that these two sites are equal in energy (the *charge degeneracy point*) the two lowest-energy eigenstates of the system are approximately the symmetric (ground state) and antisymmetric (excited state) superpositions of the electron sitting on each dot individually. At this point the electron state is minimally susceptible to electric fields, so this is the point at which the qubit is typically operated.

The charge qubit is a useful as a test case for quantum coherent behavior in quantum dots. In many ways it is simpler to create and control than other types of qubits. It is not likely to serve as a useful qubit in the long term because it has relatively strong interaction with electric fields. It experiences significant decoherence due to coupling with fluctuating electromagnetic fields from photons and phonons in the crystal environment around it, even when tuned to the charge degeneracy point.

1.4.2 Spin qubit

One system that can serve naturally as a qubit is a spin system with total spin $^1/_2$. A spin-$^1/_2$ system has two eigenstates, spin up, $|\uparrow\rangle$, and spin down, $|\downarrow\rangle$. These may naturally serve as the two basis states of the qubit. A major advancement in favor of spin qubits in laterally coupled quantum dots was a proposal given by Loss and DiVincenzo in 1998 [LD98]. They described how the spins of two electrons in could be coupled together using the exchange interaction. The spins of two electrons held apart in separate quantum dots do not interact [1], but in lateral quantum dots it is possible to change the shape of the two potential wells to bring the two electrons together so that their spatial wavefunctions overlap. At this point the Pauli exclusion principle comes into play: two electrons with aligned spins must have a spatially antisymmetric wavefunction, while if the spins are anti-aligned, the spatial wavefunction must be symmetric. When confined in a potential well, the symmetric

[1] There is a magnetic dipole-dipole interaction between any two spins, but for two electrons it is negligibly small.

wavefunction has lower energy, so the antisymmetric spin configuration is preferred. This difference in energy is an exchange interaction, which can be seen as an interaction between two spin states. By controlling the tunnel coupling between the two dots with a gate voltage, we can control the interaction between the two spins. The strength of the interaction depends *exponentially* on the gate voltage, so the interaction can potentially be turned on and off with high fidelity.

Using the exchange interaction of two electrons to control their combined spin state is an extremely valuable experimental tool, but it is not as easy to manipulate the spins individually. Single electron spins can be manipulated if there is an inhomogeneous magnetic field present so that the two dots experience a different magnetic field. They could also be manipulated by electron spin resonance (ESR). These possibilities present additional experimental challenges.

1.4.3 Singlet-triplet qubit

The spin-$^1/_2$ system is not the only possible spin system that could serve as a qubit. A spin system with higher total spin can also be used, by using a sub-manifold of two spin configurations as a qubit basis and preventing the system from being in a state outside that manifold. This can be done most readily with a two-electron system whose total spin is either 0 (singlet) or 1 (triplet). The singlet and one triplet state can be used as the two basis states of the qubit. The major advantage of the singlet-triplet qubit in lateral quantum dots is that the exchange interaction can be used to effect single-qubit operations, as was demonstrated in GaAs quantum dots by Petta, *et al.* in 2005 [PJT05] and more recently in Si quantum dots by Maune, *et al.* [MBH12]. These experiments both demonstrate the usefulness of the exchange interaction for manipulating the qubit state; both have a limitation in that they require an inhomogeneous magnetic field to exist between the two quantum dots in order to mix the singlet and triplet states.

Other combinations of electron spins in quantum dots have been proposed: a triple-

quantum dot configuration, which has three electrons contained in three quantum dots [DiV00, LTD10], and a double quantum dot system with three electrons held in two quantum dots [SSP12]. These schemes for encoding quantum information into electron spins have the significant advantage that complete control over the state of the qubit could be achieved using only the exchange interactions between neighboring quantum dots, which can be turned on and off by voltage pulses. This is easier to implement experimentally than other means of manipulating the individual spins, such as an inhomogeneous magnetic field or ESR. The gate operation times may also be faster since the exchange interaction can be tuned exponentially by the gate voltages.

1.4.4 Valley qubit

A more recent and more speculative proposal is to use the valley degree of freedom of conduction electrons in silicon as a quantum state for storing quantum information [CSK12, WC12]. As we discuss in §2.4.3, the valley degree of freedom of an electron in the silicon conduction band has (at least) two states which are far apart in momentum space, so they cannot absorb or emit light efficiently. As a result they are well protected from their surrounding environment and might have very long coherence times. The challenge is to be able to manipulate and read-out the valley state of an electron, which has not been demonstrated experimentally and will be challenging. Nevertheless, the valley degree of freedom is worth studying from a fundamental science point of view and it may be useful as a qubit at some point. Until then, it is just a complicating factor for working with spin-based qubits [CnL10].

1.5 Silicon quantum dots

The Loss and DiVincenzo proposal served to stimulate many theoretical and experimental studies on the spin states of electrons in lateral GaAs quantum dots. An excellent review of the field is given by Hanson, *et al.* [HKP07]. Coherent manipulation of the spin states of electrons in GaAs quantum dots was demonstrated by Petta, *et al.*, [PJT05] using the

exchange interaction and by ESR by Koppens, *et al.* [KBT06]. But these studies and others revealed a severe limitation in the coherence of electron spins in GaAs. Both Ga and As atoms have non-zero nuclear spins. Electrons confined in quantum dots in GaAs thus experience a fluctuating magnetic field from the nuclei, which decoheres the electron spin. In GaAs there is also a significant spin-orbit coupling that contributes to the relaxation of excited spin states. Much progress has been made in understanding the interaction between quantum dot electron spins and the nuclear spins and in reducing its decoherence effect. However, it is unlikely that this effect can be removed to a degree that makes it worthwhile for quantum computing. A better strategy is to use a material with nuclei having zero spin.

In fact all major isotopes of III-V semiconductor atoms have non-zero nuclear isotopes. On the other hand, group IV semiconductors such as C, Si, and Ge all have a primary isotope with zero nuclear spin. Electrons in these materials have many fewer nuclear spins with which to interact. It is also possible to isotopically purify these materials to remove any isotopes with a nuclear spin; in that case there is almost no nuclear spin bath at all to influence the electron spins. Furthermore, the diamond crystal structure of C, Si, and Ge assures that the spin-orbit coupling is minimal in these crystals. Thus we have been motivated to adapt quantum dot experiments from GaAs devices to group IV materials. Without a bath of nuclear spins with which to interact, the coherence time of electron spins can be extended by many orders of magnitude. For isotopically purified silicon, the coherence time of confined electrons has been measured to be as long as milliseconds [TMB06] and theoretically predicted to be as long as seconds or more under ideal conditions [WCM10].

Among the group IV materials silicon stands out, as it is the material on which the vast majority of today's semiconductor industry is based. The physical properties of silicon and the technology for making high quality electronic devices are extremely well established. This same technology enables us to make high quality devices for forming quantum dots. The type of device we have studied for the past five years in Hong Wen Jiang's lab at UCLA is based on the silicon metal-oxide-semiconductor field-effect transistor (MOSFET), the same type of device that is the basis for most computers and electronic devices in use today and for

the past several decades. Our fabrication procedures for these devices are compatible with very large scale integration (VLSI) technologies, so there is strong potential in the future for scaling these devices to incorporate many quantum dots on one chip.

Experimental progress on lateral quantum dots in silicon is several years behind the developments in GaAs quantum dots, but the exceptionally long coherence time of the spin state serves as an important motivation for making the effort to develop these devices. There are some challenges in the design, fabrication, and operation of silicon quantum dots that are unique to silicon. The progress that has been made on silicon quantum dots over the past several years, and differences between the physics of quantum dots in Si and GaAs, are reviewed in chapter 2.

1.6 Random telegraph signal analysis

Another aspect of the physics of quantum dots that we address in this dissertation is the analysis of random telegraph signals (RTS). An appropriately designed and implemented charge sensor can observe a single electron moving to and from a quantum dot, in real time. This gives us a way to directly observe the motion of a single electron in the solid state - an amazing ability considering the electron is surrounded by billions of billions of other electrons! When the quantum dot is tuned so that its chemical potential is close to the Fermi level of a reservoir of electrons, electrons can spontaneously tunnel back and forth between the quantum dot and the reservoir due to thermal fluctuations, a pattern known as a random telegraph signal (RTS). This system is a good model for the thermal behavior of two-level charge trap systems which are ubiquitous defects in solid state systems and are believed to be the origin of $1/f$ noise in semiconductors.

We have developed a novel way of analyzing RTS data based on the hidden Markov model (HMM). Hidden Markov models are statistical models for stochastic processes. They fit well with the problem of extracting information from RTS because they allow us to model the physical system independently from the experimental data it produces. Yet there is a

clear relationship between the two that allows us to make statistical inferences about the structure of the quantum dot. We have demonstrated how this type of analysis can be used to extract electron tunneling rates, detect hidden structure in the quantum dot, and measure transition rates between states that cannot be distinguished directly. The analysis of RTS is not directly related to quantum information processing applications, but it gives us a new tool for studying quantum dot physics.

1.7 Dissertation outline

This dissertation discusses experiments we have conducted to study the physics of quantum dots, particularly in silicon MOSFET devices. Chapter 2 provides additional background on the physics of silicon quantum dots and information how our silicon MOSFET quantum dot devices are fabricated. There are three major experiments that we describe on silicon MOSFET quantum dots. Chapter 3 discusses an experiment to fabricate, demonstrate, and characterize a silicon MOSFET double quantum dot. In chapter 4 we discuss an experiment in which we measured the spin lifetime of a single electron in a silicon MOSFET quantum dot, establishing a key experimental result for understanding the decoherence of confined electron spins in silicon. Chapter 5 discusses an experiment in which we designed and fabricated a device with a silicon double quantum dot and incorporated a superconducting microwave resonator for demonstrating the interaction between electrons in quantum dots and microwave photons.

In chapter 6 we discuss a different approach to studying quantum dots. We have developed a new approach to studying random telegraph signals and extracting information about the structure and dynamics of the quantum dots that participate in such processes. The analysis we describe is discussed theoretically and applied to two experiments on GaAs lateral quantum dots.

Concluding remarks and observations on the outlook for experimental progress in quantum dots in silicon are given in chapter 7.

CHAPTER 2

Quantum dots in silicon MOSFET structures

It's the little details that are vital. Little things make big things happen.

- J. R. Wooden

2.1 Lateral quantum dots

An electronic quantum dot is a potential well in which electrons can be held. These are coupled by tunnel barriers to one or more reservoirs of electrons, so that electrons can enter and leave the quantum dot by tunneling to and from the reservoir. With two reservoirs attached to the dot (a source and a drain), we can pass an electrical current through it and measure its electronic properties. In lateral quantum dots such as the ones we study, the depth of the potential well, the shape of the quantum dot, and the tunnel coupling to the reservoirs can be tuned by a series of gate electrodes to which various voltages can be applied to achieve the desired properties of the quantum dot. Tunability is a major advantage of lateral quantum dots.

When the size of the quantum dot is small enough, and the tunnel coupling to the reservoirs small enough, the number of electrons on the dot becomes quantized. The experimental signature of this is Coulomb blockade, which appears in an I-V curve as a series of relatively narrow peaks in current, separated by Coulomb repulsion between electrons on the quantum dot prevents another electron from entering the quantum dot, unless the dot's chemical potential level is tuned between the potential of the source and drain [KMM97]. When the size of the dot is small smaller yet, its energy levels become quantized. Because quantum

dots have a discrete energy spectrum like atoms do, they have been called "artificial atoms" [KAT01].

As discussed in Chapter 1, semiconductor quantum dots have been studied extensively over the past decade or so, especially for their potential use in future quantum computing applications. GaAs was the material of choice at first because high-quality quantum wells can be fabricated in GaAs heterostructures, with very low disorder. A number of excellent experiments have been done on GaAs quantum dots, which have been reviewed in multiple articles [KMM97, KAT01, RM02, WDE02, EHB05, WHM06, HKP07] and doctoral dissertations [Joh05, Han05, Vin08, Ama08, Bar10]. More recently, many research groups have been working on developing quantum dots in silicon in order to take advantage of the superior coherence of the electron spins. In our lab we have studied both GaAs and Si quantum dots, but in recent years we have spent the most effort on developing quantum dot devices based on a silicon MOSFET transistor. In lateral GaAs quantum dots, the conduction band of a quantum well is spatially shaped by gate electrodes to form quantum dots and leads in the quantum well. Our MOSFET devices are based on the same principle, but instead of a quantum well the 2D electrons in our device are confined in an inversion (or accumulation) layer in a MOSFET at a Si-SiO_2 interface.

2.2 Silicon MOSFET quantum dot device design

The silicon MOSFET quantum dot device is illustrated in Fig. 2.1. A silicon wafer, slightly p-doped, has 50 nm of dry thermally grown SiO_2 . The doping level in the wafer is small enough that the dopants freeze out at about 30 K and the bulk of the wafer is a good electrical insulator below that temperature. Above the SiO_2 layer a series of gates are patterned, which we call the depletion gates, or "side" gates. A 100 nm of Al_2O_3 covers these gates to isolate them from another metal gate, which is fabricated across the top of the entire active area of the device.

The operation of the device is illustrated schematically at the bottom of Fig. 2.1. A

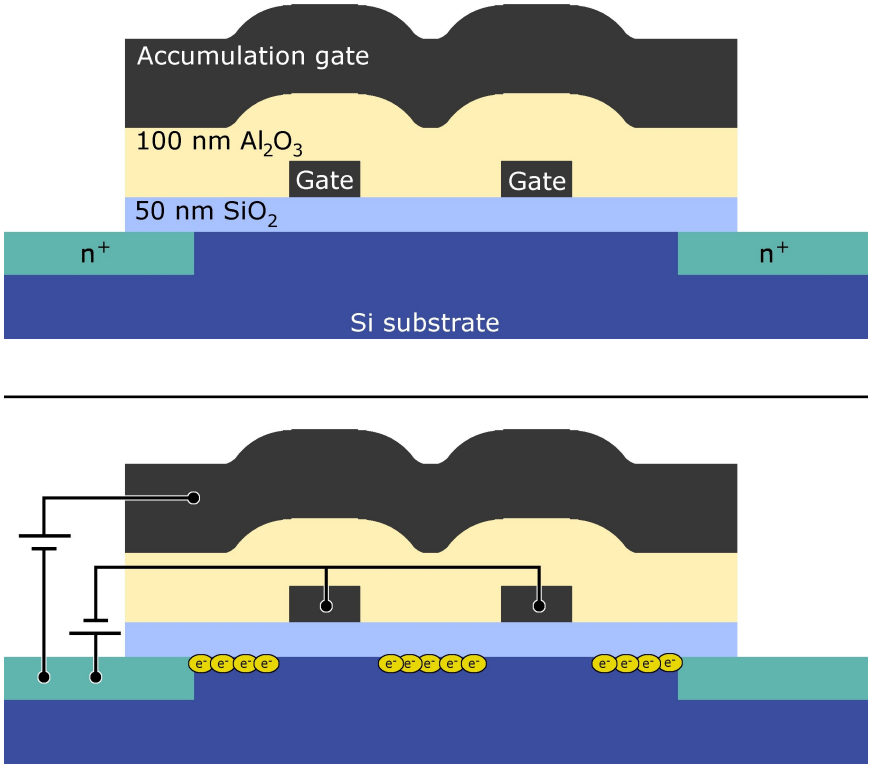

Figure 2.1: (top) Cross-section of a silicon MOSFET quantum dot device. (bottom) Schematic of the device in operation. Voltages applied to the gates shape the conduction band, trapping conduction electrons between the gates. A quantum dot is a point at which electrons become trapped in all three dimensions between the gates.

positive voltage applied to the accumulation gate raises the conduction band in at the Si-SiO_2 interface, and when the bottom of the conduction band meets the Fermi level at the ohmic contacts, an inversion layer of electrons is induced at the Si-SiO_2 interface. This is the normal operation of an n-MOS transistor. Lower voltages applied to the depletion gates deplete electrons away from these. Typically the voltages applied to the depletion gates are negative, but small positive voltages also result in depletion. The resulting shape of the conduction band in the inversion layer can include a region where a small number of electrons are trapped between gates. This island of charge is a quantum dot. The depletion gate voltages can be tuned so that electrons may tunnel between the quantum dot and outside areas of the inversion layer, where they are free in two dimensions and exist as a two-dimensional Fermi gas.

2.3 Silicon MOSFET quantum dot device fabrication

The silicon MOSFET quantum dot devices are fabricated using standard fabrication techniques that are in wide use in the semiconductor industry and in research laboratories across the world. We have deliberately chosen the silicon MOSFET structure for maximum compatibility with existing very large scale integration (VLSI) technologies that enable silicon MOSFET devices to be produced economically in large quantities. For photolithography we have relied primarily on AZ 5214-EIR photoresist. A detailed listing of the photolithography recipes we have used is given in Appendix A.

Device fabrication begins with a silicon wafer 300 μm thick. These wafers obtained commercially from Wafer World, Inc. They are boron doped, with a resistivity rating of 20-30 Ω cm, with 50 nm ($\pm$ 10%) of dry thermally grown SiO_2. Commercial silicon wafers are relatively inexpensive and the technology is well developed for producing high quality, reliable materials. Wafer production is much easier and better controlled compared to GaAs quantum wells, but the procedures needed to turn these wafers into working quantum dot devices are more involved.

The first step in the fabrication process is to etch patterned holes in the SiO_2 layer to make ohmic contact pads and alignment markers for later steps. This is done by patterning the etch windows using AZ 5214, then etching with 6 : 1 ratio NH_4F : HF (buffered oxide etchant / BOE) for 60 seconds.

Next another photolithography patterns windows for ion implantation of the ohmic contacts. The n-type ohmic contacts are made by implanting a heavy dose of phosphorus donors so that the doped area is degenerate, and will conduct even at low temperatures. The dosage is $2 \cdot 10^{15}$ cm^{-2} phosphorus atoms implanted at a kinetic energy of 40 keV[1]. After ion implantation, the photoresist is removed with acetone and the wafer is annealed in high vacuum at 950 °C for 35 minutes to repair implantation damage and activate the dopants.

To make the smallest features of the depletion gates requires electron beam lithography (EBL). Our EBL system is a Hitachi S-3000H scanning electron microscope (SEM), equipped with Nano-Pattern Generation System (NPGS - http://www.jcnabity.com/). The system's field of view is not large enough to write the entire depletion gate pattern at once, so we need to pattern the depletion gates in two steps: one using photolithography for the larger features and one using EBL for the smaller features. First the larger features (and small alignment markers for the EBL) are patterned using AZ5214 photolithography, and metal is deposited on the patterned photoresist by thermal evaporation, 5 nm of Cr and 50 nm Au. The photoresist is removed by soaking in acetone, removing the unwanted metal with it in a lift-off procedure. Then the smallest features of the depletion gates are patterned using EBL. The EBL resist we use is PMMA 950 C2, applied as described in Appendix A. Again 5 nm Cr and 50 nm Au are thermally evaporated onto the patterned resist. For removing the PMMA resist and achieving a lift-off of the metal for the smallest features, acetone will work but the best way to lift-off PMMA we found was to soak the sample in Microchem Remover PG solvent at 70 °C for several hours. Remover PG is specifically designed to dissolve and clean away PMMA.

[1]We have done this implantation step both before and after etching windows in the contact pad area, and both methods produce working contacts.

Above the depletion gate layer is the Al_2O_3 insulating layer. This layer is grown by atomic layer deposition (ALD) in A Cambridge NanoTech, Inc. Savannah-100 ALD system. The sample is placed in a chamber at a pressure of about 1 torr flowing N_2 at 20 sccm and temperature 200 °C[2]. The sample is exposed alternately to small amounts of H_2O vapor and tri-methyl aluminum (TMA), which each react with the sample surface to alternately place layers of Al and O, forming Al_2O_3, in principle one atomic layer at a time. We used pulse timings of 0.1 sec "pulse" and 10 sec "pump" time. The final thickness of the oxide usually was about 1.1 angstrom per cycle, so to achieve about 100 nm thickness we used 910 cycles. As many as 1200 cycles have been used with no noticeable difference in device performance.

To make electrical contact with the depletion gate layer we etch windows in the Al_2O_3 around contact pad areas. The normal AZ5214 photolithography is used to pattern windows over the contact pads for the depletion gates and ohmic contacts. The sample is etched in Transetch-N etchant solution, the active ingredient of which is H_3PO_4. H_3PO_4 etches Al_2O_3 but not Au or SiO_2, the two materials in the sample directly below the Al_2O_3 layer. The sample is placed in Transetch-N at 180 °C for 5 seconds, then removed and rinsed, then placed in the etchant for 5 seconds and rinsed again. Intermediate rinsing prevents the sample from heating up too much, which can over-bake the photoresist.

The final metallization step is for the ohmic contact pads and the accumulation gate. Both of these structures can be patterned in the same photolithography step, then 200 nm Al thermally evaporated onto the patterned resist and lifted off. Al on the contact pads forms a good ohmic contact with the P doped region of the wafer underneath when properly annealed.

Finally, the sample is annealed in 380 torr of 15% H_2 forming gas at 430 °C for 30 minutes. This annealing step serves two purposes. First, for the ohmic contacts it helps to break up any native oxide between the Al and Si layers, and makes Si and Al atoms interpenetrate to ensure good ohmic contact behavior. Without annealing the ohmic contacts were not

[2]Some references suggest higher growth temperatures give better quality films. We experimented with growth at 250 °C but did not see any noticeable difference in device performance.

reliable at temperatures below 4 K. Second, it improves the quality of the Al_2O_3 and SiO_2 dielectric layers. H_2 forming gas is known to reduce many types of defects in SiO_2. Annealing also seems to improve the quality of the Al_2O_3 layer, reducing its thickness and increasing its dielectric constant, as measured by ellipsometry. The 2DEG electron mobility has been measured and compared between devices that were annealed and ones that were not, and the annealing step does improve the mobility in the MOSFET channel [M. Xiao, unpublished]. However, the value of this annealing step to the oxides' quality has been the subject of much discussion in the lab, as we have not necessarily seen a correlation between annealing and the quality of the resulting quantum dots. The annealing step has a couple of negative side effects. One is that the Cr/Au metals used for the depletion gates tend to alloy during the anneal, and the gate leads become very resistive at low temperatures. This might limit our ability to send high-frequency signals to the gates. Annealing can also sometimes damage softer metal parts such as aluminum, causing device failures.

The wafers were diced by hand and dies mounted onto a 16-pin DIP chip carrier (Spectrum Semiconductor model number CSB01651). Either A4 superglue or EPOTEK H20E silver epoxy was used to secure the chip to the chip carrier. The contacts were then wired to the chip carrier by wire-bonding. We found Al wire produced more reliable wire-bonds than Au.

An alternative method for making ohmic contacts was to use the same ion-implant for n-type doping, but not to evaporate Al for metallization. Instead, after the device is mounted on a chip carrier a fine-tip soldering iron is used to apply a tiny amount of indium solder to the contact area. Indium makes good ohmic contacts with n-type silicon. The only drawback to this method is that it requires a fabricator with extremely steady hands to apply the solder precisely[3]. It is difficult to use this method when there are many contacts to solder and/or they are close together.

[3]After some practice, my own hand-soldering precision approached 200 μm . H. Pan's is better.

2.3.1 Aluminum depletion gates

As originally developed by M. Xiao, the quantum dot device fabrication procedures described above use Cr/Au as the metal for the depletion gates. For one experiment, described in Chapter 5, we incorporated a superconducting microwave resonator to our quantum dot device. The resonator design required that the depletion gates be fabricated from a superconducting material, aluminum, instead of Cr/Au. A separate experiment in our lab (not described in this dissertation), in which a microwave stripline patterned on the wafer for applying a microwave magnetic field, also required aluminum to be patterned in the same layer of the device. We discovered two challenges for using aluminum in the depletion gate layer. First, when using gold gates there was no problem fabricating the depletion gates in two steps, one using photolithography and one using EBL. But unlike gold, aluminum oxidizes when exposed to air between evaporations. The oxide layer is only a few nanometers thick, but it is enough to prevent good conduction when patching between two layers. Second, the etchant used to etch Al_2O_3 also etches aluminum, so when holes in Al_2O_3 were etched for contact pads to the depletion gate layer, the aluminum gates themselves were also etched away. To overcome these issues, we had to develop some changes to the procedures described above.

The issue of aluminum-to-aluminum patching was resolved by using an argon plasma etch in the evaporator. Our Cooke CV 301-FR5-RFX thermal evaporator includes a system for generating an argon plasma. The argon plasma etches a few nanometers of material from the sample before the second metal deposition, removing the native oxide layer that formed when it was exposed to air. The argon is then pumped from the chamber until the chamber achieves a high vacuum, so that the Al is not exposed to oxygen before the next layer of Al is evaporated. We used 50 mtorr Ar pressure and 30 W of RF power applied at 13.56 MHz to ionize the Ar. We found that this procedure reduced the height of the Al layer by 0.9 ± 0.2 nm / min. We used 8 minutes of plasma exposure to ensure the elimination of the native oxide layer. We verified on multiple devices that this procedure joined the two parts of metal deposited in separate evaporations and allowed good electrical conduction across

the joint.

The issue of etching Al_2O_3 without etching Al is more problematic. The best strategy we developed to make electrical contact with the Al depletion gate layer was to use an extra layer of Au on the Al contact pads to serve as a sacrificial protection layer. Before the Al_2O_3 was grown, an extra lift-off step was used to deposit 5 nm Cr and 100 nm Au. The Au is not etched by H_3PO_4 and serves to protect the Al during the etching process. We found that 100 nm of Au could usually protect the Al well enough from the etchant that the contact pad would work. However, often pinholes in the Au did allow etchant to get in. The etch rate of Al in H_3PO_4 is very high, so this would often result in much or all of the Al contact pad being removed. After the Al_2O_3 etch, the Au protection layer was removed by etching for 15 seconds in Transene Type TFA Gold Etchant. This procedure worked reasonably well in most cases but it was not very reliable.

Other members of the lab (M. Xiao and X. Hao), when faced with the same problem, simply used the normal H_3PO_4 etching procedure knowing that it would remove the Al at the bonding pad. They then applied either a small dab of EPOTEK H20E silver epoxy to the contact pad, or a small amount of indium solder. Either method seemed to be able to establish electrical contact between the epoxy or solder and the gate lead. The drawback of this technique is that it requires the epoxy or solder to be applied by hand, which can be inconsistent and is very difficult to do when there are many contacts to be epoxied/soldered.

2.4 Semiconductor physics relevant to quantum dots

Much of what we do discuss here is work built on results from GaAs quantum dot experiments. In this section we will focus on some of the physical properties silicon and gallium arsenide quantum dots and differences between them.

Property	Symbol	GaAs value	Si value	Units
Crystal structure		Zincblende	Diamond cubic	
Mass density	ρ	5.32	2.329	$g \cdot cm^{-3}$
Lattice constant	a	0.5653	0.5431	nm
Dielectric constant	κ	12.9	11.7	
Band gap	E_g	1.424 (direct)	1.12 (indirect)	eV
Effective mass	m^*	0.063	$m_\perp = 0.98, m_\parallel = 0.19$	m_0
Magnetic g-factor	g	-0.44	2.00	
Typical 2DEG mobility	μ	$\sim 10^6$	$\sim 10^4 - 10^5$	$cm^2\ V^{-1}\ s^{-1}$
Effective Bohr radius	a_0	10.8	3.26	nm

Table 2.1: Physical properties of Si and GaAs relevant to quantum dots.

2.4.1 Physical parameters

Gallium arsenide is a III-V semiconductor with a zincblende crystal structure, which is the same as the diamond cubic structure of silicon except that it has two types of atoms that alternate in the structure [AM76]. The difference in crystal structure leads to a different band structure, and differences in spin-orbit coupling between the two materials. The diamond structure has inversion symmetry, which means that there is no spin-orbit coupling to first order. There is no inversion symmetry in the zincblende structure, so spin-orbit coupling is significant in GaAs [Dre55]. Spin-orbit coupling explains the difference in the electronic g-factor, which in silicon is very close to the free-electron value of 2.002, but in GaAs is -0.44. In Si, the spin state which is higher in energy is aligned with the magnetic field ("spin up") and the anti-parallel spin ("spin-down") is lower in energy. In GaAs, this is reversed because the g-factor is negative; the spin-down state is higher in energy. Sometimes this causes confusion when comparing between spin effects in Si and GaAs.

The effective mass of electrons in Si is much higher than in GaAs. In Si, the effective mass is anisotropic, having the value $0.92m_0$, where m_0 is the free electron mass, in the direction

parallel to the Bloch wavevector $\boldsymbol{k}$, and $0.19m_0$ in the orthogonal directions. In a MOSFET inversion layer at low temperatures the electrons are tightly confined in the direction normal to the Si-SiO_2 interface. The conduction band valleys which have the highest effective mass normal to the interface are lowest in energy (see section 2.4.3), and in the regime where the quantum dots are operated only these valleys are occupied. The effective mass in the directions parallel to the Si-SiO_2 interface is the lower value, $0.19m_0$. This is the effective mass that determines the conduction, confinement, and tunneling behaviors of electrons in the channel. This value is still more than three times the GaAs effective mass of $0.063m_0$. Higher effective mass in silicon means that, given the same confinement potential, silicon quantum dots would have smaller electronic wavefunctions, correspondingly larger charging energies, and smaller tunnel rates. But it is not necessarily the case that the confinement is the same between different devices.

2.4.2 Nuclear spins

The primary reason we are interested in developing quantum dots in silicon is to reduce or eliminate the effects of nuclear spins on the electron spins. Table 2.4.2 shows the nuclear spins of a number of isotopes and the abundance ratio for each isotope in natural material. All of the stable isotopes of common III-V semiconductor elements Al, P, Ga, As, and In have non-zero nuclear spins, but the most commonly occurring isotopes of group IV semiconductors C, Si, and Ge all have zero nuclear spin. In Si the only naturally occurring isotope with non-zero spin is ^{29}Si, which represents only 4.3% of total atoms and has spin $^1/_2$, smaller than Ga and As isotopes. The effective nuclear Overhauser field for quantum dots in natural Si is three orders of magnitude smaller than in GaAs [APC11]. It is possible to isotopically purify these materials to eliminate those isotopes that do have a finite nuclear spin, e. g. to eliminate ^{29}Si [BSP06]. In such materials the hyperfine interaction can be almost completely eliminated, although in silicon it may actually be beneficial not to completely remove ^{29}Si if there are also defects present which have nuclear spins [WCM10].

As mentioned above, the effective mass of the electrons is higher in Si than in GaAs,

Isotope	Nuclear spin	Natural abundance (%)
^{12}C	0	98.93
^{13}C	$^{1}/_{2}$	1.07
^{27}Al	$^{5}/_{2}$	100
^{28}Si	0	92.22
^{29}Si	$^{1}/_{2}$	4.685
^{30}Si	0	3.092
^{31}P	$^{1}/_{2}$	100
^{69}Ga	$^{3}/_{2}$	60.11
^{71}Ga	$^{3}/_{2}$	39.89
^{70}Ge	0	20.38
^{72}Ge	0	27.31
^{73}Ge	$^{9}/_{2}$	7.76
^{74}Ge	0	36.72
^{76}Ge	0	7.83
^{75}As	$^{3}/_{2}$	100
^{113}In	$^{9}/_{2}$	4.29
^{115}In	$^{9}/_{2}$	95.71
^{121}Sb	$^{5}/_{2}$	57.21
^{123}Sb	$^{7}/_{2}$	42.79

Table 2.2: Naturally occurring isotopes of some relevant semiconductor elements and their nuclear spins [Hay12].

which means the confined electronic wavefunction is smaller. Being confined to a smaller area, the electron has fewer nuclei with which to interact, also reducing the effect of the nuclear spins [APC11].

2.4.3 Conduction band valley

In GaAs the conduction band minimum occurs at the Γ point, the origin, in k-space. The conduction band minimum in silicon is along the [100] direction in k-space [AFS82]. This means that in bulk silicon there are actually six nominally degenerate conduction band minima, one in each direction of the crystal axes. The shape of the conduction band minima are anisotropic, the dispersion relation parallel to the $\boldsymbol{k}$ vector being smaller than in the two orthogonal directions. Thus the effective mass of an electron in silicon is anisotropic: it is $0.92m_0$ in the direction parallel to its own k vector and $0.19m_0$ in the orthogonal directions.

The effective mass anisotropy means that when an electron is confined in one dimension along the [001] direction, the two valleys corresponding to [001] and $[00\overline{1}]$, having a higher effective mass in that direction, have a lower energy than the other four valleys. For electrons confined in a MOSFET channel at a Si-SiO_2 interface the difference is usually several 10s of meV [AFS82], which is much larger than the energy scale of our quantum dots so we may safely assume that the four higher energy valleys play no role in quantum dot physics. However, that leaves two valleys that are degenerate when an electron is confined in two dimensions. This extra degree of freedom for the electrons is a complication for silicon quantum dots that was not present in GaAs quantum dots.

The two degenerate valleys in electrons confined in [100] quantum wells can be split in turn because the electron is confined against an atomically sharp interface. If this interface causes the electron wavefunction to change significantly over a length scale $k_0^{-1} = 0.63$ nm, where k_0 is the wavenumber at the conduction band minimum, the two valleys can be mixed with the orbital degree of freedom in the dimension perpendicular to the interface, leading to an energy gap between the two valley-orbit states [AFS82]. However, in realistic systems

the confining interface is not atomically flat, and disorder in the interface tends to reduce the valley splitting [BKE04]. In 2DEG systems the electron wavefunction is distributed and it covers many such atomic steps, so 2D electrons in silicon MOSFET channels typically have small or no valley splitting. But when electrons are confined, as in quantum dots, they have fewer disorder sites with which to interact, increasing the valley splitting [GSF07].

Experimental findings show that the valley splitting is significant in silicon lateral quantum dots. Lim, *et al.*, reported a valley splitting of 100 μeV in a Si-SiGe device [LYZ11]. Borselli, *et al.*, reported valley splittings of 120 and 270 μeV in two different Si-SiGe devices. In one of our Si-SiO_2 devices we found a valley splitting of 760 μeV [XHJ10b]. Given that local disorder and confinement influence valley splitting it is not surprising that different devices, even of the same design, exhibit different valley splittings. The valley splitting may also depend significantly on the local electric field (*i.e.* it may be tunable by gate voltages), although that has not been explicitly demonstrated. Valley splittings on the order of 100 μeV are large enough that the valley degree of freedom can be well separated in energy from the spin degree of freedom. As long as the splitting is that large, the valley degree of freedom is a complicating factor for developing spin qubits, but not a critical impediment.

2.4.4 Disorder

One important difference between lateral GaAs quantum dots and silicon quantum dots is the amount of disorder in the system. GaAs quantum wells are designed and engineered to have the highest possible carrier mobility. Silicon quantum wells have never achieved the same degree of carrier mobility. In GaAs and Si-SiGe quantum wells the dopants which provide the carriers to the quantum well are deliberately placed in a separate layer so that carriers in the quantum well to increase their distance from carriers in the well. Nevertheless, they remain the primary source of scattering for carriers in the well [ND90]. In Si-SiO_2 systems the chief source of disorder is Coulomb scattering from charged impurities and surface roughness scattering at the Si-SiO_2 interface [AFS82]. Defects at the Si-SiO_2 interface are in direct contact with carriers in the inversion layer. Si-SiGe quantum wells generally have higher

mobility than Si-SiO_2 inversion layers, but are still significantly more disordered than GaAs quantum wells. Disorder causes a number of effects which are clear in experiments, but are difficult to quantify and so are not heavily reported on in the literature.

2DEG mobility is the most commonly cited measure of disorder in these systems, but it is not clear how 2DEG mobility really correlates with quantum dot device performance. We assume that higher mobility means lower disorder, but the scattering mechanisms that determine 2DEG mobility may not be the same as are important for quasi-stationary electrons in quantum dots.

One recent finding suggests that a major cause of disorder in Si nanowire quantum dots may be due to conduction band modulation due to strain [TZ12]. Strain may be caused in the silicon at the gate sites either due to fabrication processing or thermally induced strain due to thermal expansion mismatch between the gate material, the oxide, and/or the silicon. This mechanism is different from most of the assumed types of disorder in that it is not a point-like defect. Further study will be needed to elucidate this or any other source of disorder in these devices.

2.5 Conclusion

Lateral quantum dots formed in GaAs quantum wells have been an interesting quantum system to study for over a decade. The experimental progress that has been made in understanding these devices has reached the point where coherent manipulations of the electronic spin states are now routine experiments. But because of the interaction between the electron spin and the spins of the surrounding nuclei, these states do not have the coherence times we would like for storing quantum information. This has motivated us to develop similar lateral quantum dots in silicon, and in our lab specifically a silicon MOSFET structure for trapping electrons. The remainder of this dissertation will discuss the experiments we have performed on this quantum dots to better understand their physics and how their quantum states could be used for quantum information processing applications.

CHAPTER 3

Characterization of a silicon MOSFET double quantum dot

Don't let what you cannot do interfere with what you can do.

- J. R. Wooden

3.1 Introduction

A major research goal of we have persued, described in chapter 5, has been to couple a double quantum dot to a superconducting microwave resonator. In building towards this goal, we fabricated some devices which did not have a microwave resonator on them, but had the same gate geometry as the proposed devices that would contain a resonator. The specific goal of these experiments was to demonstrate that the device could indeed form a double quantum dot, and that its characteristics were suitable for coupling to the microwave resonator. In particular, we aimed to characterize the strength of the capacitive coupling between the gates and the quantum dots, which may determine whether we are able to achieve the strong coupling limit of cavity quantum electrodynamics, and to see if the inter-dot coupling could be tuned to match the 6 GHz design value for the resonant frequency of the proposed microwave resonator. In this chapter we discuss the techniques we used to characterize quantum dots and the results we obtained for one particular set of double quantum dot devices.

3.2 Device description

A microscope image of one of the devices studied in this chapter is shown in figure 3.1. It should be compared to figure 5.2, which shows a device of the same design which incorporates a microwave resonator. The devices were fabricated according to the procedures discussed in chapter 2.

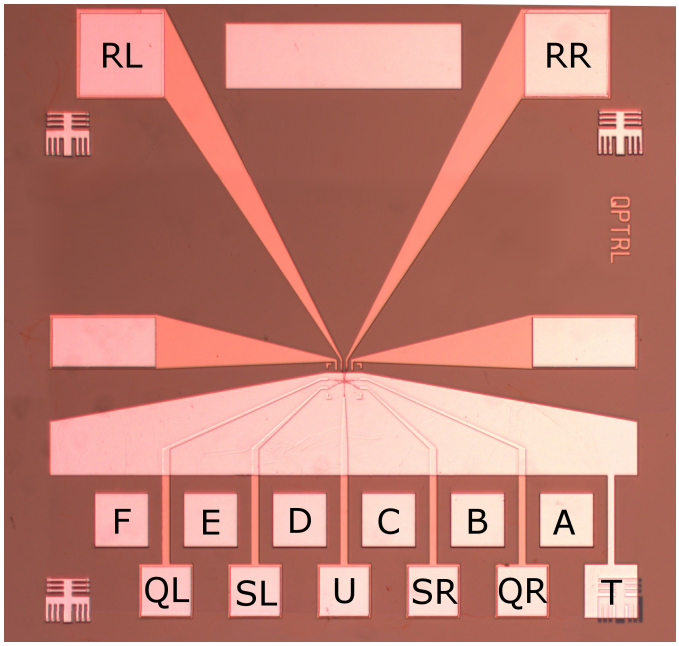

Figure 3.1: Microscope image of a device identical to the one used in the experiments, showing the ohmic contacts (labeled A-F), depletion gate leads and contact pads (refer labels to Fig. 3.2), and accumulation gate (contact pad labeled T). The device is 4 mm across in each dimension; the Si substrate is 300 μm thick. The depletion gate leads come together near the center of the device, where the quantum dot will be formed.

Figure 3.2 shows an SEM image of the depletion gates, viewed from the top down. The two quantum dots are formed between the RL, SL, and U gates (left dot) and the RR, SR, and U gates (right dot). The left dot is connected by a tunnel barrier to lead D, and the right dot to lead C. A tunnel barrier between the two dots may be formed by the voltages on the RL, RR, and U gates. Gate RL (RR) is designed to principally influence the chemical potential of

the left (right) dot. Gate SL (SR) is designed to principally tune the tunnel barrier between the left (right) dot and the outside 2DEG lead. Gate U is designed to influence the coupling between the two dots. The gap between RL and SL, and the gap between RR and SR, are intentionally very small and tuned so that electrons may not tunnel through these gaps.

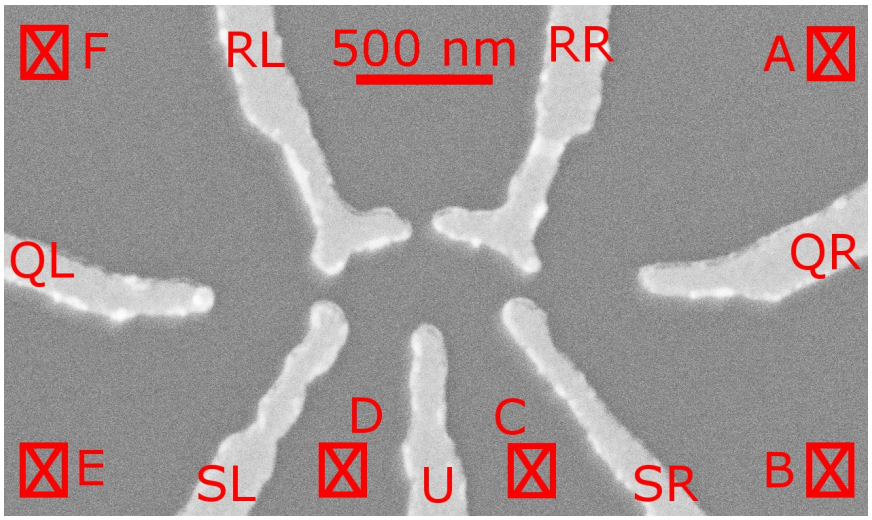

Figure 3.2: SEM image of the depletion gates of the double quantum dot device, taken before the upper layers of the device were fabricated. Letters label the names of the depletion gates and the ohmic contacts to the parts of the 2DEG layer.

The current path from C to D we call the transport channel since it carries the electrons transported directly through the quantum dot(s). The channels to each side of the quantum dot(s), one formed by contacts A and B and the other by contacts E and F, are charge sensing channels. These channels are tuned (primarily by the QR and QL gates, respectively) so that they are nearly closed, at which point the resistance of the channel becomes very sensitive to the electrostatic potential at the constriction between the RR, SR, and QR (or RL, SL, and QL) gates. Then the presence of a single electron charge at the quantum dot sites can have a measurable effect on the conductance of the charge sensing channel. By applying a voltage across the channel and measuring the resulting current, we can detect changes in the charge states of the quantum dots as changes in the measured current.

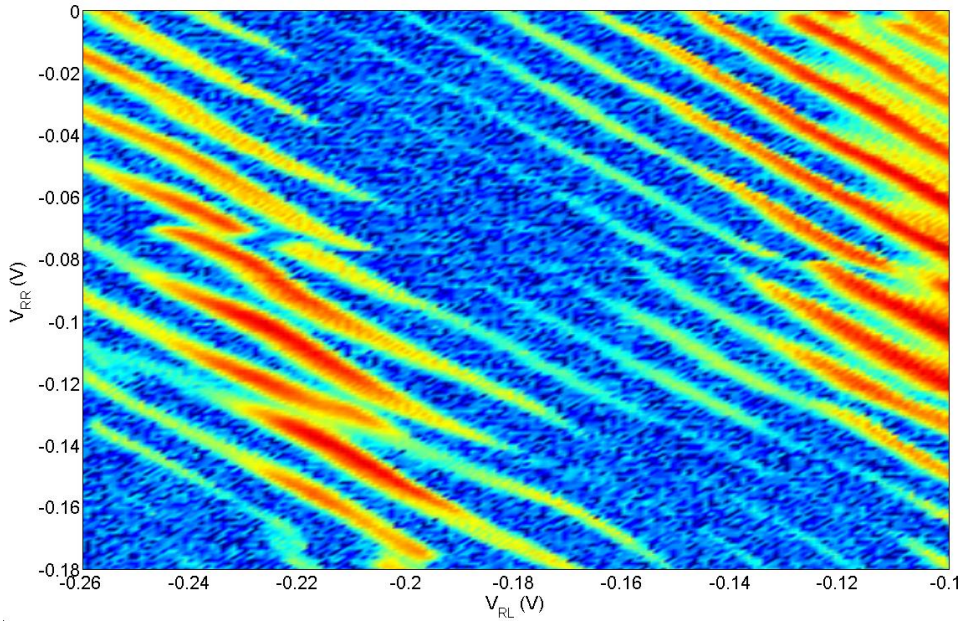

Figure 3.3: Transport current as a function of the gate voltages V_{RL} and V_{RR}. The color scale is in units of $log(Amps)$. The nearly parallel, equally spaced diagonal lines on this plot are consistent with a single, large quantum dot formed in the center of all gates. A charging event not related to the quantum dot occurs near $V_{RR} = -0.08$ V., which looks like a sudden shift in the current lines at that voltage.

3.3 Transport stability diagrams

The transport of electrons through the quantum dot system was measured by applying a sinusoidal excitation signal of amplitude 125 μV RMS and frequency 13.2 Hz to contact D and measuring the current with a lock-in current amplifier connected to contact C. A finite current may flow when the chemical potential level(s) of the quantum dot(s) are at the Fermi level of the 2DEG regions they are connected to, or between the Fermi levels of the source and drain if a finite source-drain bias is applied. Interpretation of such diagrams is discussed in several review articles [KMM97, WDE02, HKP07].

3.3.1 Two-gate Coulomb blockade diagram

The device was operated by first setting all depletion gate voltages to 0 V, then increasing the accumulation gate voltage until significant current through the transport channel could be measured, about +2.4 V. In this configuration there was good evidence that the device formed a single, large quantum dot with many electrons trapped between the depletion gates. The stability diagram in Fig. 3.3 shows many Coulomb blockade peaks, which appear as diagonal lines when plotted against two gate voltages. These lines are nearly parallel (which suggests a single quantum dot), and regularly spaced, which suggests that there are many electrons on the quantum dot. The spacing between the lines represents the charging energy of the quantum dot, which is more regular for a many-electron quantum dot because having many electrons reduces exchange effects and averages out disorder in the shape of the potential well.

3.3.2 Coulomb diamond stability diagram

Figure 3.4 shows a plot of the transport conductance as a function of the RL gate voltage and the source-drain bias voltage. The result is the characteristic Coulomb diamond pattern, which reinforces our interpretation that the device is forming a single, large quantum dot. From the size of the diamond we can extract the charging energy of the quantum dot, 0.4 meV, and the coupling constant of the RL gate to the quantum dot, $\alpha_{RL} = 0.04$ meV / V.

In this device we did not find a configuration of gate voltages that would form a double quantum dot that was observable by transport measurements. When we tuned the single large quantum dot into a double quantum dot by making the U gate more negative, the voltage change also reduced the transparency of the barriers to the leads, reducing the current through the dot. The current was reduced to being immeasurably small before double quantum dot behavior could be seen. It may have been possible to find a combination of gate voltages that did exhibit double quantum dot behavior in the transport regime, but we did not make an extended effort to find one. Instead, we relied on charge sensing to observe

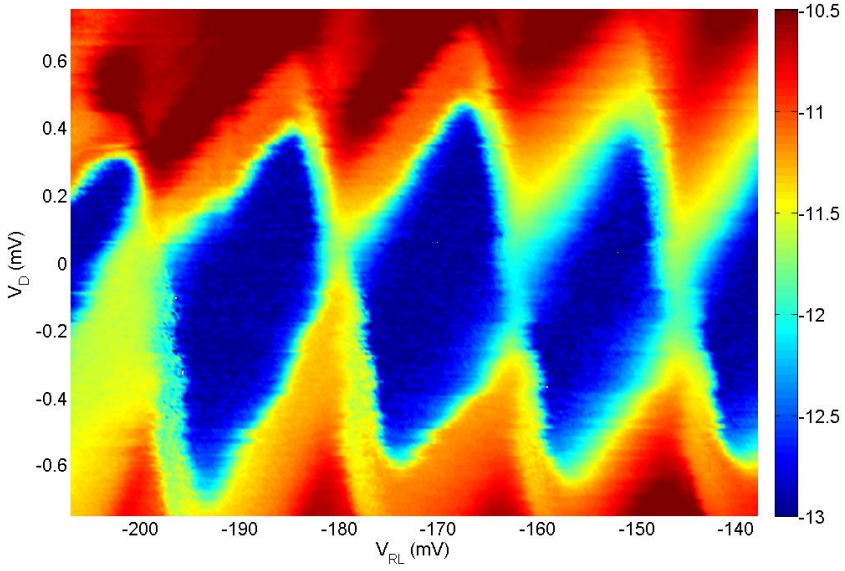

Figure 3.4: Transport stability diagram: current through the large central quantum dot as a function of the gate voltage V_{RL} and the drain-source bias voltage V_D. The color scale is in units of $log(Amps)$. In this regime of gate voltages, the system behaves like a large, single quantum dot with many electrons. The size of the diamonds reveals a charging energy of 0.4 meV, and a gate lever arm value of $\alpha_{RL} = 0.04$ meV / V.

the double quantum dot, as described in section 3.4.

3.3.3 Charge traps

The regularity of the Coulomb blockade peaks in Fig. 3.3 is broken by a sharp shift in the lines which cuts through the diagram at about $V_{RR} = -0.08$ V. This shift represents a change in the charge state of another quantum dot, impurity, or charged defect state which is near enough to the quantum dot we are studying to have a significant Coulomb interaction with it. As the gate voltages are changed they can cause a change in the charge state of such a trap, which in turn changes the electrostatic potential experienced by the quantum dot. The shift seen in this diagram is nearly horizontal in the plot, meaning that the charge trap is coupled much more strongly to the RR gate than the RL gate, which suggests that it is on the right side of the device. Such charge traps are not unusual in these devices, and we generally ascribe them to charged defect sites at the Si-SiO_2 interface. They are unfortunate because they complicate interpretation of our data, but they usually don't seriously undermine the overall usefulness of the device. Usually if such a shift occurs in a sensitive area of the stability diagram, it can often be moved to a non-sensitive region by re-tuning the depletion gate voltages, since the charge trap couples differently to each of the gates than do the quantum dot(s).

3.4 Charge sensing stability diagrams

3.4.1 Charge sensing setup

As discussed in the previous section, we found that in this device we could not form a double quantum dot with the outside tunnel barriers tuned transparent enough to observe a transport current. With our usual electronics and measurement bandwidth we were able to resolve a current as small as a few hundred femtoamps, which corresponds roughly to a minimum tunnel rate of 1 MHz. When one of the tunnel rates is smaller than this, the

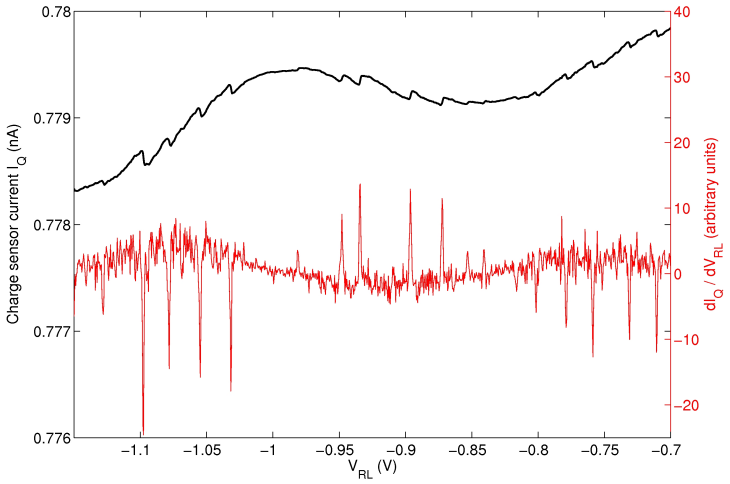

Figure 3.5: (black) Current through the charge sensor channel as a function of the gate voltage V_{RL}. The sensor channel's conductance changes as we sweep V_{RL} due to direct capacitive coupling between the gate and the sensor. Transitions of electrons on/off the quantum dot cause "kinks" in the conductance, which are small compared to this background change in the sensor's conductance caused by the changing gate voltage. (red) Derivative of the black curve, $dI/dVRL$. When plotted this way, the electron charging events are clearly seen as sharp peaks on a more slowly varying background.

transport current becomes too small to measure. With charge sensing can observe electron transitions even when the tunnel rates are orders of magnitude smaller than that.

It is worth noting that these charge sensing channels do not behave the same as similar quantum point contact (QPC) charge sensors defined in GaAs heterostructures. In a GaAs device, the electron mean free path can be long enough that electrons pass through the QPC constriction without scattering (*i.e.* ballistic transport). This allows such a constriction to have discrete subbands, and exhibit quantized conductance plateaus [WHB88, But90]. In our Si-SiO_2 devices, no such conductance plateaus are seen. The short mean free path length of electrons at the Si-SiO_2 interface means that the electrons experience significant scattering as they pass through the constriction formed by QL/QR. This causes mixing between the

subbands, and instead of conductance plateaus we observe complicated oscillations in the conductance of the channel as a function of a gate voltage. These oscillations represent a quantum interference pattern of mixing between the channel subbands. This behavior does not prevent the channels from serving as charge sensors; in fact, the sharpest oscillations in conductance have enhanced sensitivity. But at the peaks and valleys of the interference pattern, the derivative of the conductance as a function of voltage is zero, so the channel is insensitive to charging events at these points. This alternating pattern of sensitive and insensitive regions complicates experimental efforts but is not fatal.

3.4.2 Honeycomb diagrams

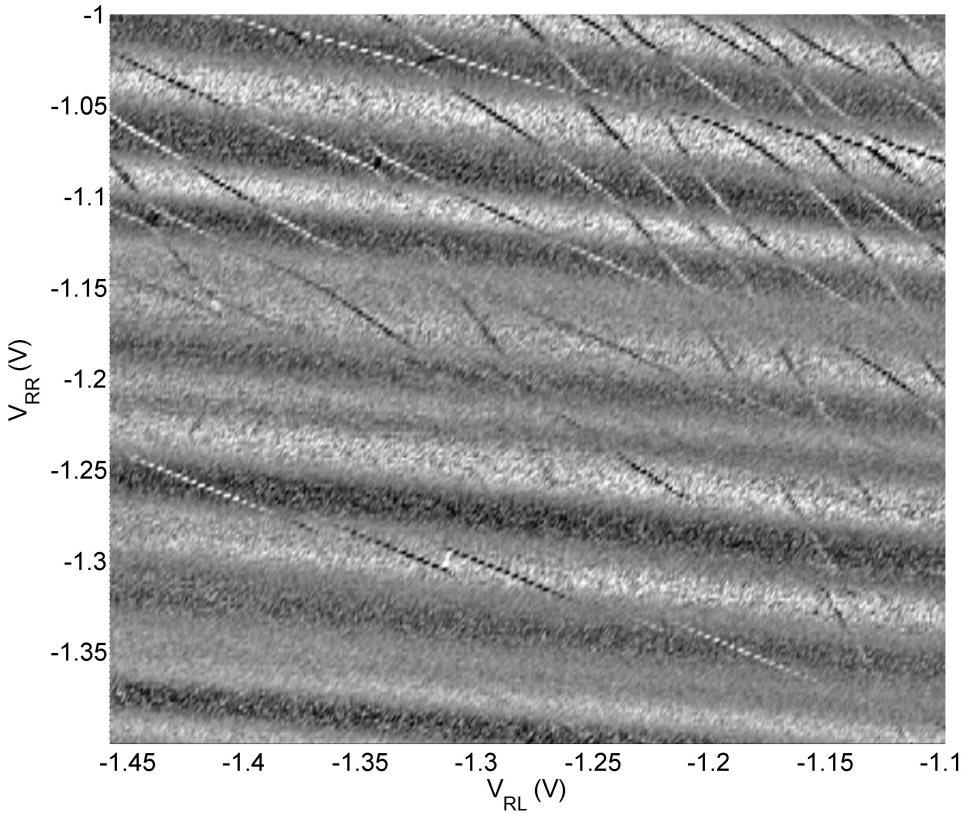

Figure 3.6: Charge sensor stability diagram of the double quantum dot: differential charge sensor current dI/dV_{RL} as a function of two gate voltages V_{RL} and V_{RR}.

Figure 3.6 shows one example of a stability diagram measured for the double quantum dot system. The differential charge sensor current, dI_{QPC}/dV_{RL}, in arbitrary units, as a function of the gate voltages V_{RL} and V_{RR}. The remaining gate voltages were fixed at $V_T = 2.5$ V, $V_{QL} = 0$ V, $V_{SL} = 0$ V, $V_U = 0$ V, $V_{SR} = 0$ V, $V_{QR} = -0.9$ V. Broad, nearly horizontal oscillations in the differential current represent fluctuations in the charge sensor channel's conductance due to its direct capacitive coupling with the gates. The narrower lines that cross the plot represent changes in the ground state charge configuration of the quantum dot. These lines are relatively close together and nearly parallel in the upper right corner of the plot, where the voltages are more positive, then towards the lower left corner of the figure the distance between the charging lines increases significantly, suggesting the few-electron regime. The last line at the bottom left is the last one visible (extra data not shown), suggesting it may be the last electron on the right dot. The more vertical lines (corresponding to transitions of the left dot) fade towards the lower left of the plot as the tunnel barrier between the left dot and lead D closes. This makes it difficult to assign electron numbers to the stability diagram with certainty, but the last distinguishable charge transition point is near $V_{RL} = -1.37$ V, $V_{RR} = -1.27$ V., which may mean there are no electrons on the dots below that point. Also evident in the diagram is the influence of disorder on the system. Many of the charge transition lines disappear and re-appear, as the tunnel barriers between the dots and the leads close and then open again. For much of the diagram the charge transition lines are not parallel, which suggests nonlinearities in the charging energy and coupling to the gates, probably also due to disorder at the SiO_2 interface.

3.4.3 Few-electron regime

Fig. 3.7 shows an example of a stability diagram where the system has been tuned into a well-behaved double quantum dot. Tentative assignment of the number of electrons on each quantum dot (N, M) is indicated at various points in the diagram, where N is the number of electrons on the left quantum dot and M is the number of electrons on the right quantum dot. The distance between the lines, combined with the gate coupling constants

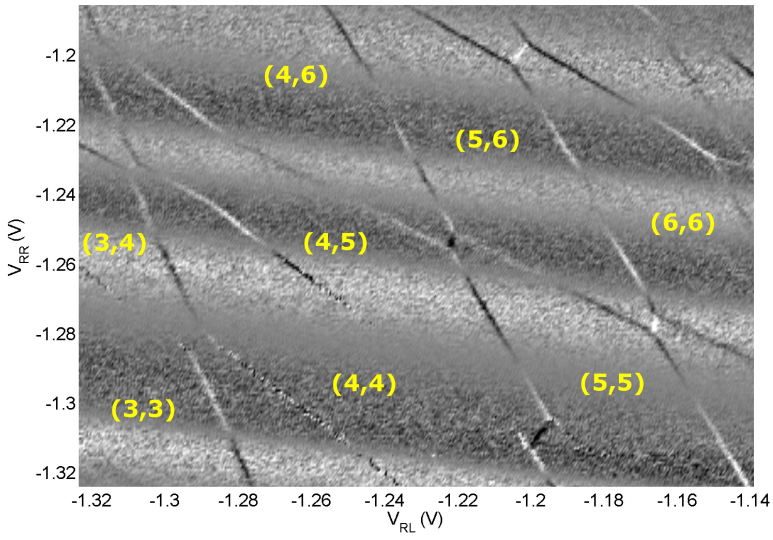

Figure 3.7: Plotted is the differential charge sensor current, dI_{QPC}/dV_{RL}, in arbitrary units, as a function of the gate voltages V_{RL} and V_{RR}. This diagram shows the "honeycomb" pattern, characteristic of a double quantum dot.

determined from the next figure, give the charging energies for this configuration: left dot, 5th electron, 2.7 meV; left dot, 6th electron 5.0 meV; right dot 5th electron 3.0 meV; right dot, 6th electron, 2.5 meV. The inter-dot Coulomb repulsion energies are measured by the length of the (positive slope) lines between areas with the same total number of electrons and vary from 0.45 meV at the (4, 6)-(5, 5) transition to 1.0 meV at the (4, 5)-(5, 4) transition. These energies were determined as described in the next section.

3.5 Interpretation of double quantum dot stability diagrams

3.5.1 Determining gate coupling strength

An important aspect of a gate-defined quantum dot device is the strength of the coupling between the gates and the energy levels of the dots. This coupling strength is usually represented by a quantity α, which represents the ratio of the change in the chemical potential of the dot, $\Delta\mu$, to a change in the gate voltage ΔV [WDE02]. α is sometimes called the

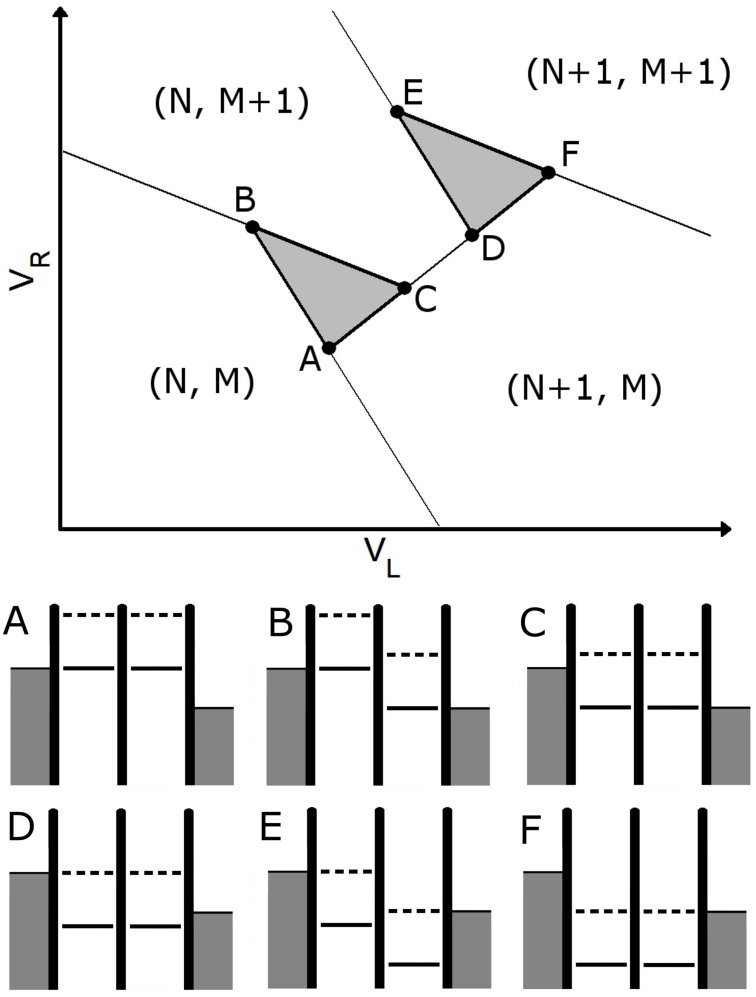

Figure 3.8: Above: a schematic picture of one small area of a double quantum dot stability diagram with a finite bias applied. Within the shaded triangles the chemical potential levels are arranged so that a finite current flows through the dots. Below: six chemical potential diagrams for the double quantum dot system representing the relative chemical potential levels of the quantum dots at each of the six corners of the triangles. A solid line indicates the chemical potential level of a dot when the opposite dot is unoccupied; a dashed line indicates the chemical potential if the opposite dot is occupied.

"coupling constant" or the "lever arm" of the gate. Knowing the lever arm allows us to determine the absolute energy scale of the quantum dots, by relating changes in gate voltages (which we control) to changes in the energy level of the quantum dot itself. In double quantum dot transport experiments, α can be determined by applying a small d.c. source-drain bias across the quantum dots, and measuring the resulting stability diagram. Finite current flows in a pattern known as the "bias triangles", in which finite current flows in a triangle-shaped region of a stability diagram. The size of these triangles reveals the coupling strength α [WDE02].

The description of coupling between the gates and the quantum dots using a single parameter α for each gate is adequate for a single quantum dot, but in a double quantum dot device each gate can influence each quantum dot with a different coupling strength. It is better to represent the coupling between gate voltages and quantum dot chemical potential levels as a tensor or matrix quantity defined by the relationship

$$\begin{pmatrix} \Delta\mu_L \\ \Delta\mu_R \end{pmatrix} = e \begin{pmatrix} \alpha_{LL} & \alpha_{LR} \\ \alpha_{RL} & \alpha_{RR} \end{pmatrix} \begin{pmatrix} \Delta V_L \\ \Delta V_R \end{pmatrix} \tag{3.1}$$

where, for example, α_{RL} is the strength of coupling between the left gate and right dot. These coupling constants can be determined from the dimensions of the bias triangles in the following way. Let the gate voltages at point A in Fig. 3.8 be denoted by $V_L^{(A)}$ and $V_R^{(A)}$, and similar notation for the other points, then define the quantities $\Delta V_{L1} = V_L^{(C)} - V_L^{(A)}$, $\Delta V_{L2} = V_L^{(B)} - V_L^{(A)}$, $\Delta V_{R1} = V_R^{(C)} - V_R^{(A)}$, and $\Delta V_{R2} = V_R^{(B)} - V_R^{(A)}$. Knowing that the chemical potentials of the dots differ by $-eV_{SD}$ at each corner of the triangle, Eq. 3.1 can be used to establish a system of equations for the α values:

$$\begin{pmatrix} \Delta V_{L1} & \Delta V_{R1} & 0 & 0 \\ 0 & 0 & \Delta V_{L1} & \Delta V_{R1} \\ \Delta V_{L2} & \Delta V_{R2} & 0 & 0 \\ 0 & 0 & \Delta V_{L2} & \Delta V_{R2} \end{pmatrix} \begin{pmatrix} \alpha_{LL} \\ \alpha_{LR} \\ \alpha_{RL} \\ \alpha_{RR} \end{pmatrix} = \begin{pmatrix} \Delta\mu_{L1} \\ \Delta\mu_{R1} \\ \Delta\mu_{L2} \\ \Delta\mu_{R2} \end{pmatrix} = \begin{pmatrix} -V_{SD} \\ -V_{SD} \\ 0 \\ -V_{SD} \end{pmatrix}. \tag{3.2}$$

The solutions of this system of equations are,

$$\alpha_{LL} = \frac{\Delta V_{R2} V_{SD}}{\Delta V_{L2}\Delta V_{R1} - \Delta V_{L1}\Delta V_{R2}} \tag{3.3}$$

$$\alpha_{LR} = \frac{-\Delta V_{L2} V_{SD}}{\Delta V_{L2}\Delta V_{R1} - \Delta V_{L1}\Delta V_{R2}} \tag{3.4}$$

$$\alpha_{RL} = \frac{(\Delta V_{R2} - \Delta V_{R1})\, V_{SD}}{\Delta V_{L2}\Delta V_{R1} - \Delta V_{L1}\Delta V_{R2}} \tag{3.5}$$

$$\alpha_{RR} = \frac{(\Delta V_{L1} - \Delta V_{L2})\, V_{SD}}{\Delta V_{L2}\Delta V_{R1} - \Delta V_{L1}\Delta V_{R2}}. \tag{3.6}$$

By making measurements of the size of the bias triangle dimensions V_{L1}, V_{L2}, V_{R1} and V_{R2} at a known bias V_{SD} we can compute the coupling constants. Once the coupling constants are known, we can determine the difference in quantum dot energy levels ($\Delta\mu_L$ and $\Delta\mu_R$) between any two points on the stability diagram, by putting the differences in gate voltages into equation 3.1.

3.5.2 Bias triangles

Fig. 3.9 shows the charge transition point of the double quantum dot between electron numbers (5, 7) and (6, 6) as seen in Fig. 3.7. Changes in the diagram when a source-drain bias voltage V_{SD} is applied to contact D while contact C is grounded are shown in Figs. 3.9 (c) and 2(d). To aid interpretation of these plots, the lines in the diagram where chemical potential levels are equal to each other or equal to their leads are drawn in (e) and (f). This highlights the bias triangles normally seen in double quantum dot transport measurements [WDE02]; within the triangles the system is out of equilibrium and a finite current flows through the dots although in this case it is too small to measure directly. In the non-equilibrium condition, the measured charge sensor current depends upon the time-averaged electron number, which is determined by the most opaque of the tunnel barriers. The data in Fig. 3.9 are consistent with the barrier between the left dot and its lead being the most opaque. In the forward bias case it takes a relatively long time for an electron to tunnel from the left lead to the left dot, but a relatively short time for that electron to tunnel to the right dot and out to the right lead. The average time it spends on the dots is nearly zero, and so there is no transition line seen on the left side of the triangles. For reverse bias, within the triangles the transiting electron moves quickly to the left dot where it spends most of its

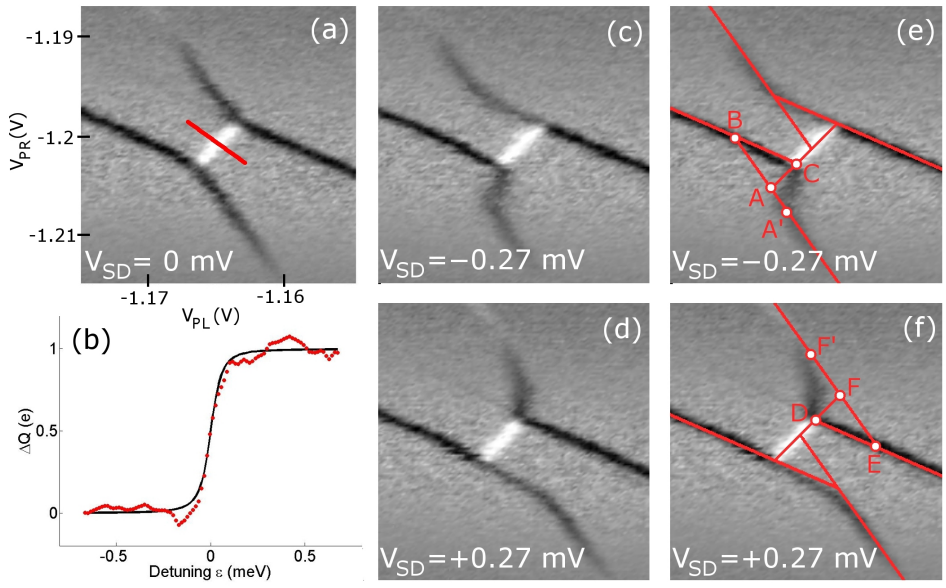

Figure 3.9: (a) Example of an inter-dot transition line. (b) The steepness of the inter-dot transition line and a fit to the data to determine the tunnel coupling between the two quantum dots, as described in the text. (c) Same stability diagram as (a), with a forward bias applied. (d) Reverse bias. (e) Same data as (c), with lines overlaid for comparison to the bias triangles interpretation. (f) Same data as (d), with lines overlaid for comparison to the bias triangles interpretation.

time before it can tunnel through the leftmost barrier. The average occupation of the dots is the same as with one extra electron on the left dot, so there is no transition line seen on the right side of the triangles.

The lines over the data in Figs. 3.9 (e) and (f) were drawn by fitting the coupling constant matrix to these data and to similar figures obtained at larger absolute bias (not shown). The coupling constants we obtain this way are $\alpha_{LL} = 0.085$, $\alpha_{LR} = 0.044$, $\alpha_{RL} = 0.044$, and $\alpha_{RR} = 0.074$. By putting these values and the differences in gate voltages into Eq. 3.1 we can find the energy difference between points C and D in Fig. 3.9, which is the inter-dot Coulomb energy at this transition, in this case found to be 0.43 meV. The charging energy of each electron in Fig. 3.7 can be found similarly: they range from 2.3 to 5.0 meV. At higher V_{PL} and V_{PR}, with more electrons occupying the dots, the charging energies were seen to be

more regular, about 0.4 meV per electron.

3.6 Inter-dot transition tuning

Fig. 3.9 (b) shows a cut of the data along the red line in Fig. 3.9 (a) to illustrate the steepness of the transition. The data have been integrated with respect to gate voltage and scaled so that the amplitude of the transition is one unit of charge. The horizontal axis is scaled to represent the detuning ϵ of the potentials of the dots relative to their degenerate point, which is related to the gate voltages by $\epsilon = \Delta\mu_R - \Delta\mu_L = (\alpha_{RL} - \alpha_{LL})\,\Delta V_{PL} + (\alpha_{RR} - \alpha_{LR})\,\Delta V_{PR}$. The shape of the transition depends on the electron temperature T_e and tunnel coupling between the two dots t, as modeled by DiCarlo, *et al.* [DLJ04]:

$$\Delta Q(\epsilon) = \frac{1}{2}\left[1 + \frac{\epsilon}{\sqrt{\epsilon^2 + 4t^2}} \tanh\left(\frac{\sqrt{\epsilon^2 + 4t^2}}{2k_B T_e}\right)\right]. \tag{3.7}$$

Fitting this model to the data using the estimated electron temperature 200 mK gives a value of $t = 58\mu$eV for the tunnel coupling between the two dots. Ignoring the off-diagonal elements of the coupling matrix would lead to an error of nearly 50% in the tunnel coupling.

3.7 Long term stability

One advantage that silicon MOSFET quantum dots appear to have over GaAs and SiGe quantum dots is the long-term charge stability of the device. Quantum dots are extremely sensitive to nearby charge reconfigurations. In the doping layer of quantum well heterostructures (such as GaAs or Si-SiGe quantum wells) there are some dopants which are ionized and some which are not. At low temperatures, the configuration of charges is generally frozen in place but if there are multiple charge configurations in the doping layer which are nearly degenerate, thermal fluctuations could cause these charges to move. It seems the charges are nearly stable but large reconfigurations can occur on the timescale of hours or days. This doesn't necessarily disrupt the quantum dot itself but it does shift the electric potential at the quantum dot, which in turn changes the gate voltages at which the quantum dot needs to

be operated. Each time such a shift occurs, the experimenter must re-tune the gate voltages in order to restore the quantum dot to its previous operation. These shifts limits an experimenter's ability to study the quantum dot system carefully because they interrupt data traces and limit the ability to reproduce data. The cause of these shifts has been attributed to charge reconfigurations in the doping layer of quantum well devices.

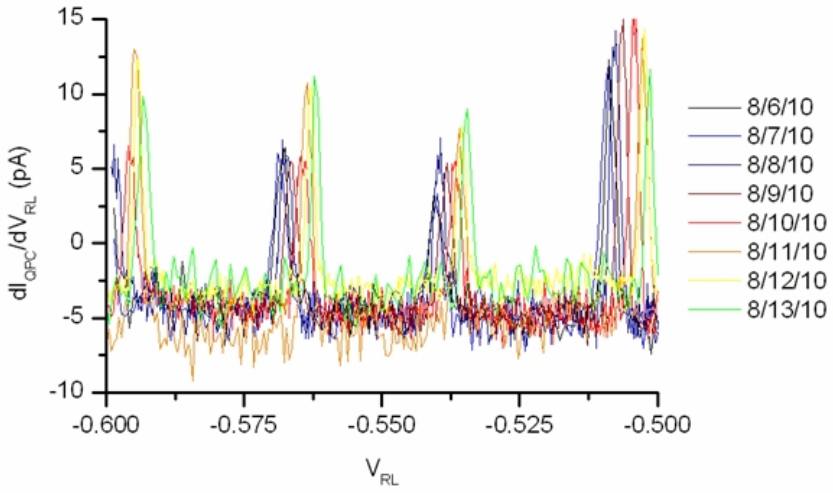

Figure 3.10: Several traces of the conductance of a quantum dot as a function of plunger gate voltage. The same scan was repeated multiple times over the course of a week to demonstrate that the same results are obtained each day.

Zimmerman, *et al.*studied charge stability in similar silicon devices and found them to be much superior to metallic single-electron transistors (SET) in terms of long-term stability [ZHF01]. They concluded that in Si, although there are charged defect states, they are more stable, and perhaps more importantly, they are non-interacting [ZHS08]. When charges do move between defect states, they tend not to be correlated with other motions, making a sudden, large shift unlikely. Our experience with Si MOSFET quantum dots corroborates their findings. We find that there is an initial period of instability when the device is first cooled down, lasting as much as 24 hours. After that, the devices are remarkably stable over periods of weeks and even months. Shown in Fig. 3.10 is an example of data we took to

confirm the stability of the double quantum dot. Each day I was working with the device I began the morning by repeating the same trace with the same voltages on each gate to confirm that the same pattern of Coulomb blockade peaks were seen. Shown in the figure are one week's worth of traces, one per day. The same pattern of Coulomb blockade peaks appears each time, with only shifts of 1-2 mV after a week. That much shift over a period of days might be explained by drifts in the voltages output by our electronic equipment.

3.8 Conclusions

In this chapter we have described a number of the techniques and measurements we have used to characterize single and double quantum dots. Transport methods we used include the two-gate transport stability diagram and the Coulomb diamond measurement for a single quantum dot. We discussed details of the charge sensing measurements used to detect the movement of charges onto and off of quantum dots. We showed how stability diagrams made from the charge sensor measurements as a function of two gate voltages reveal double quantum dot behavior in our device. The energy scale of the quantum dots can be determined by applying a source-drain bias across the two dots and observing the change in the stability diagram at the triple points. The bias triangles that appear can be interpreted to give the strength of the capacitive coupling between the gates and the quantum dots. We described a tensor representation of the coupling between the gates and the dots, and used it to determine the absolute energy scale of the double quantum dot system. The tensor representation gives a more complete and accurate picture of the quantum dots' energy scale than one-dimensional descriptions of coupling between the gates and the dots. The tunnel coupling between two dots can be extracted from analysis of the width of the inter-dot transition line in stability diagrams.

The investigations of the double quantum dot device described here were aimed at clarifying how well it will serve to couple to a microwave resonator for the purposes of making a dispersive microwave measurement of the state of the double quantum dot system and,

further down the road, for achieving strong coupling between photons in the resonator and the double quantum dot. The measurements we obtained provided a mixed answer. The strength of the coupling between the gates and the dots implies that the magnitude of the dispersive shift expected at the inter-dot transition point is on the order of 10 kHz, a shift that would be small, but probably detectable with our microwave electronics setup. This strength of coupling would be too small to achieve strong coupling unless the quality factor of the resonator were on the order of 10^6, which may be difficult but not impossible to engineer. The tunnel coupling between the two quantum dots was shown to be tunable to both above and below the 6 GHz design frequency of the resonator, suggesting that we will be able to tune the coupling to that value; however, the tunnel coupling strength was found to vary rapidly with a change in the gate voltages; the challenge may be to find a set of gate voltages at which the tunnel coupling is *exactly* in resonance with the resonator, which has a very narrow linewidth. We can estimate that the stability of the voltages on the gates will need to be sub-microvolt, which again may be difficult but not impossible. We conclude that the current design of the double quantum dot structure should be adequate for the goal of observing a dispersive shift in the microwave resonator due to the double quantum dot, but it will probably require some redesign to achieve strong coupling between the resonator and the double quantum dot.

CHAPTER 4

Measurement of the spin relaxation time of single electrons in a silicon MOS quantum dot

Talent is God-given. Be humble. Fame is man-given. Be grateful. Conceit is self-given. Be careful.

- J. R. Wooden

4.1 Background

As we discussed in Chapter 1, spurred in particular by the Loss-DiVincenzo proposal for quantum computing [LD98], there has been interest for some time in using the spin degree of freedom of electrons in semiconductor quantum dots to store and manipulate quantum information. Interest in using silicon devices in particular grew after it became clear that the coherence of electron spins in GaAs heterostructures was severely limited [HKP07]. Both gallium and arsenic nuclei have non-zero nuclear spins, which interact with the spins of electrons in the quantum dots and limit their coherence. Silicon became one of the next most interesting material possibilities, because it has a predominant isotope, ^{28}Si, which has zero nuclear spin, and therefore should not suffer as much from decoherence due to the hyperfine interaction with nuclei in the host material. Verifying this theoretical promise experimentally has been an important goal for our group and several others working on quantum information processing in silicon for the past few years. The first step in evaluating the coherence of electron spins in silicon is to measure the spin relaxation time, T_1, which is the characteristic time it takes for an electron in an excited spin state to relax to the

ground state. The elastic decoherence time T_2 is perhaps the more interesting quantity, but it is more difficult to determine experimentally. Since T_2 must be equal to or less than $2T_1$, measuring T_1 gives an upper bound for T_2 and serves as an important step in understanding the interactions of the electron spins with their surrounding environment under experimental conditions.

In this chapter we describe an experiment in which we measured the spin relaxation time of a single electron in a silicon MOSFET quantum dot. Using a pulse spectroscopy technique, we studied the excited state spectrum of the quantum dot in the few-electron regime. For a one-electron quantum dot configuration, the spin state was identifiable by its energy dependence on an applied magnetic field, which was consistent with the expected Zeeman energy. We measured the lifetime of this state at several magnetic fields by the lifetime readout technique developed by Elzermann, et al. [EHB04a]. We developed a rate equation model to describe the dynamics of the quantum dot during the pulse readout cycle. The results we obtain show that the spin relaxation time at low magnetic fields is about 30 ms, while at magnetic fields above 3 T the relaxation time drops significantly, to 1 ms at 5 T, the highest magnetic field at which we were able to measure the relaxation time. The reduction in the relaxation time at high magnetic fields is consistent with existing theory, which predicted a B^{-7} dependence of T_1. The reason for the saturation in the spin relaxation time at low magnetic fields is unknown.

The experiment described in this chapter was primarily designed and executed by Ming Xiao, and a paper describing it was published in Physical Review Letters [XHJ10a]. This author assisted with the measurements and interpretation of the data, and developed the rate equation model that describes the dynamics of the experiment.

4.2 Spin relaxation theory

The dominant mechanism for electron spins to relax from one Zeeman level to another is by interaction with the electric field of phonons of the host material, mediated by spin-

orbit coupling [HKP07, KN01, GKL04, TFJ02, TJ05]. There are two mechanisms by which phonons in a crystal generate a local electric field: piezoelectric coupling and deformation potential coupling. In GaAs quantum dots the spin relaxation rate T_1^{-1} depends on both coupling mechanisms [HKP07, EHB04a, SFH05, PJT05]. The piezoelectric coupling is due to the difference in motion between the Ga and As atoms in the crystal, which each have a different potential. But in Si there is only one type of atom so the piezoelectric contribution to coupling between is negligibly small [TFJ02]; the relaxation is expected to be dominated by the deformation potential field of acoustic phonons. The relaxation rate depends on the phonon density of states at the Zeeman energy, the amplitude of the electric fields generated by the phonons, and the strength of the spin-orbit coupling. The rate of spin relaxation T_1^{-1} due to deformation potential-coupled acoustic phonons depends on the seventh power of the magnetic field, in the limit that the wavelength of the phonon is larger than the size of the quantum dot [HKP07, TFJ02].

4.3 Device description

The device used in this experiment is a silicon MOS quantum dot structure with Cr/Au depletion gates, fabricated according to the description in chapter 2. An SEM image of the depletion gate layout is shown in Figure 4.1. The gate geometry was designed to form a single quantum dot between gates LT, RT, LB, P, and RB. Gates LB and RB serve to control the tunneling barriers between the quantum dot and its leads at the lower left and lower right of the device. For this experiment, the leads were grounded and the LB gate tuned so that the quantum dot was isolated from the left lead (electrons may not tunnel to the left lead). The voltage on gate RB was varied to control the tunneling rate between the quantum dot and the right lead. The tunneling rate for electrons between the quantum dot and the right lead could be tuned continuously from 100 Hz to 30 kHz for the last few electrons and can be measured in the time domain by an oscilloscope. Gate P, the "plunger" gate, was used to control the chemical potential of the quantum dot relative to the Fermi level of the right

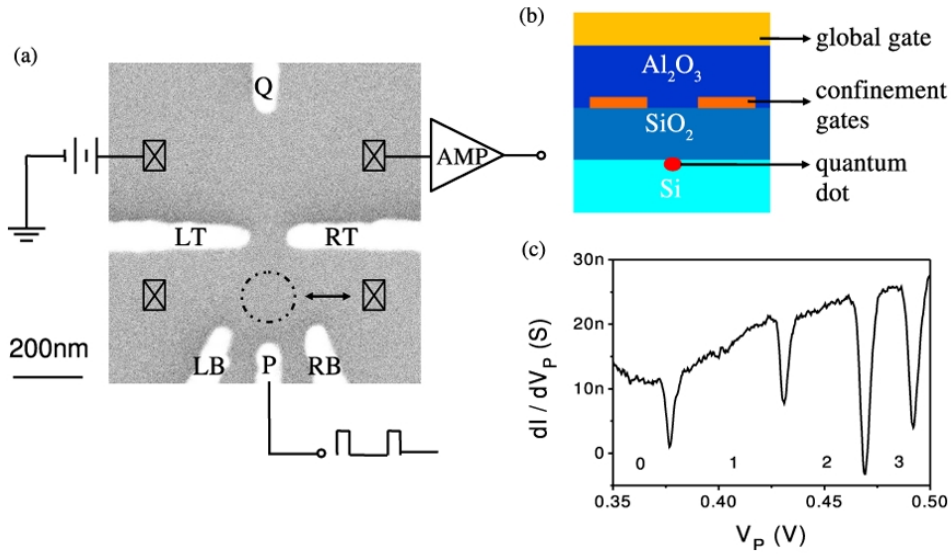

Figure 4.1: (a) SEM image of the depletion gates of the MOSFET quantum dot device. (b) Schematic cross-section of the MOSFET device structure. (c) Example charge sensor signal. The differential current through the charge sensor is plotted against the dc voltage on gate P.

lead. Gates LT and RT serve to isolate the quantum dot and its leads from a charge sensing channel located next to it; the gap between LT and RT does not allow electrons to pass. The gap exists to help improve the sensitivity of the charge sensing channel by moving the channel constriction between gates Q, LT, and RT closer to the quantum dot and reducing the screening of the quantum dot charge by the depletion gates.

The experiments were done in an Oxford top-loading ^{3}He refrigerator with a base temperature of 300 mK. The magnetic field referred to in this chapter was always applied parallel the plane of the device, in order to induce a Zeeman energy splitting between the electron spin states while minimally affecting the orbital motion of electrons in the quantum dots or the 2DEG.

4.4 Experimental methods

4.4.1 Pulse spectroscopy

Pulse spectroscopy was performed on this quantum dot in order to characterize its excited states and in particular to identify Zeeman-split states when a magnetic field was applied. A dc biasing voltage of 0.8 mV was applied across the sensing channel while the resulting current was amplified by a high-bandwidth (200 kHz) and low-noise (130 fA/$\sqrt{Hz}$) current amplifier (FEMTO DLPCA-200) at a gain of 10^8 V/A. The resistance of the sensing channel was tuned by adjusting the voltage on gate Q until it was about 10^5 ohms. The maximum bandwidth of the measurement, about 50 kHz is determined by the resistance of the charge sensor and the parasitic capacitance of the coaxial cables in our ^{3}He refrigerator, which is on the order of 100 pF. A Stanford Research System SRS535 Pulse/Delay Digital Generator was used to provide a square electrical pulse on gate P, and a synchronized SRS 830 lock-in amplifier was used to record time integrated signal at the pulse frequency.

Figure 1(c) shows a typical trace of the lock-in signal as a function of the dc voltage applied to gate P. The four dips indicate the transitions in the charge states by addition or subtraction of single electrons, as the electrochemical potential for adding one additional electron to the quantum dot is tuned to within the pulse amplitude of the Fermi level of the lead. The quantum dot was tuned such that the left barrier was completely opaque and the electron tunneling rate between the dot and the right lead was about 1 kHz. The four dips shown are most likely the last four electrons in the quantum dot, as we could not detect any additional dips as the plunger gate voltage was made more negative. We verified that the absence of the additional peak was not due to the closure of the quantum dot by increasing the voltages on RT and RB (*i. e.*, increasing the transparency of the right barrier).

Measuring the quantum dot's response to a small pulse on the plunger gate as described in the previous paragraph reveals the charging energies for electrons in the ground state of the quantum dot. By varying the pulse amplitude, we can reveal (some of) the excited state spectrum of the quantum dot [FAT03, EHB04b, Han05]. Figures 2(a) and 2(b) show in a

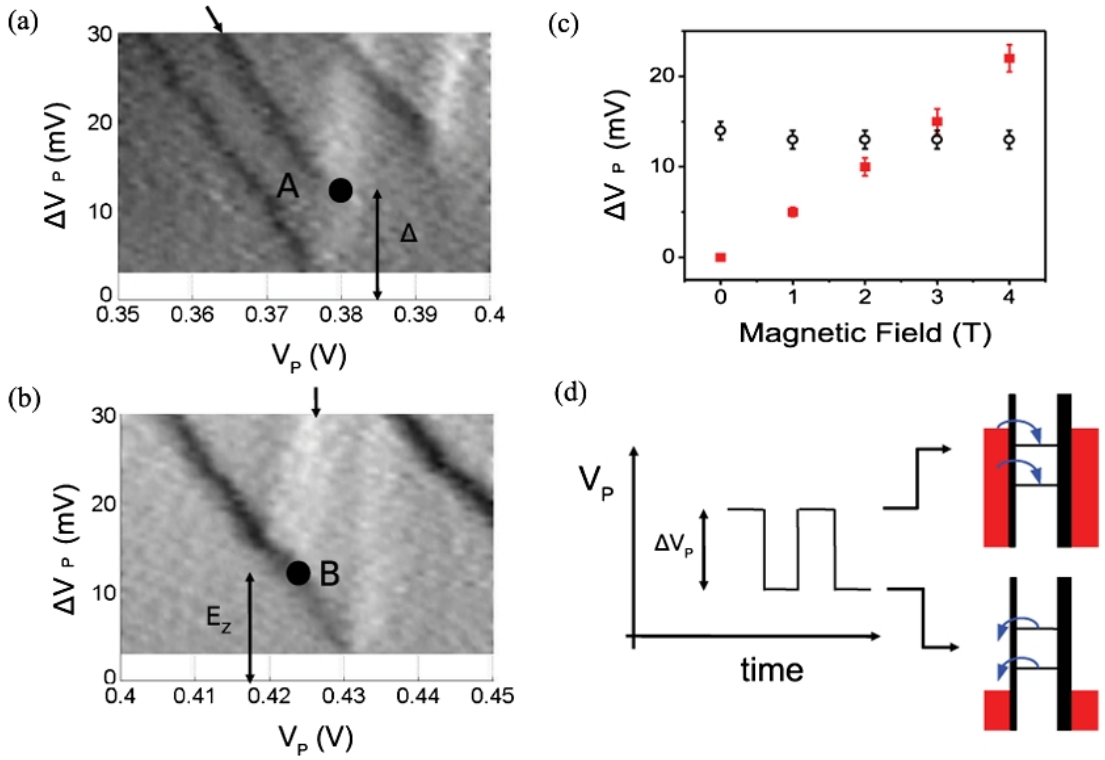

Figure 4.2: (a) Differential charge sensor current with respect to pulse amplitude and dc plunger gate voltage for the $N = 0 \leftrightarrow N = 1$ transition. (b) Same as (a), for the $N = 1 \leftrightarrow N = 2$ transition. (c) Difference in pulse amplitude, Δ, between the ground state loading line and the first excited state loading line. Red squares are for the $N = 0 \leftrightarrow N = 1$ transition; open circles are for the $N = 1 \leftrightarrow N = 2$ transition. (d) Schematic diagram showing the pulse spectroscopy experiment. During the low voltage phase of the pulse, an electron tunnels into the ground state of the quantum dot or the first excited state. During the high voltage phase the electron tunnels out of the quantum dot.

gray scale plot the derivative of the signal as a function of the pulse amplitude and dc gate voltage for the $N = 0 \rightarrow N = 1$ and $N = 1 \rightarrow N = 2$ transitions, respectively. In each case, a triangular pattern with an extra interior line (indicated by the arrow) is seen. The left line is due to the front edge of the pulse beginning the process of electron loading while the right line is for the point where the ground-state electron is unloading. An extra interior line [dark for Fig. 2(a) and bright for Fig. 2(b)] indicates an excited state. The excited state becomes visible when the excitation frequency is high enough in comparison to the relaxation rate from the excited state to the ground state. As shown in Fig. 2(d), a pulse with sufficiently high amplitude can populate either the ground state or the excited state during the high-voltage half of the pulse cycle and depopulate during the low-voltage half of the cycle. We found that the interior line terminates on the right side for the $0 \leftrightarrow 1$ electron transition and terminates on the left side for the $1 \leftrightarrow 2$ electron transition. Following arguments from excited state spectroscopy (see Fig. 5 of [HKP07]), both points A and B measure the energy difference between one of the excited states of $N = 1$ and the ground state of $N = 1$.

We studied the dependence of the termination points on a magnetic field applied parallel to the Si-SiO_2 interface and found that point A was largely independent of the magnetic field while the termination point B varied linearly with the field, as shown in Fig. 2(c). For this reason, point B is most likely a measure of the spacing of the two Zeeman sub-levels for $N = 1$ electron, and we believe point A to be either an orbital excited state, or a valley excited state of the quantum dot. Assuming the g factor of an electron in Si to be 2, the magnetic field dependence of the energy level spacing implies a conversion factor between the pulse voltage and the quantum dot potential energy (the "lever arm") of 27 meV/V. This conversion factor is consistent with that obtained from the transport measurement of Coulomb diamonds. The energy spacing of the magnetic field-independent excited state is therefore about 0.4 meV. The Coulomb charging energies needed to add an additional electron to the quantum dot for $N = 1$, $N = 2$, and $N = 3$ are 5 meV, 3.8 meV, and 3 meV, respectively.

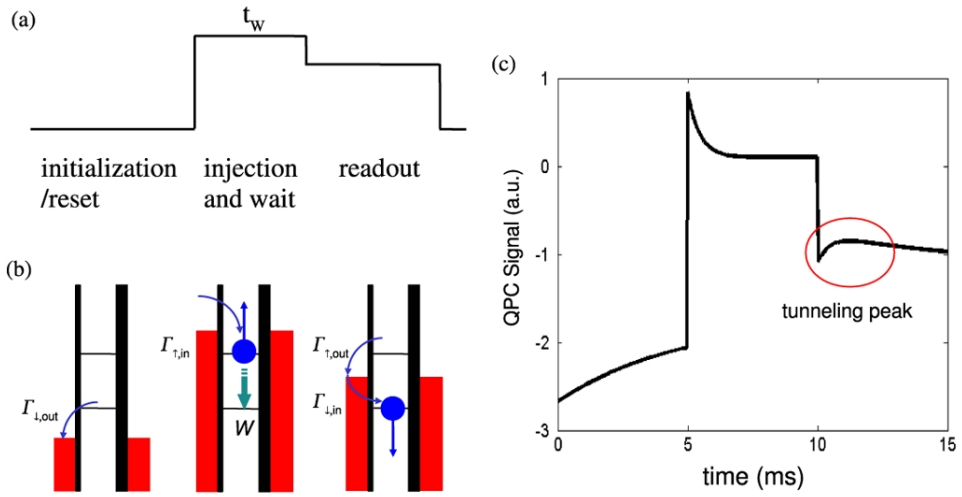

Figure 4.3: Schematic description of the relaxation time measurement pulse sequence.

4.4.2 Excited state relaxation time measurement technique

Having established the energies of the quantum dot charge states, and the magnetic field dependence of the two excited states labeled A and B in Fig. 4.2, we now perform a measurement of the relaxation time for both the excited states. Since excited state B has an energy dependence consistent with the Zeeman energy of a single electron spin in Si, we identify it as an excited spin state (spin up) of the one-electron quantum dot. The nature of excited state A is less clear, as discussed below.

The technique we used for measuring the excited state relaxation time is a three-step pulse sequence [EHB04a]. Fig. 4.3 illustrates schematically the working principle of this electrical pump-and-probe technique. The first phase of the pulse sequence, the initialization phase, positions the electrochemical potential of the quantum dot above the Fermi level of the lead so that any electron on the dot tunnels out. The length of this phase, t_1, is chosen to be long enough that the dot is reliably emptied of an electron. For the second phase, the plunger gate voltage is shifted so that both the ground state and excited states' electrochemical potentials are below the Fermi level. During this phase an electron tunnels into the quantum dot, in either the excited or ground state. This phase of the pulse sequence, the "injection and wait"

phase, lasts an amount of time t_2 (also called the waiting time t_W), which is variable. During the second phase of the pulse sequence, the electron may be in the excited state, but it can relax to the ground state, so the longer t_2 is, the smaller the probability that the electron will be in the excited state at the end of the phase. Finally, in the third phase, the read-out phase, the pulse voltage is set so that the excited state potential is above the Fermi level of the lead, while the ground state is below the Fermi level. In this arrangement, if the electron is in the ground state, it will not tunnel out; but if it is in the excited state, it will tunnel out. This tunneling can be detected by a change in the conductance of the charge sensing channel. Another electron will then tunnel back in to the quantum dot ground state, but in the interim the conductance change can be observed. In principle, this tunneling event can be detected by applying a single pulse (*i. e.*, a single-shot measurement) [EHB04a, AMR08a]. However, the relatively poor signal-to-noise ratio of our detection, about 1:5, prevented us from seeing the tunneling event in real time. We therefore applied multiple pulses and averaged the channel signal over several thousand pulse cycles. The resulting average signal was captured by a digital oscilloscope. Averaged over many cycles of the pulse, the charge sensor conductance exhibits a "tunneling peak" feature, a brief increase in the signal whose amplitude is proportional to the average population of the excited state at the end of the inject-and-wait phase. As the waiting time is increased, the amplitude of the tunneling peak decreases exponentially. The rate of decay is equal to the excited state relaxation time.

In Fig. 4.4 (a) the tunneling peak is shown for several waiting times at $B = 4$ T. The trend of the reduction of the height with increasing waiting time can be clearly seen. This dependence is plotted in Fig. 4.4 (b) and was fit to an exponential decay $\propto \exp(-t_2/T_1)$ to extract T_1. This measurement was repeated at several different magnetic field amplitudes. For magnetic fields smaller than 2 T the Zeeman energy difference was too small to resolve (due to thermal effects; smaller Zeeman energies could presumably be resolved at lower temperatures). At higher magnetic fields the relaxation rate increases and we cannot determine it reliably when it becomes comparable to the measurement bandwidth. Figure 4.4 (d) shows the relaxation rates from the excited state to ground state are plotted as a function

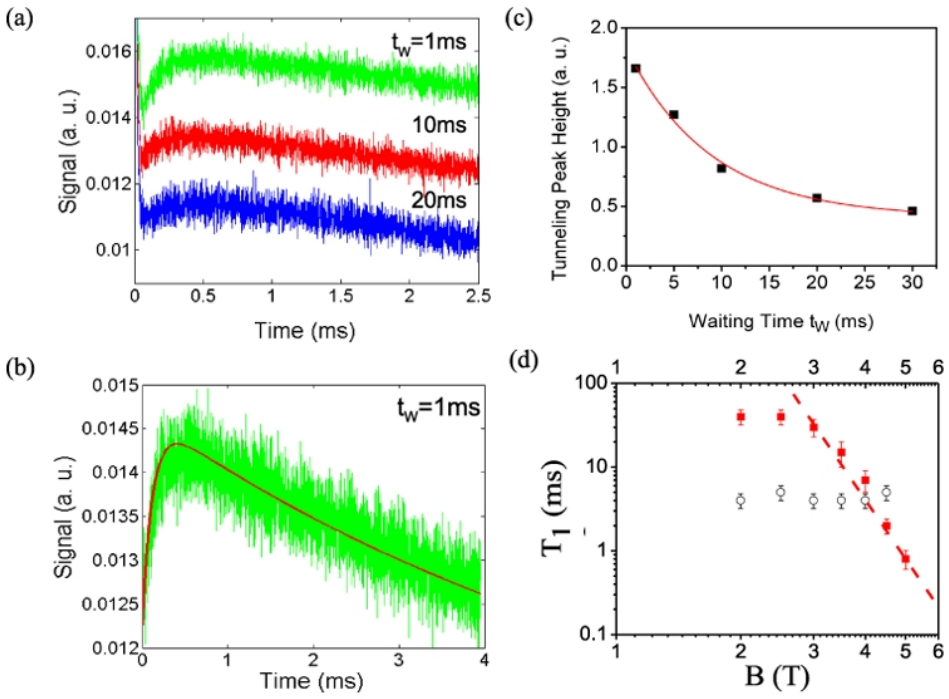

Figure 4.4: Results of the relaxation time measurements. (a) Charge sensor amplitude as a function of time during the read-out phase; three curves show the results for three different waiting times t_W, offset for clarity. (b) an example fit to the rate equation model for the case t_W =1 ms. (c) Amplitude of the 'tunneling peak' feature as a function of the waiting time. The red line is an exponential fit to the data. (d) Measured values of the relaxation time T_1 as a function of magnetic field for the $0 \leftrightarrow 1$ transition (red squares) and for the $1 \leftrightarrow 2$ transition (open circles). The red dashed line represents a fit to a B^{-7} dependence as discussed in the text.

of the magnetic field. For excited state B the relaxation rate shows a strong magnetic field dependence. In contrast, the relaxation time is essentially a constant 5 ms for excited state A.

4.4.3 Rate equation model

To support our use of the Elzerman spin read-out technique and interpret the results of the experiment we developed a rate equation model to describe the probability of an electron residing on the quantum dot as a function of time during the pulse sequence. The quantum dot is modeled as having three possible states: electron spin up, electron spin down, and no electron. The probabilities that the system is in each of the three states are contained in the vector $\boldsymbol{p} = (p_\uparrow, p_\downarrow, p_0)^T$, which evolves in time according to the equation

$$\frac{d}{dt}\boldsymbol{p} = \boldsymbol{Q}\boldsymbol{p} \tag{4.1}$$

where $\boldsymbol{Q}$ is a matrix that describes the instantaneous transition rates between the states. The transition rates depend on the dot potential, so there are three different transition matrices, one for each phase of the three-step cycle:

$$\boldsymbol{Q_1} = \begin{pmatrix} -W - \Gamma_{\uparrow,out} & 0 & 0 \\ W & -\Gamma_{\downarrow,out} & 0 \\ \Gamma_{\uparrow,out} & \Gamma_{\downarrow,out} & 0 \end{pmatrix} \tag{4.2}$$

$$\boldsymbol{Q_2} = \begin{pmatrix} -W & 0 & \Gamma_{\uparrow,in} \\ W & 0 & \Gamma_{\downarrow,in} \\ 0 & 0 & -\Gamma_{\downarrow,in} - \Gamma_{\uparrow,in} \end{pmatrix} \tag{4.3}$$

$$\boldsymbol{Q_3} = \begin{pmatrix} -W - \Gamma_{\uparrow,out} & 0 & 0 \\ W & 0 & \Gamma_{\downarrow,in} \\ \Gamma_{\uparrow,out} & 0 & -\Gamma_{\downarrow,in} \end{pmatrix} \tag{4.4}$$

where $\Gamma_{\uparrow,in(out)}$ is the tunneling rate for an electron into (out of) the $|\uparrow\rangle$ state, $\Gamma_{\downarrow,in(out)}$ is the tunneling rate into (out of) the $|\downarrow\rangle$ state, and W is the rate of relaxation from $|\uparrow\rangle$ to $|\downarrow\rangle$

. These three matrices correspond to the initialization/reset, injection and wait, and read-out phases of the cycle, respectively. Each full pulse period the probability vector evolves according to

$$\boldsymbol{p}(t_1 + t_2 + t_3) = \exp(\boldsymbol{Q_3} t_3) \exp(\boldsymbol{Q_2} t_2) \exp(\boldsymbol{Q_1} t_1) \boldsymbol{p}(0). \tag{4.5}$$

In the steady state $\boldsymbol{p}(t_1 + t_2 + t_3) = \boldsymbol{p}(0)$, so the steady state $\boldsymbol{p}(0)$ is an eigenvector of the matrix $\exp(\boldsymbol{Q_3} t_3) \exp(\boldsymbol{Q_2} t_2) \exp(\boldsymbol{Q_1} t_1)$ with eigenvalue 1. In the limit $t_1 \to \infty$, the electron always tunnels out during the empty phase, so the probabilities approach $\boldsymbol{p}(0) = (0, 0, 1)$. This is ideal since having no electron present at the beginning of the injection phase will maximize loading of the spin up state, but might not always hold since for practical reasons t_1 must be finite. The probability vector during the read-out phase $t_2 \leq t \leq t_2 + t_3$ is

$$\boldsymbol{p}(t) = \exp[\boldsymbol{Q_3}(t - t_2 - t_1)] \exp[\boldsymbol{Q_2} t_2] \exp[\boldsymbol{Q_1} t_1] \boldsymbol{p}(0). \tag{4.6}$$

The channel current averaged over many cycles of the pulse sequence $\langle I(t) \rangle$ is proportional to $p_\uparrow(t) + p_\downarrow(t)$, which during the read-out phase first increases, approximately like $\exp[-\Gamma_{\uparrow,out}(t - t_2)]$, as spin-up electrons tunnel out of the quantum dot and then decreases, approximately like $\exp[-\Gamma_{\downarrow,in}(t - t_2)]$, as spin-down electrons tunnel back in. It is this "tunneling peak" feature that signals the occupation of the spin-up state; its amplitude is reduced as we increase t_2 because spin-up electrons relax to spin-down during the injection phase. In the limit that the tunneling rates are much faster than W, the dependence on t_2 is $\exp(-W t_2)$, in which case we can determine the relaxation rate W by fitting the tunneling peak amplitude as a function of t_2 to an exponential decay curve. When W is on the same order of magnitude as the tunneling rates, as it sometimes is in our experiment, the rate equation model is useful for comparison to the observed data.

4.5 Discussion

4.5.1 $N = 1 \leftrightarrow N = 2$ transition

The pulse technique which accesses the excited state (state "B") of the quantum dot with $N = 1$ electrons by adding and removing an extra electron appears to access the spin excited state. This is evidenced by the fact that the energy level difference between the ground state and excited state is consistent with the Zeeman energy. The lifetime of this spin state appears to be nearly constant at about 30 ms for magnetic fields of 2-3 T., then drops rapidly with magnetic field until it is about 1 ms at 5 T. The trend of T_1 with respect to B at high fields is consistent with theory for spin relaxation of an electron spin for a quantum dot in silicon, which predicts a dependence of B^{-7} [Tah05]. Current theory doesn't account for the fact that our quantum dot is not formed in bulk silicon, but at a Si-SiO_2 interface which may have other effects on the spin. The presence of the interface, the gates and leads, or other environmental factors local to the quantum dot may introduce another relaxation mechanism besides longitudinal phonon emission, which may account for the saturation of T_1 at low magnetic fields. Further study is needed in order to clarify this mechanism.

4.5.2 $N = 0 \leftrightarrow N = 1$ transition

When the $N = 1$ quantum dot was access by adding an electron from the $N = 0$ configuration, a different excited state was accessed which was more difficult to interpret. This excited state's energy level did not depend on magnetic field, it was constant at about 0.4 meV. The lifetime of this state T_1 could be measured and was found also to be independent of magnetic field, about 5 ms. This lifetime is much longer than that expected for an ordinary orbital excited state of the quantum dot, which couples directly to photons and is expected to have a lifetime on the order of nanoseconds or less. On the other hand an excited state with the same spin state but a different valley configuration than the ground state may have a long lifetime. Because the two valley states are far apart in momentum space they cannot be coupled by photons, so it is possible they would have a long lifetime. A detailed theory of

valley relaxation does not exist, and there have been no other experimental measurements of the valley relaxation time with which to compare. We present the interpretation of this state as a valley excited state as our most likely interpretation of this data, but it is not clear why this state is accessed when making transitions between $N = 0$ and $N = 1$ electrons, while transitions from $N = 1$ to $N = 2$ access the spin excited state.

4.5.3 Comparison to similar experiments

The T_1 time has now been measured in other similar systems by other researchers. It was measured in a Si/SiGe lateral quantum dot by HRL Laboratories [HKB09], in a Si/SiGe lateral quantum dot at the University of Wisconsin [SPV11], and in a quantum-dot-like system based on phosphorus donors at the University of New South Wales [MPZ10]. Each of these systems is unique and the processes that lead to spin relaxation may be different, but they all have in common the trapping of single electrons in silicon, near an interface (either Si-SiO_2 or Si/SiGe). Each study used essentially the same technique for measuring the spin relaxation time as described here. The results of each of these studies are compared in Fig. 4.5. This comparison shows that there is are differences in the relaxation time between different systems of an order of magnitude or more, and in fact there is a major difference in behavior between two different devices of the same design studied by Morello, *et al.* [MPZ10]. This suggests that the specific details of electron confinement and surface interface impact the spin lifetime, especially at low magnetic fields. In all cases the spin relaxation time exceeds 1 ms, which is encouraging; in spite of the fact that local disorder and surface effects appear to have a significant influence on the electron spin, the timescale for these effects is still relatively long, and the spin relaxation time in these type of systems is not less than 1 ms and can exceed 1 s.

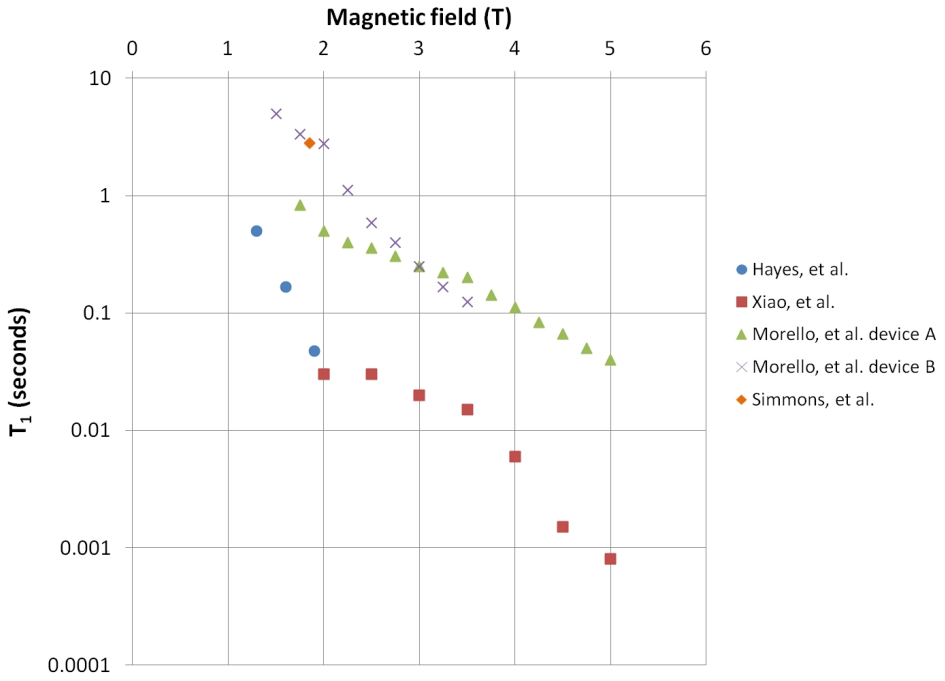

Figure 4.5: Measurements of the spin relaxation time T_1 of the spin of a single confined electron in a silicon device as a function of magnetic field, as reported by several different researchers on different systems.

4.5.4 Conclusions

The measurement of T_1 for the electron spin in a silicon quantum dot reported here marks an important step in the ability to manipulate, read-out, and understand the electron spin physics in this system. The values we find for T_1 are on the order of 1-10 ms, which is comparable to that found in GaAs and is in line with previous theoretical expectations about the electron spin lifetime. Our findings suggest that at high magnetic fields the relaxation mechanism may be the emission of a longitudinal acoustic phonon, as discussed by pre-existing theory, while at low magnetic fields a different behavior is seen that may be due to local effects that are specific to the device or the Si-SiO_2 interface. More experiments and/or theoretical development will be necessary to understand such effects. Nevertheless, a lifetime exceeding milliseconds is still a long time in terms of quantum coherence. If, as

expected, the spin dephasing time T_2 in silicon quantum dots is comparable to the T_1 found here, the electron spin in silicon quantum dots is indeed a promising candidate for studies of quantum coherence and demonstrations of quantum information processing techniques.

CHAPTER 5

Coupling a double quantum dot charge qubit to a microwave resonator

Success is never final, failure is never fatal. It's courage that counts.

- J. R. Wooden

5.1 Background

This chapter describes a series of experiments we performed in an effort to couple a high-quality superconducting microwave resonator to a double quantum dot in a silicon MOSFET device. When the coupling between microwave photons and the states of a quantum dot system is strong enough, their quantum states become entangled. This entanglement could be exploited for a number of purposes, including to use microwave photons to communicate quantum information stored in the quantum dots to other quantum systems, potentially over long distances. The long-term goal of these experiments is to demonstrate a coherent interaction between photons in the microwave resonator and the quantum dot system, and to determine its usefulness for quantum information processing experiments and applications.

In the shorter term our goal is to observe a dispersive interaction between the microwave resonator and the double quantum dot. The dispersive interaction causes a shift of the resonant frequency of the microwave resonator with a change in the state of the quantum dot. Although this is a classical effect, it is an interesting physical phenomenon worth studying unto itself, and it may be a useful mechanism for making high-fidelity, high-bandwidth measurements of quantum dots. We have focused on achieving the dispersive regime first

because it is experimentally less demanding than achieving the strong coupling regime. This chapter discusses the background, design, implementation, and results we have achieved to date in pursuit of this goal.

The experiments described here were done in collaboration with Edward Henry, Andrew Schmidt, Ofer Naaman, and Irfan Siddiqi in the Quantum Nanoelectronics Laboratory at the University of California, Berkeley.

5.2 Introduction and motivation

5.2.1 Cavity quantum electrodynamics

Cavity quantum electrodynamics (CQED) experiments are concerned with studying the interaction between matter and electromagnetic radiation at the quantum level. Such experiments were originated in the 1970s; a number of good texts and review articles exist, *e. g.* [MNB05, WVE06, WM08, CDG92, Dut05]. In CQED experiments, atoms with an electronic transition at frequency ω_a are placed inside a resonant optical cavity (*i. e.* a Fabry-Perot cavity) with a resonant frequency ω_r. The interaction between the atomic transition and the standing wave mode of the cavity produces a number of interesting physical phenomena.

A single atom, approximated as a two-level system whose energy eigenstates are described by the Pauli matrix operator σ_z, interacting with a single electromagnetic mode in the cavity has the Hamiltonian

$$H = \hbar\omega_r \left(a^\dagger a + \frac{1}{2}\right) + \frac{1}{2}\hbar\omega_a\sigma_z + \hbar g(a^\dagger\sigma^- + a\sigma^+) \tag{5.1}$$

where $a^\dagger$ and a are respectively the creation and annihilation operators for photons of frequency ω_r in the cavity and σ^-, and σ^+ are the Pauli matrix operators which operate on the state of the atom, lowering and raising its energy level, respectively.

The strength of the interaction between the electromagnetic field and the atomic transition, g, is known as the vacuum Rabi frequency. This parameter can be thought of as is the rate at which photons are created by vacuum fluctuations in the cavity, absorbed by by the

atom, then re-emitted back into the cavity. If there is no decoherence in the system, this process can repeat itself indefinitely. The emission/re-absorption frequency is $g = E_0 d/\hbar$, where d is the electric dipole moment of the atomic transition and E_0 the root-mean-square amplitude of the electric field at the atom site due to quantum vacuum fluctuations. The RMS vacuum electric field E_0 can be estimated by equating the integrated electromagnetic energy density in the cavity and equating it with that of one-half a photon:

$$\int \frac{1}{2}\epsilon_0 E^2 \mathrm{d}V = \frac{1}{2}\epsilon_0 E_0^2 V_m = \frac{1}{2}\left(\frac{1}{2}\hbar\omega_r\right) \tag{5.2}$$

which results in

$$E_0 = \sqrt{\frac{\hbar\omega_r}{2\epsilon_0 V_m}} \tag{5.3}$$

where V_m is the effective volume of the cavity. The vacuum Rabi frequency is then,

$$g = d\sqrt{\frac{\hbar\omega_r}{2\epsilon_0 V_m}}. \tag{5.4}$$

There are at least two important mechanisms for decoherence in the atom-photon coupled system that are not captured in the Jaynes-Cummings Hamiltonian Eq. (5.1) above. The Fabry-Perot cavity mirrors are not perfectly reflective, so photons are lost from the cavity through the mirrors at a rate denoted by κ. At least some of this loss is needed experimentally in order to observe photons from the cavity. Other losses can occur by the atom emitting a photon into a non-cavity mode, which occurs at a rate given by γ. Decoherence has an important influence on the nature of the interactions that are experimentally observed. In order to observe quantum coherent interactions between the atom and photons, the "strong coupling" regime, it is necessary that the rate at which photons are exchanged between the atom and the cavity, g, exceed the decoherence rates κ and γ. To achieve this it is valuable to use a transition with a large dipole moment, a cavity with a small mode volume, and a high quality factor cavity such that losses from the cavity κ are small.

CQED is a rich field as there are many different types of interaction possible between atoms and photons that can be explored with this type of experiment. For the purposes of this dissertation, we focus on two possibilities: first, the resonant, strong-coupling regime

of the interaction, in which the state of the atom becomes entangled with the photon state of the resonator. Second, the weak dispersive limit, in which the resonant frequency of the cavity can be influenced by the state of the atom.

5.2.2 Solid state CQED

Although the field of CQED originated with atomic physics, more recently it has also been making inroads into solid state physics. The insight that motivates this development is that the Jaynes-Cummings Hamiltonian Eq. (5.1) describes a general quantum two-level system interacting with an electromagnetic field mode. The two-level system need not be an atom; quantum two-level systems, qubits, in the solid state can also be used. They have the advantage that their properties can be engineered in ways that atoms cannot. With atoms the electronic transitions, dipole moments of the transitions, and other characteristics are set by nature, but with solid state systems we have a good degree of control over the properties of the system. There are also a variety of systems that can be studied in this way; *e.g.*, electronic, excitonic, and spin systems. A disadvantage of solid state systems relative to atomic systems is that the quantum system being studied is always surrounded by a crystal environment and there are many more degrees of freedom with which it can interact, generally leading to decoherence.

The first proposals to use solid state systems in a CQED experiment were introduced in 1999 [SIM99, IAB99]. Imamoglu, *et al.*, proposed using optical photons in an optical semiconductor cavity to couple the spin states of two heavy holes in a quantum dot via a Raman-like transition [IAB99]. CQED has indeed been been demonstrated using optical transitions of excitonic quantum dots embedded in semiconductor photonic cavities [KGK06, YSH04, RSL04, HBW07].

An influential step in bringing CQED experiments into the realm of solid state physics was the proposal put forward in 2004 by Blais, *et al.*, to couple the quantum state of a superconducting Josephson junction device to a microwave cavity [BHW04]. It was demon-

strated shortly thereafter by Wallraff, *et al.* [WSB04]. This type of experiment has been given the name "circuit QED" because it imitates CQED using microwave circuits instead of optical elements. Superconducting qubit devices represented a new path forward for CQED experiments because the qubit transitions are at microwave frequencies and because they can be controlled *in situ* in ways that atomic or excitonic systems cannot. In recent years the number of experiments demonstrating control over the coupled quantum states of superconducting qubits entangled with microwave photons has ballooned dramatically.

Inspired by the success of the circuit QED experiments, we are working to develop similar experiments using a superconducting microwave stripline resonator coupled to a semiconductor qubit. Silicon quantum dots have the advantage that the coherence time of the spin state is very long. Direct coupling of a photon mode to a single spin is very difficult because the magnetic coupling between a photon and an electron's magnetic dipole moment is very weak. CQED-like experiments have been performed on spin ensembles containing 10^9 spins [KOB10, AKN11], but strong coupling between a cavity mode and the magnetic dipole moment of a single spin is currently unrealistic. It may be possible to couple a spin state indirectly, by exploiting the exchange interaction. The singlet and triplet spin states of a double quantum dot can be arranged in such a way as to create an effective electric dipole moment between two spin states [BI06, TL06]. An inhomogeneous magnetic field across two quantum dots, each with one electron, mixes the singlet and triplet spin states two electrons. The admixtures of singlet and triplet that are formed have a significant electric dipole moment, which can couple the singlet-triplet qubit to the electric field of a cavity mode. Demonstrating such coupling is the ultimate goal of the experiments described here. As a step towards this goal, the present experiment is to couple a high quality factor superconducting microwave resonator to the charge state (not yet the spin state) of a double quantum dot in a silicon MOSFET structure.

5.2.3 CQED theory

5.2.3.1 Resonant strong coupling regime

In a CQED system when the qubit is in resonance with the cavity, $\omega_a = \omega_r$, it can emit a photon into the cavity, where it remains stored and continues to interact with the qubit. The qubit can emit and re-absorb the photons to and from vacuum fluctuations repeatedly, at a rate g. If this process occurs many times before the decoherence time of the cavity and qubit system, $g \gg \kappa, \gamma$, the interaction is coherent and the state of the qubit becomes entangled with the photon state of the cavity. With this interaction the state of the qubit can be coherently exchanged with the photon state of the cavity. When the qubit is on resonance with the cavity, a microwave pulse applied to the cavity can coherently manipulate the state of the qubit [DCG09]. The microwave transmission or reflection of the cavity become dependent on the state of the qubit, so that a measurement of the cavity transmission/reflection can be used as a quantum non-demolition (QND) measurement of the qubit state [BFB09]. The state of the qubit can also be transferred to a photon in the cavity, which could then in turn be transferred to the state of another qubit, allowing transmission of quantum information and two-qubit gate operations over long distances [MCG07]. Another physical phenomenon to study in this system would be lasing of the double quantum dot at microwave frequency [JMC11].

Consider a system governed by the Jaynes-Cummings Hamiltonian (Eq. 5.1), and define the detuning between the qubit transition frequency and the resonator frequency, $\Delta \equiv \omega_a - \omega_r$. Let $|n\rangle$ be the photon state of the system with n photons in the cavity, $|g\rangle$ be the ground state of the qubit, and $|e\rangle$ the excited state of the qubit. In the sub-manifold which has n excitations (the subspace of states spanned by $|n\rangle|g\rangle$ and $|n-1\rangle|e\rangle$) the Hamiltonian reduces to,

$$H = \hbar \begin{pmatrix} \omega_r n - \Delta/2 & g\sqrt{n} \\ g\sqrt{n} & \omega_r n + \Delta/2 \end{pmatrix} \tag{5.5}$$

which has eigenstates $E_\pm = \hbar\omega_r n \pm \hbar\sqrt{\Delta^2 + 4g^2 n}$ and corresponding eigenvectors

$$|+\rangle = \cos(\theta_n)\,|n\rangle\,|g\rangle - \sin(\theta_n)\,|n-1\rangle\,|e\rangle \tag{5.6}$$

$$|-\rangle = \sin(\theta_n)\,|n\rangle\,|g\rangle + \cos(\theta_n)\,|n-1\rangle\,|e\rangle\,, \tag{5.7}$$

where the mixing angle θ_n is

$$\theta_n = \frac{1}{2}\arctan\left(\frac{2g\sqrt{n}}{\Delta}\right). \tag{5.8}$$

The energy eigenstates of the system are not eigenstates of the photon number operator $aa^\dagger$, nor of the qubit state operator σ_z. Instead the eigenstates of the coupled cavity-qubit system are linear combinations of the two subsystems. When $\Delta = 0$ the energy eigenstates are $|\pm\rangle = (|n\rangle\,|g\rangle \pm |n-1\rangle\,|e\rangle)/\sqrt{2}$. The energies of the two eigenstates at $\Delta = 0$ are split by an amount $2g\sqrt{n}$. Thus the energy levels of the system are not linear in the number of excitations in the system, n, but increase as the number of photons increases. This nonlinearity enables experiments to be performed in which the number of photons in the cavity can be controlled by manipulations of the qubit [HWA08].

The splitting between the two eigenstates of the system with the same number of excitations is the vacuum Rabi splitting and it can be observed as a doubling of the resonance in the transmission spectrum of the cavity [WSB04]. When the cavity is driven with a power small enough that the average number of photons in the cavity is approximately 1, the splitting between the two transmission peaks is $2g$. Decoherence in the qubit-cavity system, either through loss of photons from the cavity or dephasing of the qubit, broadens the peaks. Therefore to observe the strong coupling regime the splitting g must be greater than the decoherence rates κ and γ.

5.2.3.2 Dispersive regime

When the qubit transition is strongly de-tuned from the resonator frequency, $\Delta \gg g$ we have the dispersive limit. The dispersive regime is experimentally less demanding to achieve because the qubit does not need to be tuned exactly into resonance with the cavity. Therefore

our first experimental effort is to observe a dispersive interaction between the double quantum dot charge qubit and the microwave cavity.

Dispersive readout of quantum dot states is closely related to the radio frequency single electron transistor (RF-SET) charge sensor [SWK98, FH00, CDC07]. It has been demonstrated using lumped-element resonators with a relatively low quality factor $Q < 100$ [PPL10]. Such dispersive readout is useful as a high-bandwidth, low-noise measurement of the quantum dot state, but with such low quality factors quantum effects are not observable. Therefore instead of a lumped element resonator we employ a superconducting microwave resonator, for which quality factors as high as 10^6 have been demonstrated. Very recently experiments have demonstrated dispersive coupling between quantum dots and a superconducting microwave resonator, none of which involve silicon quantum dots [FLB12, CWP12, DSP11].

In the dispersive limit $\Delta \gg g$, the Jaynes-Cummings Hamiltonian (Eq. 5.1) is approximately [BFB09],

$$H_{disp} = \hbar(\omega_r + \chi\sigma_z)\left(a^\dagger a + \frac{1}{2}\right) + \frac{\hbar}{2}\omega_a\sigma_z \tag{5.9}$$

where χ is the dispersive coupling strength between the resonator and the charge qubit,

$$\chi \approx -\frac{g^2 E_C}{\Delta(\Delta - E_C)} \tag{5.10}$$

and E_C is the charging energy of the qubit. In quantum dots, $E_C \gg \Delta$, so that $\chi \approx g^2/\Delta$. In this approximation the Hamiltonian commutes with the photon operators and the qubit operator, so the two systems are not entangled, but the energy levels are effectively shifted by the interaction. The photon energy is shifted from $\hbar\omega_r$ to $\hbar[\omega_r \pm g^2/(2\Delta)]$, where the $\pm$ correspond to the two different qubit states. The difference in frequency, by an amount g^2/Δ, between the two qubit states is the dispersive shift that we observe in this system. The qubit energy level is also shifted, from $\hbar\omega_a$ to $\hbar[\omega_a + 2g^2/\Delta n + g^2/\Delta]$.

5.3 Experimental details

5.3.1 Experiment design

The conceptual design of the device containing both a microwave resonator is shown in Figure 5.1. The resonator is a length of superconducting co-planar stripline (CPS) waveguide. CPS waveguides have two parallel conductors, and support balanced mode signals, *i.e.* currents along the waveguide are in equal and opposite directions. At one end the stripline is capacitively coupled to an outside circuit by a small (25 fF) coupling capacitance C_C. At the other end, the two conductors of the waveguide are joined by a relatively large (50 pF) termination capacitance C_T. At microwave frequencies the termination capacitance acts nearly as a short, while the coupling capacitance has a very high impedance, nearly an open. Thus standing wave resonances can be formed in the waveguide with a node in the electric field at the terminated end and an antinode at the coupled end. For a length of waveguide L, the lowest mode of this standing wave corresponds to a quarter wavelength, $\lambda/4 = L$. The higher order modes are not used in this experiment [1]. The red curves in Fig. 5.1 represent the oscillating electric field amplitude of the microwave resonance.

At the right side of Fig. 5.1 is shown how the double quantum dot is placed in relationship to the resonator. Small superconducting leads extending from the waveguide at the coupled end narrow down to form two of the depletion gates of the double quantum dot. The microwave electric field between the two conductors extends down to the double quantum dot. This allows the double quantum dot system to experience the maximum electric field of the microwave standing waves. The two quantum dots will be tuned so that one electron is nearly degenerate between two sites; the dipole moment of the transition is then approximately equal to one electron charge times the distance between the two quantum dots (on the order of 10 nm).

The terminating capacitor at the shorted end of the resonator is used so that each side

[1] We did observe resonances at the second ($L = 3\lambda/4$) and third ($L = 5\lambda/4$) modes of the resonator in at least one device

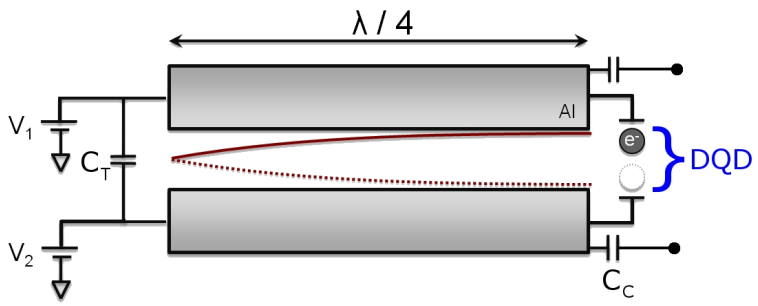

Figure 5.1: Schematic layout of the design of the device with a double quantum dot coupled to a microwave resonator.

of the resonator can be biased with a dc voltage (shown as V_1 and V_2 in Fig. 5.1). Since the resonator conductors also serve as the depletion gates of the quantum dot, the dc voltages on each conductor are needed to confine and control electrons in the double quantum dot system. If we did not need to bias each side of the resonator independently the far end of the resonator could have been literally shorted.

5.3.1.1 Superconducting microwave resonator

The material chosen for the waveguide is aluminum, which is superconducting at experimental temperatures and is relatively inexpensive and easy to fabricate relative to other superconducting metals (although see Chapter 2 for discussion of aluminum fabrication difficulties). The resonator was designed for a resonant frequency in the $\lambda/4$ mode of 6 GHz. When patterned on a (primarily) Si substrate (with its effective dielectric constant), this corresponds to a wavelength of 20 mm, so the length of stripline used is 5 mm. Each conductor is 10 μm wide and they are separated by 8 μm. These dimensions are chosen so that the characteristic impedance of the stripline is 50 Ω. The capacitive coupling to the outside circuit is designed to be about 20 fF, so that the external quality factor of the resonator is $Q \approx 1000$. The resonator is incorporated into our MOSFET structure as part of the depletion gate layer of the device and is connected directly to the plunger gates of the double

quantum dot (see Fig. 5.3).

5.3.1.2 Double quantum dot charge qubit

The qubit in our experiment is a double quantum dot charge qubit. The two qubit states correspond to one electron sitting either on the left quantum dot, $|L\rangle$, or the right quantum dot $|R\rangle$. The total number of electrons on each dot is not important, only that we work in a regime where the electron is nearly degenerate between the two dots. In that case we can approximate the Hamiltonian of the double quantum dot as,

$$H_{charge} = \frac{\epsilon}{2}\sigma_z + t\sigma_x = \begin{pmatrix} \frac{\epsilon}{2} & t \\ t & -\frac{\epsilon}{2} \end{pmatrix} \tag{5.11}$$

where ϵ is the detuning between the two dots, the difference in energy level between states $|L\rangle$ and $|R\rangle$, and t is the tunnel coupling between the two dots. The eigenvalues of this Hamiltonian are $E_\pm = \pm\sqrt{\epsilon^2 + 4t^2}/2$, and the eigenstates are

$$|x_\pm\rangle = \frac{1}{\sqrt{(\epsilon \pm \Delta E)^2 + 4t^2}} \left[(\epsilon \pm \Delta E)\,|L\rangle + 2t\,|R\rangle\right] \tag{5.12}$$

where $\Delta E = \sqrt{\epsilon^2 + 4t^2}$ is the difference in energy between the two eigenstates. Both parameters ϵ and t are experimentally tunable by adjusting the voltages on the depletion gates. When the dots are tuned so that they are equal in energy, $\epsilon = 0$, the difference in energy between the two states is $2t$ and the eigenstates are $(|L\rangle \pm |R\rangle)/\sqrt{2}$.

The advantages of the charge qubit are that it is highly tunable by changing gate voltages, and it has a relatively large dipole moment for coupling to the cavity. Its disadvantage is that it has a short coherence time, which was reported by Gorman, *et al.*, to be as long as $T_2^* \approx 200$ ns for silicon quantum dots [GHW05], although this result has been challenged [ANP06], and has not yet been confirmed by other experiments. The coherence time of a double quantum dot charge qubit in GaAs has been reported to be $T_2^* \leq 7$ ns [PPL10, FHS06, HFC03]. In GaAs the coherence of charge states is limited by the piezoelectric interaction with longitudinal acoustic phonons, a mechanism which is not present in Si, so

it is reasonable to expect that the coherence time of a double quantum dot charge qubit can be longer than ns, but in the absence of other experimental results the result by Gorman, *et al.*, remains controversial.

5.3.2 Device layout

A microscope image of the finished device is shown in Fig. 5.2. The scale of the die is 4 mm on a side. The resonator itself is two narrow conductors that meander together in the middle of the device. They are fabricated in the same layer as the depletion gates of the device, on top of the Si-SiO_2 layer and beneath a layer of Al_2O_3 . Near the top of the picture is the terminating capacitance, where these two conductors each connect to a relatively large plate. In the area above these plates, above the Al_2O_3 layer, another metal plate is patterned which covers the two, thus forming a parallel plate capacitor with both sides of the resonator (in fact the terminating capacitor is two capacitors in series). From each side of the terminating capacitor comes a lead which connects to a bonding pad in the upper left/right corners of the die for connecting to a dc voltage input for the gates. To each side of the resonator is an rf feed line, which is wire-bonded to the microwave input on the sample holder. These feed lines are capacitively coupled to the resonator by small fingers, shown in more detail in Fig. 5.3. The lower part of the device has the MOSFET quantum dot structures: the accumulation gate, six ohmic contacts for making contact to the MOSFET channel, and five more leads and bonding pads for depletion gates.

An image of the center area of the device, taken at higher magnification and before the accumulation gate was fabricated, is shown in Fig. 5.3. This shows more detail of the resonator, its coupling to the rf feed lines, and the quantum dot leads. The two resonator conductors come down from the top and have small fingers near the end which extend toward the rf feed lines. These fingers were designed to give approximately 20 fF capacitive coupling between the resonator and the feed lines on each side. These features were made with Al using optical lithography. From the bottom of the image up are five leads patterned from Cr/Au for the remaining depletion gates of the device. At the end of the resonator conductors

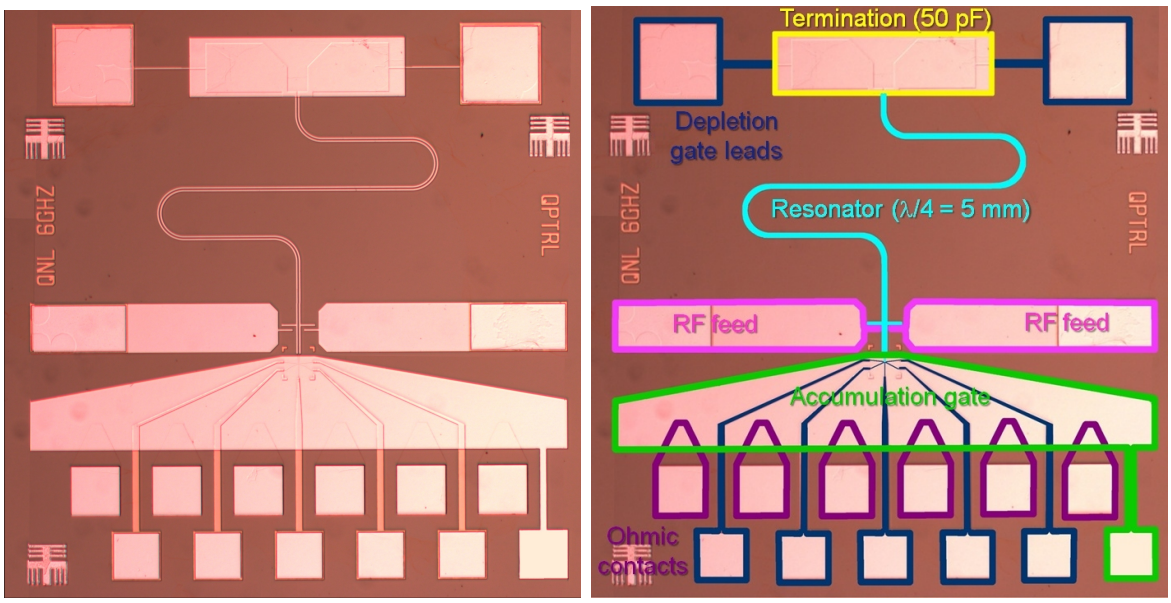

Figure 5.2: Microscope image of the device incorporating a superconducting microwave resonator and a double quantum dot. The image is 4 mm on a side. (left) Raw image. (right) Same image with various parts highlighted and labeled.

and the other depletion gate leads are small Al leads, which were patterned using electron beam lithography. Details of the device fabrication are given in Ch. 2.

5.3.3 Microwave electronics at UC Berkeley

A schematic diagram of the microwave measurement electronics used at UC Berkeley is shown in Fig. 5.4 at left. This measurement setup was designed and executed by Ofer Naaman and Ned Henry. The sample sits anchored to the mixing chamber of a dilution refrigerator with a base temperature of 30 mK. Two semirigid coaxial lines are installed in the refrigerator, one for an incoming signal (left side of the figure) and one for the outgoing signal. The input line has a series of attenuators thermally anchored at various stages of the refrigerator, designed to minimize thermal noise in the line and heat transmitted down the line to the mixing chamber. The input and output lines are joined at a circulator attached to the mixing chamber, which routes the input signal to the sample and the signal reflected

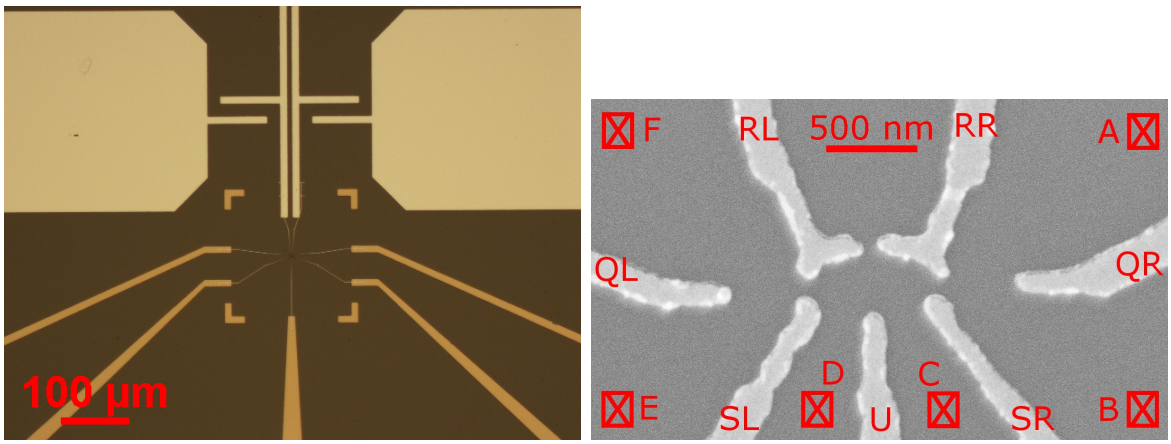

Figure 5.3: (left) Microscope image of the device, taken before the accumulation gate was fabricated. Shown are the two resonator conductors (top middle), the rf feedlines (left and right), and five other depletion gate leads (bottom) which converge on the location of the quantum dot near the center of the image. (right) SEM image of the depletion gates of the device at the point where the quantum dots are formed. Gates and ohmic contacts are labeled.

from the sample to the output line. The sample itself is mounted on a 180° hybrid coupler built into the sample holder which splits the incoming (unbalanced) microwave signal into its positive and negative phases, so that the sample is driven in balanced mode. The 90° port of the hybrid coupler is attached to ground by a 50 Ω resistor, which attenuates common mode noise. The sample holder also accommodates 16 wires for low-frequency signals, which are wire-bonded to the ohmic contacts and depletion gate contact pads on the sample.

The outgoing signal line has a circulator and 50 Ω resistor configured as an isolator mounted to the 150 mK heat exchanger stage of the refrigerator. This isolator attenuates any signals propagating down the return line towards the sample. At the 1 K stage of the refrigerator is mounted a low-noise, high-bandwidth HEMT microwave amplifier. Measurements were made using an Agilent N5230A network analyzer as both the source signal and quadrature measurement.

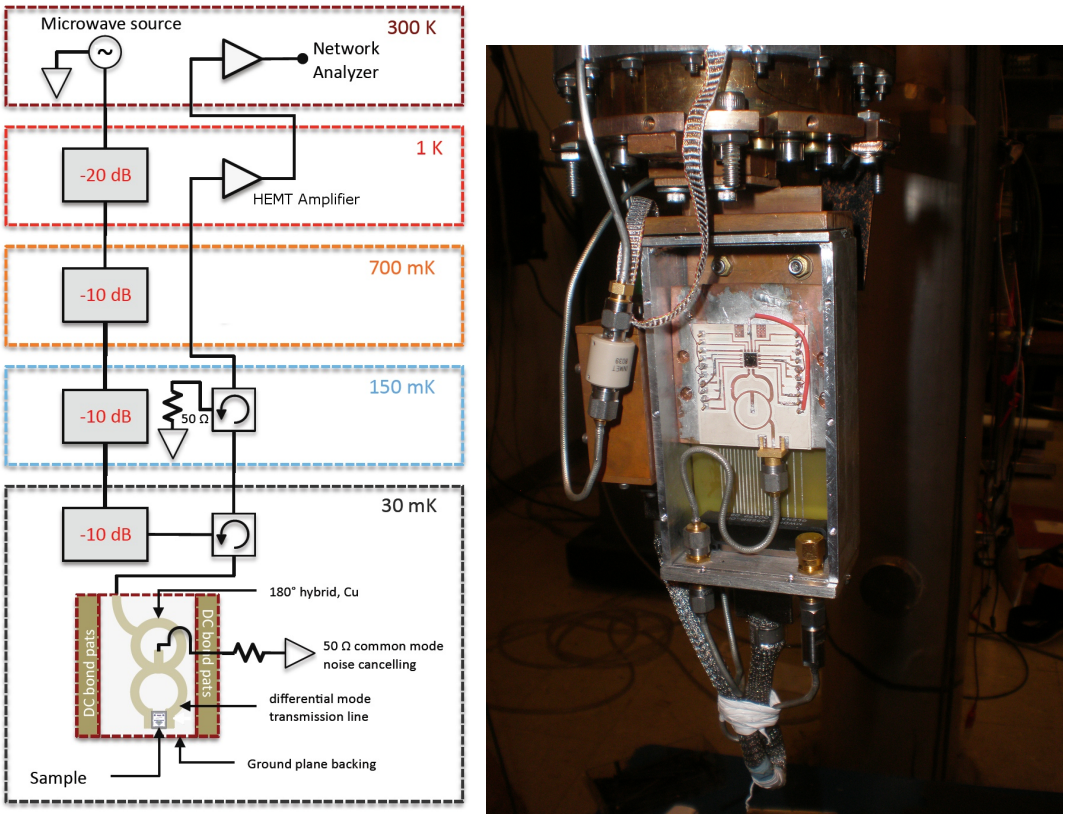

Figure 5.4: (left) Schematic of the microwave measurement electronics at UC Berkeley. (right) Image of the sample mounted in the refrigerator.

5.3.4 Microwave electronics at UCLA

An alternative, simpler microwave measurement setup was used for several measurements at UCLA. The ^{3}He refrigerator was used to make microwave measurements. This refrigerator has wiring for only one semirigid coaxial cable for microwave signals, so it was not possible to have separate lines for input and output signals. The measurement setup at UC Berkeley is less noisy and correspondingly more sensitive, and a network analyzer was available for phase-sensitive measurements. Nevertheless useful data were obtained using the simplified setup described here.

In this setup a microwave signal was introduced to the refrigerator's high frequency cable by a signal generator (HP 8673 B). A -6 dB directional coupler (PH2020-6620-05)

was attached to the top of the refrigerator to allow an input signal to be introduced to the sample while routing (part of) the reflected signal to two microwave amplifiers (Minicircuits ZVA-213-S+) connected in series, which are rated to each give 26.7 dB of gain near 6 GHz. The output of these amplifiers is fed to a microwave detector (HP8474E) which outputs a dc voltage proportional to the microwave power, which is in turn read by a Keithley 2015 multi-meter. It could also be routed to a Stanford Research SR830 lock-in amplifier for measurements in which a low frequency lock-in signal was applied to one of the MOSFET gates.

The sample itself was mounted on a custom chip carrier with a standard 16-pin DIP socket for wiring to the ohmic contacts and gates of the MOSFET. At one end of the sample holder an SMA launch connector is attached, through which the microwave signal is introduced (and the reflection signal extracted). On this chip carrier the center pin of the SMA connector is wire-bonded to one of the rf feed lines on the sample and the other rf feed line is wire-bonded to the ground side of the SMA connector.

5.4 Resonator circuit models

5.4.1 RLC model

A useful model for the microwave resonator in this experiment is that of a parallel RLC resonant circuit. We will show in §5.4.2 how this model can be derived from a more sophisticated one that describes the resonator as a quarter-wave truncated waveguide. Here we review the theory of the parallel RLC circuit, which can be found in many textbooks (*e. g.* [Poz04], p. 269).

The RLC model is that of one resistor R_r, one capacitor C_r, and one inductor L_r connected in parallel. We can describe the motion of charge in the circuit by letting the charge on the capacitor q be the "coordinate" of the system, which can be introduced in the differential

equation

$$\frac{d^2q}{dt^2} + \frac{1}{R_rC_r}\frac{dq}{dt} + L_rC_rq = V_{IN}(t) \tag{5.13}$$

which is exactly analogous to the driven, damped harmonic oscillator model. When $V_{IN} = 0$ it has the solution

$$q(t) = q(0)\exp\left[i\omega_r t - \kappa/2t + \phi_0\right] \tag{5.14}$$

where

$$\omega_r = 1/\sqrt{L_rC_r} \tag{5.15}$$

is the resonance frequency of the circuit, $\kappa = 2/(R_rC_r)$ is the decay rate due to loss in the resistor, and ϕ_0 is an arbitrary phase.

The input impedance of the RLC circuit as a function of frequency is

$$Z_{RLC}(\omega) = \left[\frac{1}{R_r} + i\omega C_r + \frac{1}{i\omega L_r}\right]^{-1}. \tag{5.16}$$

The input impedance is very large except near the resonant frequency ω_0. It is useful to expand this formula in terms of the detuning from the resonant frequency, $\delta\omega \equiv \omega - \omega_0$. To first order in $\delta\omega$,

$$Z_{RLC}(\delta\omega) \approx \frac{R_r}{1 + 2iQ\left(\frac{\delta\omega}{\omega_0}\right)} \tag{5.17}$$

where we have introduced the quality factor

$$Q = 2\omega_0/\kappa = R_rC_r\omega_0. \tag{5.18}$$

The resonance can be characterized by the two parameters center frequency ω_0 and quality factor Q. It is useful for any resonant circuit to describe the resonator using these two parameters, even when the resonance is not a lumped RLC circuit.

5.4.2 Transmission line model - quarter wave resonator

The resonator is constructed from a co-planar stripline (CPS) waveguide, which behaves as a high-quality transmission line with a capacitance per unit length C_l, impedance per unit length L_l, and series resistance per unit length R_l. The characteristic impedance of

such a line is $Z_0 = \sqrt{L_l/C_l}$, the phase velocity is $v_p = 1/\sqrt{L_l C_l}$, and propagation constant $\gamma = \alpha + i\beta$, where $\beta = \omega/v_p = \sqrt{L_l C_l}\omega$.

A length l of such a stripline, shorted at the far end, has input impedance

$$Z_{IN}^{short} = Z_0 \tanh(\gamma l) = \frac{\tanh(\alpha l)\cot(\beta l) + i}{\cot(\beta l) + i\tanh(\alpha l)}. \tag{5.19}$$

Setting $\alpha = 0$ in this expression gives $Z_{IN}^{short} = i\tan(\beta l)$, which has poles at $\beta l = (2n-1)\pi/2$, $n = 1, 2, 3, ...$ Each of these poles corresponds to a resonant mode of the shorted line, each with resonant frequency $\omega_n = (2n-1)\pi v_p/(2l)$. The fundamental mode $n = 1$ corresponds to $l = \lambda/4$. Expanding 5.19 in small powers of αl and $\delta\omega$, where $\delta\omega$ is defined by

$$\beta l \approx \frac{\pi}{2}\left[(2n-1) + \frac{\delta\omega}{\omega_1}\right], \tag{5.20}$$

$$Z_{IN}^{short} \approx \frac{iZ_0}{(2n-1)\frac{\pi}{2}\frac{\delta\omega}{\omega_1} + i\alpha l} = \frac{(Z_0/(\alpha l))}{1 - 2i\left[\frac{\pi(2n-1)}{4\alpha l}\right]\frac{\delta\omega}{\omega_1}}. \tag{5.21}$$

Comparing this last result to 5.17, we see that it has the same form, where

$$R_r = \frac{Z_0}{\alpha l} \tag{5.22}$$

$$C_r = \frac{Q_n}{\omega_n R_r} = \frac{\pi}{4Z_0\omega_1} = \frac{C_l l}{2} \tag{5.23}$$

$$L_r = \frac{1}{\omega_n^2 C_r} = \frac{4Z_0}{(2n-1)^2\pi\omega_1} = \frac{8L_l l}{(2n-1)^2\pi^2} \tag{5.24}$$

$$Q = \frac{(2n-1)\pi}{4\alpha l} = \frac{(2n-1)\pi}{4}\frac{R_r}{Z_0} \tag{5.25}$$

$$Z_C = \sqrt{\frac{L_r}{C_r}} = \frac{4Z_0}{(2n-1)\pi} \tag{5.26}$$

We are interested only in the first mode, $n = 1$, in which case,

$$Z_{IN}^{short} = \frac{(R_l/4)}{1 - 2iQ\left(\frac{\delta\omega}{\omega_1}\right)} \tag{5.27}$$

$$R_r = \frac{4Z_0}{\alpha\lambda} \tag{5.28}$$

$$C_r = \frac{C_l\lambda}{8} \tag{5.29}$$

$$L_r = \frac{2L_l\lambda}{\pi^2} \tag{5.30}$$

$$Q = \frac{\pi}{4\alpha l} = \frac{\pi}{4}\frac{R_r}{Z_0} \tag{5.31}$$

$$Z_C = \sqrt{\frac{L_r}{C_r}} = \frac{4Z_0}{\pi} \tag{5.32}$$

$$\lambda = 4l \tag{5.33}$$

The design values of the resonator used in our experiment are $\omega_1 = 2\pi \cdot 6$ GHz, $C_l = 167$ pF/m, $L_l = 0.42$ nH/m, $Z_0 = 50\ \Omega$. This implies the remaining parameters are $\lambda = 2$ cm, $C_r = 0.42$ pF, $L_r = 1.7$ nH, $Z_C = 63.7\ \Omega$.

The internal resistance of the resonator, represented by R_l and R_1, would ideally be zero. The value Q here we identify as the internal quality factor and also denote it by Q_{int}, to distinguish it from the external quality factor Q_{ext}, which is due to coupling to the external circuit as described in §5.4.3.

5.4.3 Capacitively coupled quarter wave resonator

The previous section describes the simplest possible quarter-wave resonator formed in a transmission line, one which is completely isolated. But in order to measure the resonance characteristics, the resonator must be coupled to an outside circuit. Instead of having a true "open" (infinite impedance) at one end of the quarter-wave resonator, it is instead coupled to the outside circuit by a small coupling capacitance C_C, which provides a large, but finite, impedance at that point in the transmission line. In this way some signal can be input and output from the resonator but the basic resonance characteristic remains. The quantity we measure experimentally is the reflection coefficient Γ, also known as the scattering parameter S_{11}, the complex ratio of the reflected signal to the input signal.

As found in the previous section, the input impedance of the shorted quarter-wave resonator is (Eq. (5.19)),

$$Z_{IN} = Z_0 \tanh(\gamma l) \approx \frac{R_r}{1 + 2iQ_{int}\frac{\delta\omega}{\omega_0}} \tag{5.34}$$

Adding a coupling capacitance C_C in series with the resonator gives,

$$Z_{IN} = \frac{1}{i(\omega_0 + \delta\omega)C_C} + \frac{R_r}{1 + 2iQ_{int}\frac{\delta\omega}{\omega_0}}. \tag{5.35}$$

The coupling has two effects on the resonance. The additional capacitance shifts the center frequency of the resonator by an amount $\Delta\omega_0 = -2\omega_0 C_C Z_0/\pi$. The coupling to the outside line, which dissipates energy according to its characteristic impedance Z_0, also contributes to losses from the resonator. Whereas the quality factor Q_{int} describes the linewidth of the resonance due to internal losses in the resonator, losses from the resonator to the outside circuit also broaden the linewidth of the resonance by an amount Q_{ext}, where

$$Q_{ext} = \frac{\pi}{4\omega_0^2 C_C^2 Z_0^2}. \tag{5.36}$$

The total quality factor of the resonance is the reciprocal sum of the internal and external Qs,

$$\frac{1}{Q_{total}} = \frac{1}{Q_{int}} + \frac{1}{Q_{ext}}. \tag{5.37}$$

The reflection coefficient for the resonator in series with a capacitor is

$$\begin{aligned} S_{11} = & \frac{Z_{IN}-Z_0}{Z_{IN}+Z_0} = \frac{1+i\omega C_C Z_0[\tanh(\gamma l)-1]}{1+i\omega C_C Z_0[\tanh(\gamma l)+1]} \\ \approx & \frac{-2\pi i Q_{int}\delta\omega - \pi\omega_0 - (\omega_0+\delta\omega)C_C Z_0[2\pi Q_{int}\delta\omega - i(\pi-4Q_{int})\omega_0]}{-2\pi i Q_{int}\delta\omega - \pi\omega_0 + (\omega_0+\delta\omega)C_C Z_0[2\pi Q_{int}\delta\omega - i(\pi+4Q_{int})\omega_0]}. \end{aligned} \tag{5.38}$$

Some examples of the reflection coefficient as a function of frequency are shown in Fig. 5.5. For these calculations the values used were $\omega_0 = 2\pi \cdot 6$ GHz (unloaded), $C_C = 20$ fF, $Z_0 = 50$ Ω, which result in $Q_{ext} \approx 1000$. The internal Q was varied as described in the legend. These plots show the evolution of the reflected signal as Q_{int} changes. For $Q_{int} \gg Q_{ext}$, the reflected amplitude is nearly unity even at the resonant frequency, while the phase evolves through 2π as the frequency is swept through the resonance. As Q_{int} is made smaller, the reflected amplitude shows a dip at the (loaded) resonant frequency and the total phase evolution is less than 2π. When $Q_{int} < Q_{ext}$, the amplitude dip is reduced in magnitude and broadens, while the total phase excursion is smaller, tending to zero as $Q_{int} \to 0$. The phase evolution gives the most information about the resonance, but when Q_{int} is comparable to or less than Q_{ext}, the amplitude is adequate to determine the resonance characteristics. Fitting (Eq.

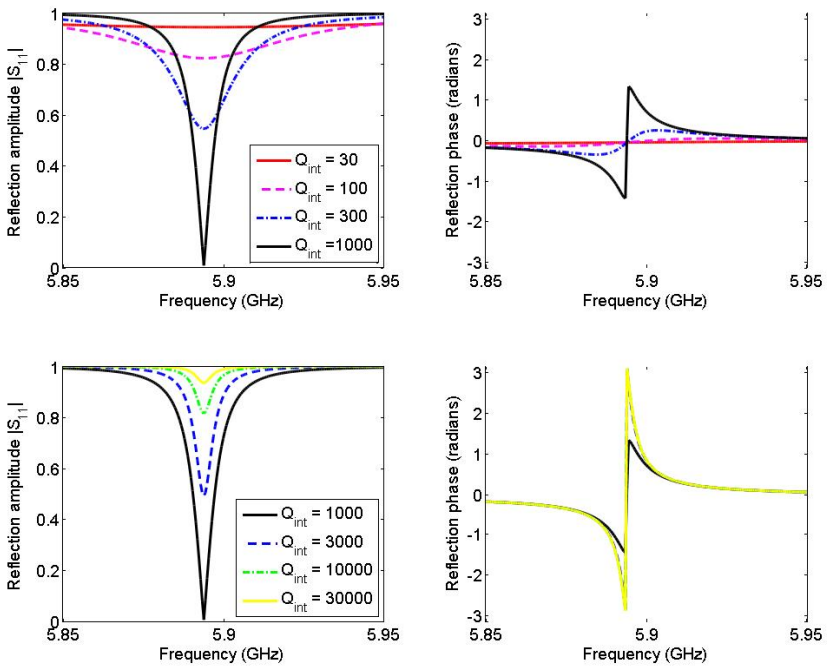

Figure 5.5: Examples of the reflection amplitude and phase of the capacitively coupled resonator model as a function of frequency.

(5.38)) to reflection measurements can extract the resonance parameters ω_0, Q_{int}, and C_C, which in turn can be related back to circuit model parameters L_r, C_r, R_r.

5.5 Experimental results

5.5.1 Electrical detection of microwave signal

We have also observed interactions between photons in the microwave resonator and 2DEG electrons in the MOSFET channel by measuring changes in the charge sensing channel conductance due to a microwave signal input to the resonator. An example of this type of conductance change is shown on the left side of Fig. 5.6. Plotted is the current through one of the charge sensing channels as a function of the frequency of an input microwave signal

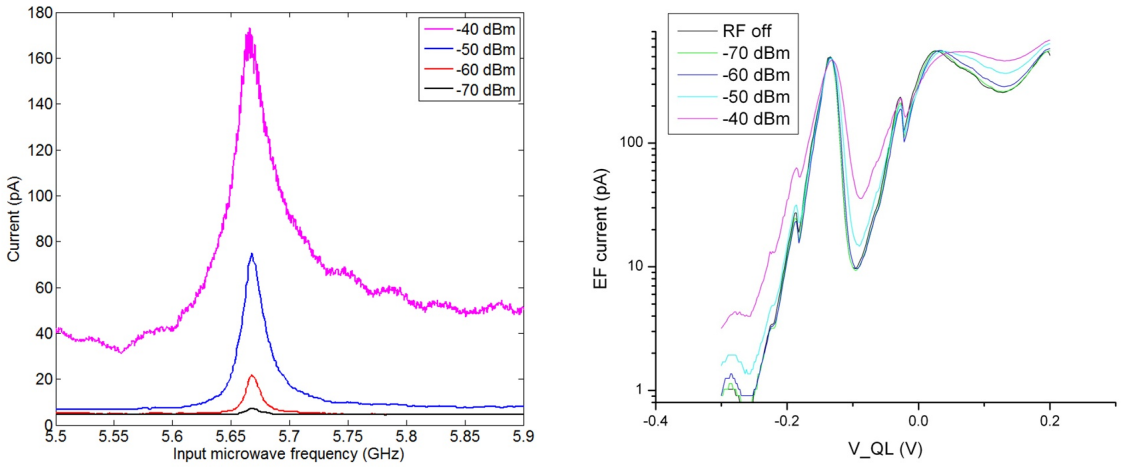

Figure 5.6: (left) Current through charge sensing channel EF as a function of input microwave frequency. (right) Current through charge sensing channel EF as a function of gate voltage V_{QL}, with microwave frequency fixed. In both cases the current was measured using a 125 μV lock-in drive signal.

to the resonator. When the input signal is off resonance, most of the microwave signal is reflected from the resonator and does not interact with the 2DEG. When the input signal is near the resonant frequency, near 5.670 GHz for this device, microwaves enter into the resonator and interact with the 2DEG. In this case, microwave power applied on resonance increased the conductance of the channel. At higher power, the conductance is increased even when the signal is off resonance (likely due to stray signal heating the whole device), but the strongest effect on the charge sensor conductance is still on resonance. The power levels reported are the power applied at the output port of the signal generator; about 20 dB of loss is present in the coaxial waveguides between the signal generator and the sample.

On the right side of Fig. 5.6 is a plot showing the effect of the microwave signal on the conductance of the charge sensing channel EF as its tuning is changed. The channel was tuned so that it is in the regime where the conductance fluctuates with respect to the voltage on gate V_{QL}. In this regime, as the microwave power is increased the primary effect on the channel conductance is to increase the conductance at the conductance minima, effectively

reducing the magnitude of the conductance fluctuations. This is consistent with an increase in the electron temperature of the channel [ABG02, WHH05]. Microwave photons in the resonator are absorbed by 2D electrons in the MOSFET channel, which heats the channel electrons and in turn influences the conductance through the point contact constriction. The channel is acting as a very sensitive bolometer. The microwave resonance could be detected with as little as -75 dBm power output from the signal generator, corresponding to about -95 dBm (0.3 pW) power applied at the resonator itself.

To quantify the increase in temperature as a the microwave signal was applied, we tuned the channel EF more closed so that it exhibited Coulomb blockade, as shown in Fig. 5.7. The width of the Coulomb blockade resonances increases with increasing temperature. If the resonance is in the "orthodox" transport regime where many quantum energy levels of the quantum dot can participate in transport, the shape of the conductance peak is given by [KMM97, ABG02]

$$\frac{G}{G_{max}} = \cosh^{-2}\left(\frac{\alpha(V_g - V_0)}{2.5k_B T_e}\right) \tag{5.39}$$

where G is the conductance of the channel, G_{max} is the maximum conductance of the peak, α is the "lever arm" parameter representing the strength of the capacitive coupling with the gate, V_g is the gate voltage, V_0 is the gate voltage at which the peak conductance occurs, and T_e is the electron temperature. A Coulomb diamond measurement established the gate lever arm factor $\alpha = 0.013$ eV/V for the data shown in Fig. 5.7. For each input power level (and more not shown in Fig. 5.7) the three Coulomb blockade peaks near $V_{RL} = -0.4$ V, $V_{RL} = -0.6$ V, and $V_{RL} = -0.76$ V were fit to Eq. 5.39 to determine the electron temperature. The results of the fits are shown in Fig. 5.7 at right. Squares mark the average temperature determined from the three peaks while the error bars indicate the range of values. The black dashed line on the plot indicates the base temperature of the ^{3}He bath in the refrigerator reported by its thermometer. A difference of about 10% between the temperatures measured by the width of the Coulomb blockade peaks at the smallest input powers and that reported by the refrigerator thermometer is attributable to uncertainty in the determination of α. It is worth noting that at the highest power applied, -30 dBm, the

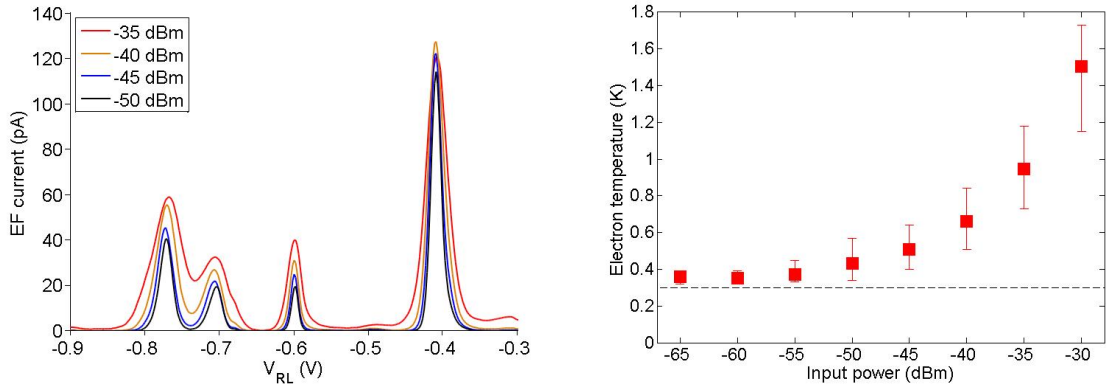

Figure 5.7: (left) Current through the channel EF as a function of gate voltage V_{RL}. The channel has been tuned so that it exhibits Coulomb blockade. Different curves show different amounts of power applied to the microwave resonator. Increasing power broadens the peaks, indicating an increase in the electron temperature in the MOSFET channel. (right) MOSFET channel electron temperature as a function of microwave power applied to the resonator, at the resonant frequency 5.670 GHz. The dashed black line indicates the refrigerator base temperature as indicated by the refrigerator thermometry.

electron temperature increased by a factor of 5, but the background temperature of the ^{3}He bath did not increase detectably ($\Delta T < 0.1$ mK). The heating is specific to the electrons in the MOSFET channel.

5.5.2 Reflected microwave signal

Fig. 5.8 shows measurements of the amplitude of the microwave reflection as a function of frequency (the input power in this case was -40 dBm). The overall structure of the signal shows a nearly periodic fluctuation with a period of 43.3 MHz. This periodic fluctuation corresponds to a resonance formed in the coaxial cable in the refrigerator, between the directional coupler (which is not perfectly impedance matched to the transmission line) and the sample holder. The distance between the two is about 2.5 m and the phase velocity of microwaves in the line is roughly $2 \cdot 10^8$ m / s, which causes a standing wave with modes

spaced by 40 MHz, which is about what we observe. One experimental challenge is that the reflected signal from our resonator is mixed in with this background reflection. To identify the resonance itself, we take the same scan of reflected microwave power versus frequency at several different settings of the accumulation gate voltage V_T, as shown in Fig. 5.8. As V_T is increased, at first there is no change in the reflected signal, but above a threshold of about V_T =1.7 V, a change in the reflected signal appears at about 5.67 GHz, which is the same resonant frequency as observed by electrical detection (Sec. 5.5.1). The magnitude of the feature increases as the accumulation gate voltage is increased. It is most clearly seen by subtracting the background signal, as measured at $V_T = 0$ V, which is shown in Fig. 5.8 at bottom.

The shape of the resonance feature is a bit unusual, because it represents the amplitude of a complex signal with two parts: the background reflection of the coaxial cable, and the resonator itself. These signals add in quadrature, but we measure only the reflected power, with no phase information. Instead of a simple dip in the reflected power we see on each side of the dip is an increase in the total reflected power, where the phase of the resonator reflection and the phase of the background reflection are commensurate and the two signals add constructively. The combined signal can be modeled in the following way. The background signal is represented by $a(\omega)$, whose amplitude $|a(\omega)|$ is known from measurements, and whose phase is assumed to vary linearly with frequency at a rate that corresponds to a phase change of 2π over the observed 43.3 MHz period of the background signal. The two signals with the resonator reflection,

$$c(\omega) = |a(\omega)| \exp(i\omega t_p) + bS_{11}(\omega) \tag{5.40}$$

where b is a complex constant amplitude of the resonator reflection and c is the total reflected signal. The power $|c(\omega)|^2$ is the experimentally measured quantity. This model has a total of five free parameters: an amplitude and phase for b, plus the resonator parameters ω_0, Q_{int}, and C_C (see Eq. (5.38)). An example of the fit to one background-subtracted amplitude data set is shown in Fig. 5.9. The model fits well and the presence of nuisance parameters b does not significantly change the estimates of ω_0, Q_{int}, and C_C.

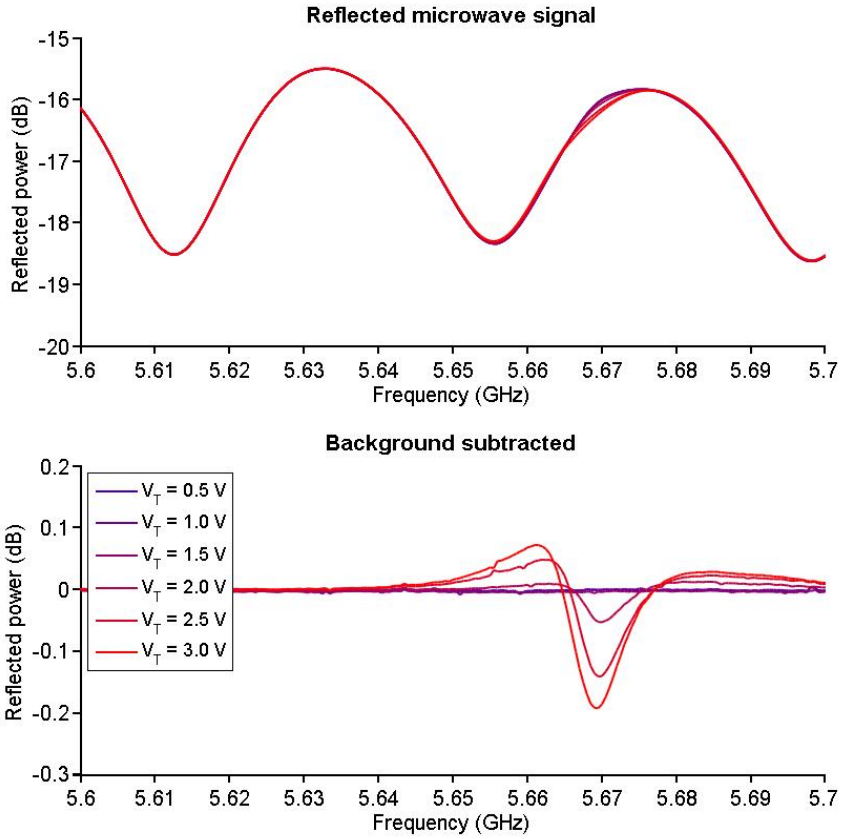

Figure 5.8: (top) Microwave reflection amplitude vs. frequency. Several different curves are shown at with various voltages V_T applied to the accumulation gate. (bottom) Same as top, but with the background signal $V_T = 0$ subtracted.

A more complete data set is shown as an intensity plot in Fig. 5.10. In this data set the input microwave power was -40 dBm. The background-subtracted microwave reflection is shown plotted as a function of input frequency and accumulation gate voltage. The appearance of the resonance is clear at about V_T=1.7 V and the resonance feature increases in amplitude and in width as the accumulation gate voltage is increased. This is consistent with increasing dissipation in the resonator as the accumulation gate voltage is increased. This statement can be made quantitative by fitting the model (Eq. (5.40)) to the data in Fig. 5.10. The model parameters b and C_C are assumed to be independent of V_T (since they

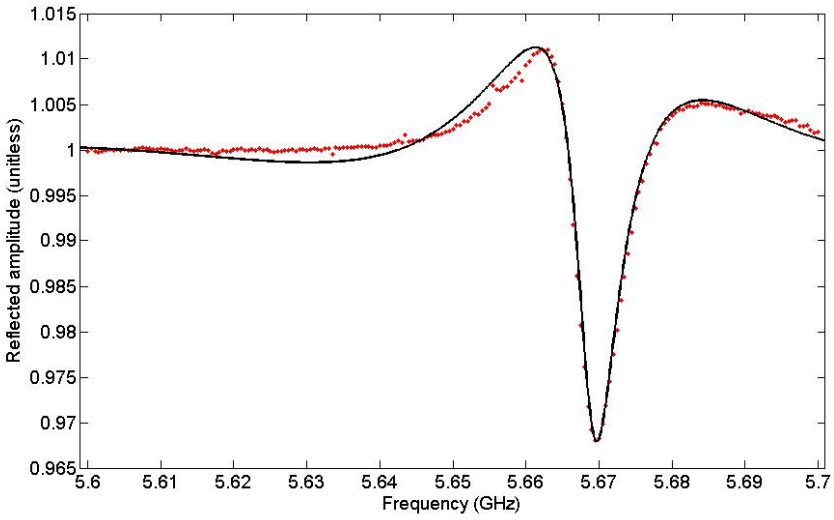

Figure 5.9: Example of microwave reflection power data with the background subtracted. The black line is a fit to the data points (red), as described in the text.

represent quantities that are external to the resonator) and are fit to a value that is constant across the data set while Q_{int} and ω_0 are fit individually to each frequency scan at fixed V_T. The results of the fits are shown in Fig. 5.11 for ω_0 and Q_{int}. The constant values that were found were $b = 0.026 + 0.14i$ and $C_C = 19$ fF ($C_C = 19$ fF corresponds to Q_{ext}=650). In Fig. 5.11 we can see that the general trend is a decreasing ω_0 and Q_{int}. These correspond to an increase in the capacitive loading and resistive loss in the cavity, respectively. Also shown in Fig. 5.11 are the RLC model equivalent resistance R_r and capacitance C_r for the resonator circuit, under the assumption that the resonator's total impedance is the design value, L_r =1.7 nH [2]. We observe an increasing capacitance as the accumulation gate voltage is increased, consistent with a capacitive loading by the MOSFET electrons on the resonator. The total change in capacitance is only about 1 fF but it is easily detectable as a shift in the resonant frequency. The change in the linewidth is due to an increased loss in the resonator-MOSFET system as the electron density in the MOSFET is increased. The internal quality

[2]MOSFET electrons have no measurable impact on the resonator inductance since they are located at the open end of the resonator, where the current is zero.

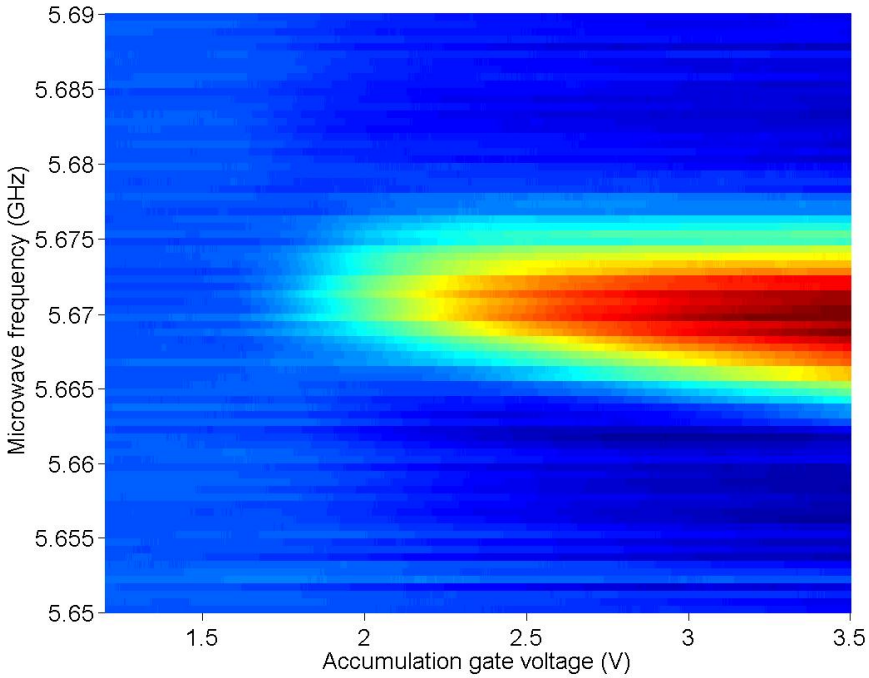

Figure 5.10: Reflected microwave power (background subtracted) as a function of microwave frequency and accumulation gate voltage V_T.

factor of the resonator itself is on the order of $10^4 - 10^5$ when the accumulation gate voltage is zero, but it clearly drops dramatically as the electron density in the MOSFET channel is increased by increasing the voltage on the accumulation gate voltage. Fig. 5.11 shows that the change in reflected power is first detectable near V_T=1.8 V, as the internal quality factor is about 300. It continues to drop significantly as the accumulation gate voltage is further increased.

The effects shown in this section are only due to the gross influence of 2DEG electrons in the MOSFET. In the next section we discuss efforts to make more sensitive measurements of the microwave resonator by applying a small modulation signal to the gates of the device and measuring the microwave reflection response to it.

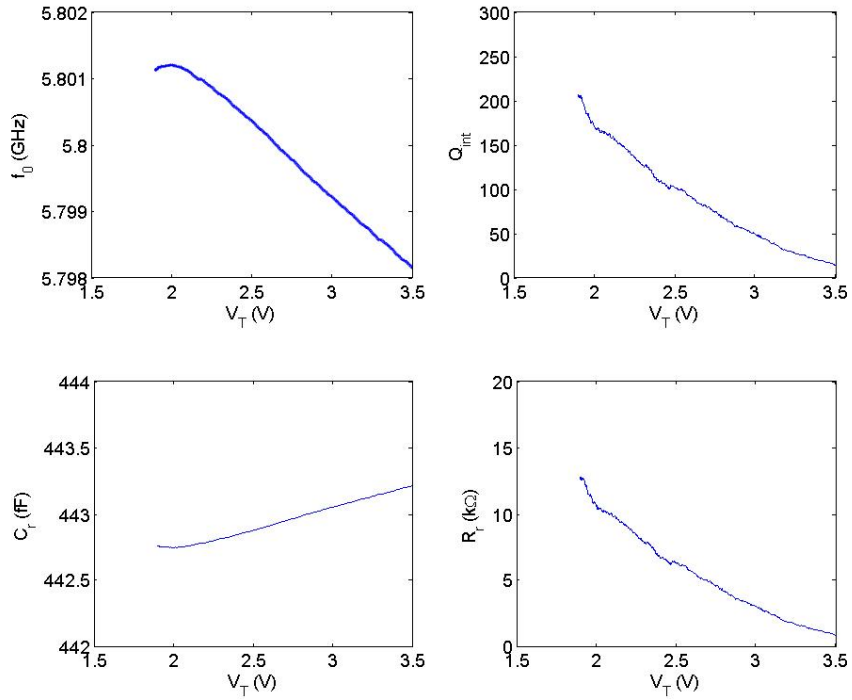

Figure 5.11: Results of fitting the data in Fig. 5.10 to the resonator reflection model. The center frequency f_0 (upper left) and internal quality factor Q_{int} are determined as a function of V_T by fitting. The equivalent resistance R_r and capacitance C_r are computed from f_0 and Q_{int} according to Eq. 5.18.

5.5.3 Modulated reflection amplitude measurements

The results of the previous section describe the findings for the gross behavior of the system as the electron density in the MOSFET channel is increased. In order to observe changes in the microwave resonance more sensitively, we used a Stanford Research SR830 Lock-in Amplifier to measure the change in the reflected microwave power due to a small change in gate voltage. A low-frequency modulation signal (typically 400 Hz, 4 mV RMS amplitude) from the lock-in amplifier was applied to one of the gates of the device, and the output of the microwave detector was connected to the input port of the lock-in amplifier. Assuming the modulation

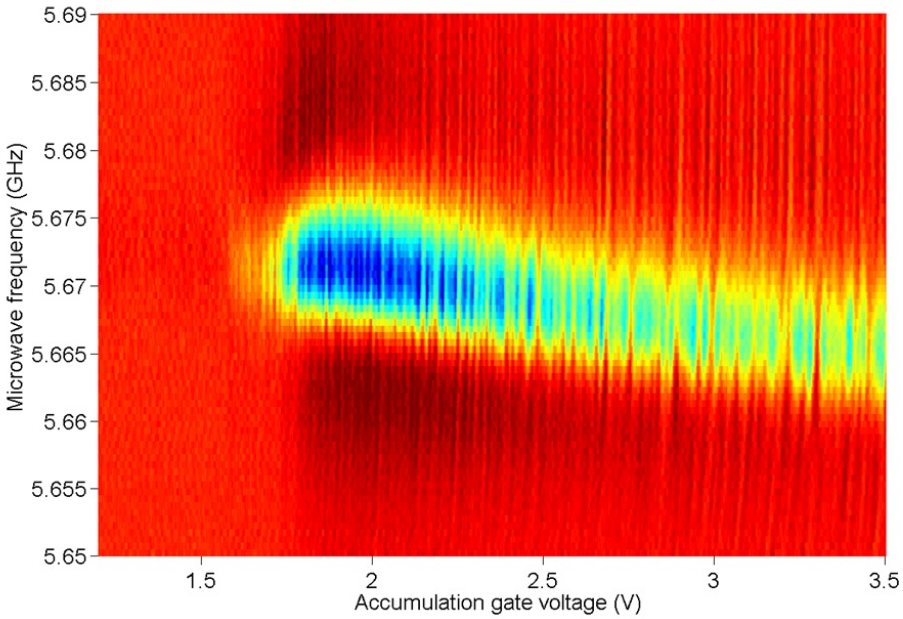

Figure 5.12: Microwave reflection modulated by the accumulation gate as a function of frequency and accumulation gate voltage.

amplitude is small enough, the lock-in measurement is proportional to the derivative of the reflected power with respect to gate voltage. This is a much more sensitive measurement than measuring the reflected power directly, and it also automatically eliminates the background signal, which is not changing with respect to gate voltages.

Fig. 5.12 shows the microwave reflected power, modulated by the accumulation gate, as a function of frequency and accumulation gate voltage. The input power in this case was -40 dBm. A similar structure appears as was seen in the unmodulated reflection signal: a resonance feature appears as the accumulation gate voltage is increased to 1.8 V and greater. In this case the resonance feature is not smooth. It contains a number of small fluctuating features that were not seen in the unmodulated signal (Fig. 5.10). A scan of frequency and gate voltage taken at higher resolution is shown in Fig. 5.13. These features are reproducible from one voltage scan to the next. We identify these features as representing shifts in the microwave resonance due to interaction with individual charging events in the MOSFET.

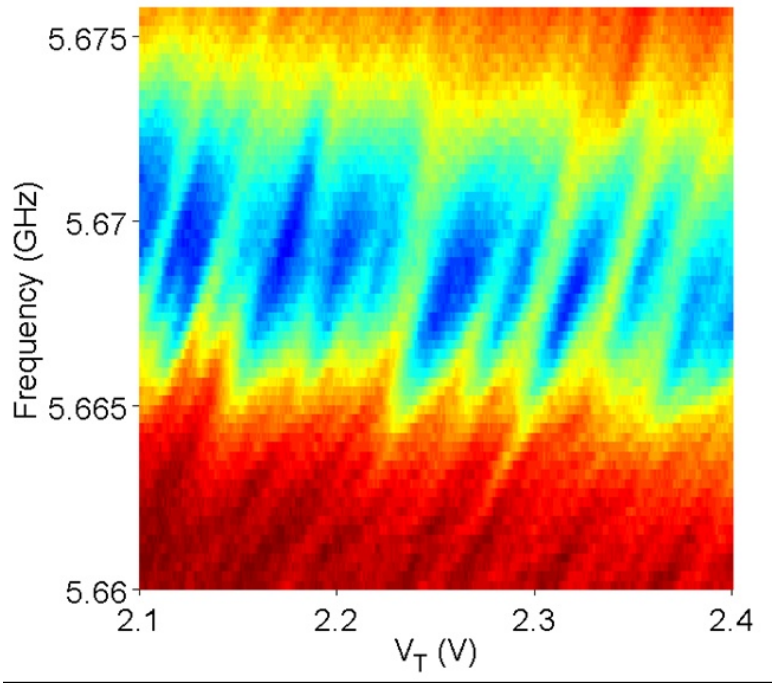

Figure 5.13: Microwave reflection modulated by the accumulation gate as a function of frequency and accumulation gate voltage. Same as Fig. 5.12 but with higher scan resolution.

These features do not seem to correlate with measurements of transport or charge sensing of the double quantum dot system itself, so we cannot conclude that they represent an interaction with the quantum dot system as intended. Instead it is likely that they are charging events from charged defect states at the Si-SiO_2 interface, near the resonator gates. The fringing field of the microwave resonator is interacting with such charged defect states, each of which are shifted into and out of equilibrium with the 2DEG reservoir by the dc voltages on the gates. When a charged defect state is tuned by the gate voltages so that its chemical potential is near to the Fermi level of the 2DEG, the electron (or hole) can transfer to and from the 2DEG, and this motion acts as a small amount of additional capacitance in the microwave resonator, shifting its resonant frequency downward. As the gate voltage is scanned, these defects pass in and out of tune with the Fermi level of the 2DEG reservoir, so we observe both positive and negative changes in the center frequency of the resonator.

Fig. 5.14 shows six data sets taken with the gate modulation technique. In the three sub-figures on the left the modulation signal was applied to the accumulation gate. In the three sub-figures at right the modulation signal was applied to gate RL. In all cases the input microwave power was -40 dBm and the input frequency was 5.670 GHz (on resonance). In the top two figures, the dc voltages scanned were V_{top} and V_{RL} (V_{RR} was fixed at 0 V); in the middle two figures the voltages scanned were V_{top} and V_{RR} ($V_{RL} = 0$ V); in the bottom two sub-figures, the voltages scanned were the two plunger gates V_{RL} and V_{RR} ($V_T = 2.1$ V).

At top left, the accumulation gate is modulated so we see those features that respond to a change in top gate voltage. We see two types of features: one set of horizontal lines, and one set of diagonal lines. The horizontal lines represent features that couple only to the top gate voltage; the diagonal lines represent features that couple to both the top gate and gate RL. In the middle left plot we see a similar looking pattern with respect to the RR gate: one set of features couples to both V_{RR} and V_T, while another is coupling only to V_T. In the lower left plot, we again see two types of features, but in this case we see that one group of features is horizontal (coupling only to V_{RR}) and the other is vertical (coupling only to V_{RL}).

Comparing the three plots on the left of Fig. 5.14 (where the modulation is applied to the accumulation gate) with the corresponding plots on the right (where the modulation is applied to gate RL), we see that the difference between them is always that one set of lines disappears, and the set of lines that disappears is the one that is not influenced by V_{RL}. We expect this since the modulation is applied to RL; any features that do not respond to V_{RL} will not be modulated and will not be observed in this configuration. At top right, we see the diagonal lines that couple to both V_{RL} and V_T, but not the horizontal features that were seen at top left. Similarly, at middle right we see only horizontal lines; the diagonal lines are not seen as a function of V_{RR}. And at lower right, only the vertical lines, which are coupled to V_{RL}, appear. The horizontal features, coupled to V_{RR}, are not seen.

These six plots together are all consistent with the hypothesis that there are charge traps or quantum dots in the MOSFET which are influencing the microwave resonator. There are two types of such traps, those that couple to gate RL, and those that couple to RR;

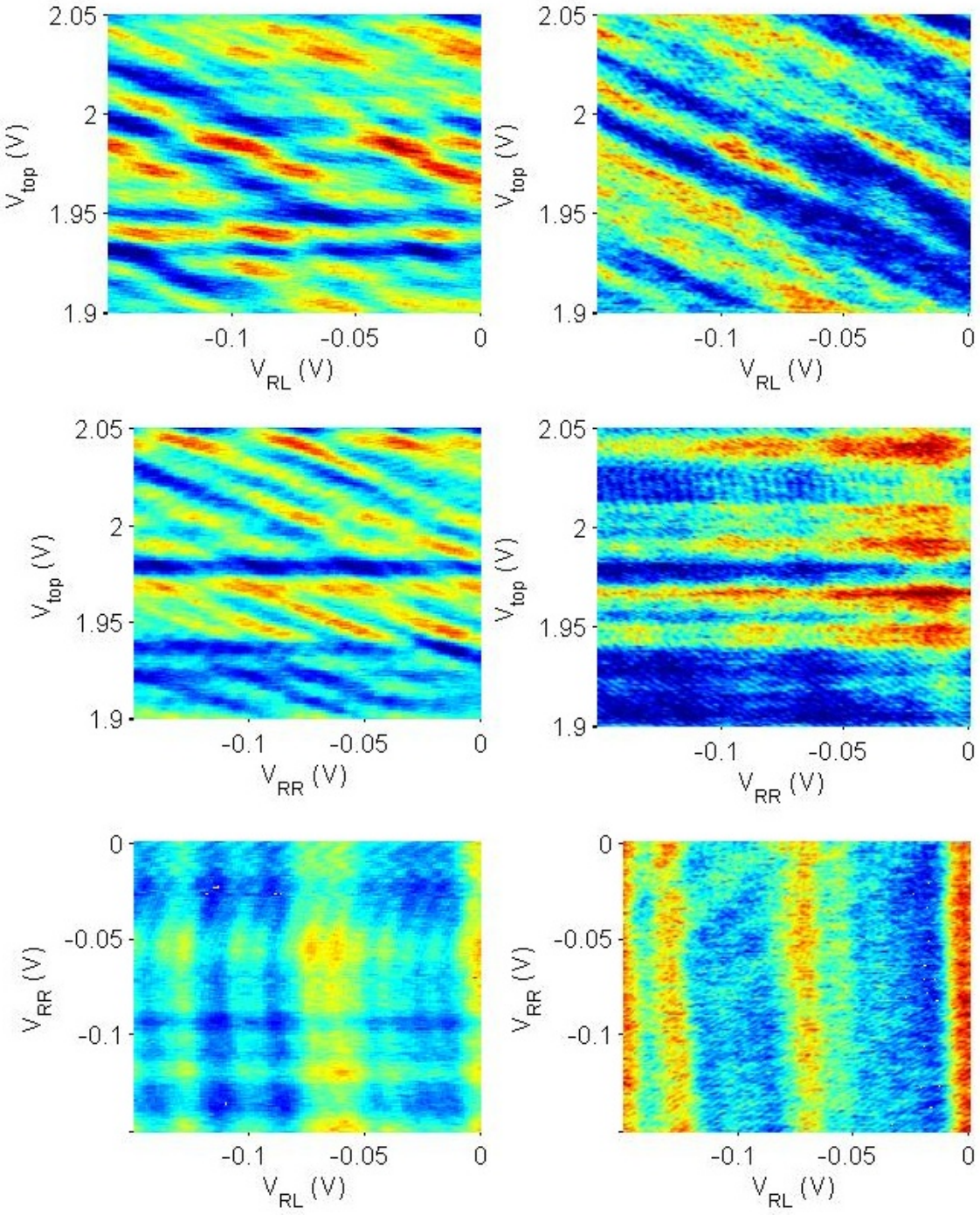

Figure 5.14: Modulated reflected microwave power, on resonance, as a function of gate voltages as described in the text.

both types couple to the accumulation gate. We do not observe any that couple to both plunger gates, which would show as diagonal lines in the bottom two plots in Fig. 5.14. The double quantum dot itself couples to both gates (as evidenced by diagonal lines in similar voltages sweeps measuring either transport or charge sensing of the dots), so it does not appear to be the double quantum dot that is interacting with the microwave resonator. Instead it appears we have either two isolated quantum dots, or many charge traps that each couple to one plunger gate or the other. We hold the latter scenario to be more likely, although one issue with that interpretation of the data is that the diagonal lines in Fig. 5.14 are all nearly parallel, which implies that each feature's relative coupling strength between the accumulation gate and the plunger gate is equal. This seems unlikely for a random distribution of defect states; it may be that either there are two deep quantum dots and we are observing multiple electronic transitions from the same dot, or that for some reason all of the charge traps that couple well to the microwave resonator all have about equal coupling strength.

5.6 Conclusions

5.6.1 Findings

The experiments we have performed so far on our microwave resonator - double quantum dot devices have clearly demonstrated coupling between the microwave resonator and 2D electrons in the MOSFET channel. In one respect this is encouraging, because the resonator can respond to electrons in the MOSFET, possibly even single electron charging events. However we have not yet demonstrated a clear interaction between the microwave resonator and electrons specifically in the double quantum dot. We clearly see a gross effect of the electrons in the MOSFET channel on the microwave resonator. This interaction can be seen both in the microwave reflection from the resonator element, and by observing a change in the conductance of a charge sensing channel as microwave power is applied to the resonator. The interaction between 2DEG electrons and the microwave resonator may itself have some

scientific value, although in the present experiment it represents an unwanted complication for observing the double quantum dot.

5.6.2 Outlook

The decrease in the internal quality factor and the increase in the MOSFET electron temperature are both consistent with the absorption of microwave energy by 2D MOSFET channel electrons. The capacitive shift in the resonance frequency due to these electrons is not a serious concern for the double quantum dot experiment, but the fact that the interaction between 2D electrons and microwaves in the resonator is *lossy* a serious concern for this experiment. The current amount of loss is certainly too much for us to be able to achieve the strong coupling regime, and probably limits our ability to detect a dispersive shift of the resonator with respect to the quantum dot state. At the highest V_T, the quality factor is on the order of 10, which is too small to observe a dispersive shift of the scale we expect for the double quantum dot system. At more modest V_T, Q_{int} is on the order of 100 or more, which may be large enough to observe a dispersive shift, but in order to demonstrate strong coupling the Q_{int} should be at least on the order of 1000, and ideally should be much higher than that. In order to achieve our experimental goals, the system will have to be redesigned to minimize the interaction between the microwave resonator and the 2DEG electrons. It is worth noting that a similar experiment in a GaAs quantum dot system observed similar heating of the 2DEG by absorption of microwaves in the resonator [FLB11]. This group was able to achieve a dispersive measurement of the quantum dot by redesigning the device to minimize the interaction between the resonator and the 2DEG [FLB12].

We conclude that it should be possible to achieve a dispersive readout of the double quantum dot state with the microwave resonator in a slightly modified device that was redesigned to minimize the interaction between the microwave resonator and the 2DEG electrons. In the current design the quantum dot is approximately 50 μm from the edge of the MOSFET accumulation gate, a distance over which the resonator leads may interact with the 2DEG and any charge defect states that exist in the silicon, the oxide, or at the

interface of the two. It should be possible to reduce this distance to only a few microns (or possibly less) with no impact on the quantum dot performance. This simple change may be enough to significantly reduce or eliminate the resonator interaction with the 2DEG and defect states. Such a reduction will probably be enough to make dispersive readout possible.

The possibility of achieving the strong coupling regime in this system is more dubious. The demand on the quality factor is greater ($Q \gg 10^3$) than for dispersive measurement, and it is not clear whether the interaction with the 2DEG can be eliminated to that degree. Another issue is that other similar experiments that have observed that the dephasing of the double quantum dot system may be too rapid to allow strong coupling, at least in GaAs [FLB12]. There is reason to believe that silicon quantum dots will have more favorable dephasing times [GHW05], but this needs more experimental confirmation.

CHAPTER 6

Data analysis for real-time observations of electron tunneling events

Ability may get you to the top, but it takes character to keep you there.

- J. R. Wooden

This chapter describes a novel approach to analysis of observations of individual electron tunneling events that was developed by this author. The experimental data presented here came from two experiments: one performed by Xinchang Zhang and others in our lab, which was described in a paper published in Physical Review B [ZMB09], and a second performed by Ming Xiao and colleagues at the University of Science and Technology of China [LXC12]. This author generated all simulated data sets. Part of this chapter is adapted from a paper published in Physical Review B [HZJ09], with some added details and new results.

A note about index convention: The generally used convention in the hidden Markov model literature is to specify the transition matrices in a Markov equation such that if Q_{ij} is a matrix element, it represents the rate of transition *from* state i *to* state j, and probability vectors are represented as row vectors. This is the opposite of the usual convention used in physics literature, in which Q_{ij} is the rate of transition *from* state j *to* state i. In this chapter, and only in this chapter, we follow the convention of the HMM literature. In Chapter 4 we specified a rate equation model *which used the opposite convention*, because that convention is more commonly used in physics literature in general. I apologize for any confusion.

6.1 Introduction

6.1.1 Analysis problem

As discussed in earlier chapters, the conductance of a quantum point contact (QPC) [WHB88, But90] or single electron transistor (SET) [FD87, LPW91] near to a quantum dot can be sensitive to the charge on the quantum dot, with good enough resolution to determine when individual electrons enter or leave the dot. If the charge detection bandwidth is sufficient we can observe changes in the charge state in real time as electrons tunnel between the quantum dot and its lead(s) [GLS09, FFH09]. These observations are valuable because they show the dynamics of the quantum dot electrons at the most basic level. The dynamics depend on several interesting characteristics of the dot-lead system that we would like to study: the number of quantum states in the quantum dot, their energy levels, coupling between states in the quantum dot and states in the lead, allowed or disallowed transitions between states, and the density of states and occupation of states in the lead. Tunneling events are stochastic in nature, so in order to gain information about these things we must extract it from the statistics of the tunneling events. Doing so allows us to study electron spin dynamics at the thermal energy scale and below; most experiments (such as described in Chapter 4) require that the energy scale exceed the thermal energy scale.

This chapter describes a new approach to analyzing charge sensor data in quantum dot experiments, primarily based on the Hidden Markov Model (HMM). The HMM is an excellent type of model for the system we are studying and it provides a way to extract as much information as possible about the quantum dot system from the data available. HMM analysis has the following advantages:

- A simple mathematical model represents the system being studied, with no prior assumptions about the physics involved.
- Transition rates between different states can be estimated directly by fitting a model to the data.

- "Hidden" states which cannot be seen directly in the system can be detected from their influence on the electron transition statistics.
- A HMM can model noise in the measurements directly, making its parameter estimates very robust against noise.

In this chapter, first we will discuss the physics of RTS and its relevance to quantum dot experiments. Next we will outline the theory of hidden Markov models and explain how it relates to the data analysis we wish to perform. We will discuss the results of HMM analysis on three types of data: simulated RTS data generated specifically for evaluating the HMM analysis, and data from two different experiments on GaAs quantum dots. We then discuss some new directions that we have started to develop for this type of analysis and conclude by summarizing our findings.

6.1.2 Random telegraph signals

When the potential of the lead(s) of the quantum dot are tuned so that there are both occupied and unoccupied states in the lead at the electrochemical potential level of a quantum dot state, ordinary thermal fluctuations cause electrons to spontaneously transition on and off of the dot, a process which can be observed in real-time by a QPC or SET acting as a charge sensor. The conductance of the charge sensor will show random transitions back and forth between two levels that are commonly referred to as a random telegraph signal (RTS). An example of RTS data is shown in Fig. 6.6. Besides deliberately engineered quantum dot experiments, RTS are a widespread natural phenomenon in solid state physics that are often observed in mesoscopic devices [KDW89]. Quantum dots which are tuned to produce an RTS can serve as a controllable model system for studying the behavior of these naturally occurring defects.

The basic model for an RTS is the two-level fluctuator (TLF), in which there is a charge which can sit on one of two sites, separated by an energy barrier. Due to thermal (or other) fluctuations it can switch back and forth between these two sites. The two different states

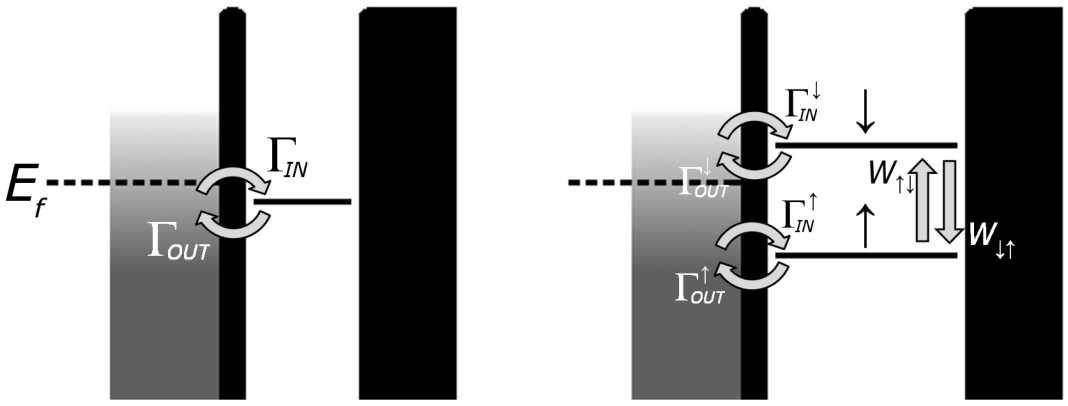

Figure 6.1: (left) Diagram of a two-state model for a RTS system: a single allowed electron state tunnel coupled to a thermal reservoir of electrons. (right) A three-state model for an RTS system, in which there are two distinct states an electron may occupy.

each have a different influence on the measured quantity (*i.e.* current through a narrow channel), so this switching is observed as an RTS. The combined action of an ensemble such TLFs is one explanation for the origin of $1/f$ noise, which is ubiquitous in semiconductor devices [Wei88].

While an RTS exhibits only two distinct conductance levels, it is possible these two levels correspond to more than two states of a microscopic system. Two possibilities we can consider are illustrated in Fig. 6.1. At left is the potential diagram of a two-state system, in which the quantum dot has a single allowed state for the electron. The electron state of the quantum dot can be empty, $|0\rangle$, or occupied $|1\rangle$. The central line in this figure represents the chemical potential of the $|0\rangle \leftrightarrow |1\rangle$ transition, separated from a Fermi reservoir of electrons with Fermi level E_f. The rates of transition are Γ_{IN} for an electron to tunnel into the dot, and Γ_{OUT} for an electron to tunnel out. The right half of Fig. 6.1 is shown a three-state system. In this case the quantum dot state can be empty, $|0\rangle$, occupied in the ground state $|\uparrow\rangle$, or occupied in the excited state $|\downarrow\rangle$. In this case there are two chemical potential levels

for the two spin states, which are separated by the Zeeman energy. There are independent tunnel rates for each spin; $W_{\downarrow\uparrow}$ and $W_{\uparrow\downarrow}$ correspond to the rates of transition between two spin states (spin flips). We use the notation $|\uparrow\rangle$ and $|\downarrow\rangle$ to suggest two distinct spin states because those are the two states we will study in §6.6, but these two states need not be spin states. We can also consider models with more than three states, if appropriate. In both models, a quantum dot is coupled by a tunneling barrier to a Fermi reservoir of electrons. Then electrons will tunnel back and forth between the reservoir and the quantum dot. The rates at which electrons tunnel into the quantum dot are proportional to a bare tunneling rate Γ_0 times the fraction of occupied states in the lead,

$$\Gamma_{IN} = \Gamma_0 f\left[\frac{(\mu - E_f)}{k_B T}\right] \tag{6.1}$$

where f is the Fermi distribution, μ is the electrochemical potential of the quantum dot state, E_f is the Fermi level of the reservoir, k_B is the Boltzmann constant, and T is the temperature of electrons in the reservoir. The rate for electrons to tunnel out of the quantum dot is proportional to the fraction of unoccupied states in the reservoir, $1 - f$:

$$\Gamma_{OUT} = \Gamma_0 \left\{1 - f\left[\frac{(\mu - E_f)}{k_B T}\right]\right\}. \tag{6.2}$$

If the system is in thermodynamic equilibrium, the ratio of the tunnel-in rate to the tunnel-out rate is $\Gamma_{IN}/\Gamma_{OUT} = \exp[-(\mu - E_f)/(k_B T)]$.

Since the absolute number of electrons is not important for discussing the RTS itself, for convenience we will call the two occupation numbers 0 electrons and 1 electrons, with the understanding that there may be an arbitrary number N of other electrons in the quantum dot which remain fixed on the quantum dot, and don't participate in the fluctuation.

It is non-trivial to see whether the three-state model might apply for a given RTS, which can detect only the charge state of the quantum dot. It is always clear there are at least two states, but the states $|\downarrow\rangle$ and $|\uparrow\rangle$ in the three-state model are not directly distinguishable. We may say that one of the three states is "hidden". But if the average transition rates for electrons to tunnel out of the quantum dot is different for each of these states, it is possible

to find evidence for the hidden state in the statistics of the electron transition times. In this chapter we discuss our strategy for detecting such states with statistical analysis of the signal, and the conditions on the system that make detection possible.

6.2 Hidden Markov models

6.2.1 Background

A HMM is a statistical model, diagrammed in Fig. 6.2, in which the state of the system is a Markov process that cannot be observed directly. At regular time intervals the system produces an observation that depends probabilistically on the state that the system is in at the time. Information about the sequence of states through which the system passes must be inferred indirectly from the observations. In our application, the Markov process models the electron state of the quantum dot and the observations are the charge sensor conductance data. The state is "hidden" because the measured signal does not have a one-to-one correspondence with the state of the system. The conductance measurement only depends on the charge state of the quantum dot, not on any other degrees of freedom such as spin, valley, or orbital quantum numbers. The signal also inevitably contains experimental noise, which further obfuscates the state of the system. The HMM is well suited for dealing with both of these limitations. Using HMM analysis we can extract the transition rates between the various states of the system. In favorable cases we can also infer the existence of multiple states with the same number of electrons, *i.e.* distinct orbital or spin states, that cannot be distinguished directly by a charge sensor.

Hidden Markov modeling is a well-developed statistical field dating from the 1960s. The key algorithm that enables inference in HMMs to be computed efficiently was originally proposed by Baum, *et al.*, and came to be known as the Baum-Welch algorithm [BE68]. It was later shown to be part of a larger class of useful maximum-likelihood estimation algorithms called expectation maximization (EM) algorithms [DLR77]. HMMs have been applied to data analysis problems in a variety of other fields, including automatic speech recognition

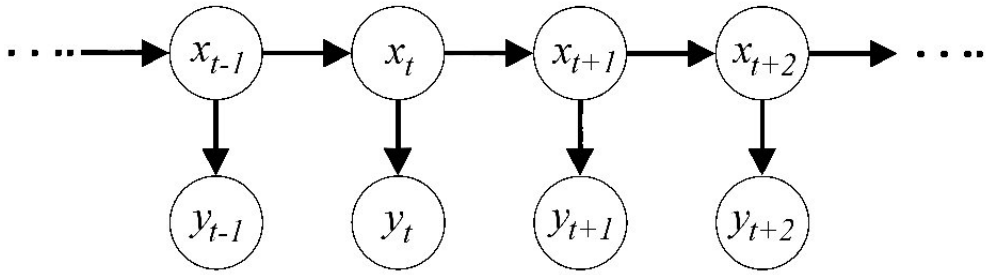

Figure 6.2: Diagram of a general HMM, which consists of a Markov process $\boldsymbol{x} = \{x_1, x_2, \ldots, x_N\}$ and a sequence of observations $\boldsymbol{y} = \{y_1, y_2, \ldots, y_N\}$. Arrows indicate conditional dependence between variables. The state x_t depends only on the previous state x_{t-1} and the observation y_t depends only on the current state x_t. In our implementation the Markov process $\boldsymbol{x}$ represents the electron state of the quantum dot as it changes over time and the observations $\boldsymbol{y}$ represent charge sensor measurements.

[Rab89], financial modeling [BH04], and a number of biological applications. The type of model proposed here is particularly closely related mathematically to HMMs developed in the study of biological ion channels [FR86, QAS00, RE08]. A very good introduction to HMMs is given by Rabiner [Rab89]; another is by Visser [Vis11]. A recent comprehensive text on the topic is by Cappe, *et. al* [CMR05].

6.2.2 Discrete time HMM

In most HMM applications and in our original approach to this problem [HZJ09], the state of the system is modeled as a discrete-time, first-order Markov process. At a sequence of times $t_n = n\Delta t$ the system is assumed to be in one of a finite number M of definite quantum states, denoted by $X_1, X_2, ...X_M$. The system transitions randomly between states, with the probability of the system being in state X_j at time t_n depending only on the state of the system at time t_{n-1}. Let x_n represent the state of the system at time t_n. We define the transition matrix of the system, A, whose elements are the probability of being in state X_j

at time t_n, given that the system was in state X_i at time t_{n-1}:

$$A_{ij} = P(x_n = X_j | x_{n-1} = X_i). \tag{6.3}$$

Introducing a row probability vector $\boldsymbol{p}(t_n)$ such that $p_i(t_n)$ is the probability that the system is in state X_i at time t_n, the evolution of the system is described by the Markov equation,

$$\boldsymbol{p}(t_n) = \boldsymbol{p}(t_{n-1})A. \tag{6.4}$$

This equation is the discrete-time analog of the classical master equation (also known as the continuous-time Markov equation) commonly used to describe the dynamics of mesoscopic systems, which will be discussed in §6.2.3.

The sequence of states $\boldsymbol{x} = x_1, x_2, \ldots x_N$ is unknown. At each time step t_n, the system produces a random output or observation, y_n, which is conditionally dependent only on the current state of the system x_n (not on any previous state or observation). In our models we assume that the signal amplitude is proportional to the number of electrons on the quantum dot, plus Gaussian white noise. Mathematically, that means if the system is in state X_i the conductance through the charge sensor y_n is a Gaussian variable with mean value μ_i, which is a function of the number of electrons in state X_i, and standard deviation σ_i:

$$p(y_t = y | x_t = X_i) = \frac{1}{\sqrt{2\pi}\sigma_i} \exp\left[-\frac{(y-\mu_i)^2}{2\sigma_i^2}\right]. \tag{6.5}$$

Together, equations (6.4) and (6.5) constitute a HMM. The model is fully specified by the set of parameters $\boldsymbol{\phi} = \{A, \mu_1, \mu_2, \ldots \mu_M, \sigma_1, \sigma_2, \ldots \sigma_M\}$. The parameters can be constrained as appropriate, for example if state i and state j have the same number of electrons we make the constraint $\mu_i = \mu_j$. In practice we always assume the noise amplitudes are equal for each state, $\sigma_1 = \sigma_2 = \ldots = \sigma_M$.

6.2.3 Continuous time HMM

The discrete-time HMM described above is the most common type of hidden Markov model, on which most of the literature focuses. It is the first type of model we applied to the

RTS analysis problem (see [HZJ09] and §6.5). It is also possible to define a continuous-time HMM, which is based on the continuous-time Markov equation

$$\frac{d}{dt}\boldsymbol{p} = \boldsymbol{p}Q. \tag{6.6}$$

The continuous time representation is more natural since the system itself is continuous in time, only our measurements are discrete. It is possible to convert between the discrete time transition matrix A and the continuous time transition matrix Q since they are related by $A = exp(Q\Delta t)$. In our paper [HZJ09], we said the way to determine the continuous-time transition rates from the discrete time transition matrix A was simply to divide each element of A by Δt. But this is only valid for transition rates small compared to Δt^{-1}. A better way is to take the matrix logarithm of A, $Q = \log(A)/\Delta t$. Taking this matrix logarithm can be problematic, since it does not not have a unique solution, and the taking the principal matrix logarithm may not necessarily give a valid Markov transition matrix [IRW01, RE08]. Using a continuous time Markov model is a better solution.

Roberts and Ephraim developed an algorithm analogous to the Baum-Welch algorithm for estimating the parameters of a continuous time Markov model with Gaussian distributed observations, which they named the Markov-modulated Gaussian Process (MMGP), which is exactly the form of model we wish to apply to our data sets [RE08]. The state of the system is described by the continuous-time Markov equation (Eq. 6.6) and each data point y_n is Gaussian distributed, with mean and standard deviation determined by the state of the system at time t_n, as in the discrete time case we discussed above.

Discrete time models are still adequate for most cases, but given the success of the Roberts-Ephraim algorithm and the more natural representation of the system as a continuous time process, we now prefer to use continuous time models. The analysis in §6.5 still is discussed in terms of discrete-time model because that is how it was originally analyzed. Re-analyzing using a continuous time model would not change the results significantly.

6.2.4 HMMs for two RTS models

We may now discuss how to construct HMMs for the two cases discussed in §6.1 and illustrated in Fig. 6.1. We use notation which is suggestive of the physics of these systems, discussing transitions as *IN* or *OUT*, and labeling states ↑ and ↓, but it is important to note that the HMM is just a mathematical model. Only the number of states, their statistical relationship to the observations, and the values of the model parameters are relevant. It is up to us to provide a physical interpretation to the models.

6.2.4.1 Two-state model

The two-state model is the simplest possible model that can explain an RTS. It has one state each for the 0 electron occupation, $|0\rangle$, and for the 1 electron occupation, $|1\rangle$. Whichever number of electrons is on the dot, there are no excited states, only a ground state. If the states are ordered $(|1\rangle, |0\rangle)$, then the transition matrix Q_2 which describes the model is,

$$Q_2 = \begin{pmatrix} -\Gamma_{OUT} & \Gamma_{OUT} \\ \Gamma_{IN} & -\Gamma_{IN} \end{pmatrix} \tag{6.7}$$

where Γ_{IN} is the rate at which electrons tunnel into the dot, making the transition $|0\rangle \rightarrow |1\rangle$, and Γ_{OUT} is the rate at which electrons tunnel out of the dot, making the transition $|1\rangle \rightarrow |0\rangle$.

For the signal part of the HMM, there are two conductance levels, μ_0 and μ_1, corresponding to the 0-electron and 1-electron states, respectively. There is one noise amplitude parameter, σ. Thus there are a total of five free parameters in the two-state HMM: Γ_{IN}, Γ_{OUT}, μ_0, μ_1, and σ.

6.2.4.2 Three-state model

The three-state model we use has one 0-electron state, $|0\rangle$, and two states which each have 1-electron. For ease of notation we will designate the two 1-electron states $|\uparrow\rangle$ and $|\downarrow\rangle$, which suggests that they are two different spin states, but all that we need is for there to be two

states with distinct transition rates. The transition matrix for the three state model is

$$Q_3 = \begin{pmatrix} -\Gamma^{\downarrow}_{OUT} - W_{\downarrow\uparrow} & W_{\downarrow\uparrow} & \Gamma^{\downarrow}_{OUT} \\ W_{\uparrow\downarrow} & -W_{\uparrow\downarrow} - \Gamma^{\uparrow}_{OUT} & \Gamma^{\uparrow}_{OUT} \\ \Gamma^{\downarrow}_{IN} & \Gamma^{\uparrow}_{IN} & -\Gamma^{\downarrow}_{IN} - \Gamma^{\uparrow}_{IN} \end{pmatrix}. \tag{6.8}$$

where $\Gamma^{\downarrow}_{OUT}$ and $\Gamma^{\downarrow}_{IN}$ are the transition rates for an electron to tunnel out of and into the quantum dot in state $|\downarrow\rangle$, $\Gamma^{\uparrow}_{OUT}$ and $\Gamma^{\uparrow}_{IN}$ are the transition rates for an electron to tunnel out of and into the quantum dot in state $|\uparrow\rangle$, $W_{\downarrow\uparrow}$ is the transition rate from $|\downarrow\rangle$ to $|\uparrow\rangle$, and $W_{\uparrow\downarrow}$ is the rate for $|\uparrow\rangle$ to $|\downarrow\rangle$ transitions.

For the signal part of the HMM, there are two conductance levels: μ_0 corresponds to the 0-electron state $|0\rangle$ and μ_1 corresponds to the 1-electron states $|\uparrow\rangle$ and $|\downarrow\rangle$. There is one parameter for the noise amplitude, σ. So there are a total of nine free parameters in the three-state model: six transition rates $\Gamma^{\downarrow}_{OUT}$, $\Gamma^{\downarrow}_{IN}$, $\Gamma^{\uparrow}_{OUT}$, $\Gamma^{\uparrow}_{IN}$, $W_{\downarrow\uparrow}$, and $W_{\uparrow\downarrow}$; and three signal parameters μ_0, μ_1, and σ.

6.2.5 Likelihood function

From Eq. (6.4) and Eq. (6.5) we can compute the likelihood $p(\boldsymbol{y}|\boldsymbol{\phi})$ of obtaining the sequence of observations $\boldsymbol{y}$ given a set of model parameters $\boldsymbol{\phi}$, which is useful for judging how well a model with parameters $\boldsymbol{\phi}$ fits the observed data $\boldsymbol{y}$. For practical details of computing the likelihood function, see Rabiner [Rab89]. Given a model $\boldsymbol{\phi}$ and a sequence of observations $\boldsymbol{y}$, we can determine the most likely sequence of states the system was in at each time step using the Viterbi algorithm [Vit67, Rab89]. That is, given $\boldsymbol{y}$ and $\boldsymbol{\phi}$, we can find the sequence of states $\boldsymbol{x}$ which maximizes the likelihood $p(\boldsymbol{y}|\boldsymbol{x}, \boldsymbol{\phi})$.

More interestingly, for a given data set $\boldsymbol{y}$ we can find the maximum likelihood estimator $\hat{\boldsymbol{\phi}}$. That is the set of model parameters which best fit the data, in the sense of maximizing the likelihood function $p(\boldsymbol{y}|\hat{\boldsymbol{\phi}}) = \max[p(\boldsymbol{y}|\boldsymbol{\phi})]$. To do this we use the Baum-Welch algorithm for discrete time models and the Roberts-Ephraim algorithm for continuous time models. They are local search algorithms: each iteration takes as input a set of observations $\boldsymbol{y}$ and a set of

model parameters $\boldsymbol{\phi}$, and computes a set of model parameters $\boldsymbol{\phi'}$ such that $p(\boldsymbol{y}|\boldsymbol{\phi'}) \geq p(\boldsymbol{y}|\boldsymbol{\phi})$. Thus, beginning with an initial guess for $\boldsymbol{\phi}$, repeated iterations of the algorithm converge to a maximum in the likelihood function. Finding the true maximum-likelihood estimator $\hat{\boldsymbol{\phi}}$ of the model parameters depends on having a initial guess for the model parameters which leads to the global maximum and not to a suboptimal local maximum. To obtain the initial guesses for signal means and standard deviations, we form a histogram of all the conductance data points and fit them to a mixture of Gaussian functions. The initial guess for the transition matrix is chosen arbitrarily. The maximum-likelihood estimator $\hat{\boldsymbol{\phi}}$ has been shown to have advantageous statistical properties such as strong consistency [Ler92] and asymptotic normality [BRR98] for the type of model described here.

6.2.6 Model selection

6.2.6.1 Model selection background

In any given RTS the observed signal fluctuates back and for between two distinct signal levels, but it is not clear *a priori* that the quantum dot which produces the RTS has only two possible states. It may be that more than one quantum state with the same number of electrons has a chemical potential level within the thermal broadening of the lead, and electrons can tunnel into any of these states. If we know the number of states participating in the observed fluctuations, it is straightforward to construct a HMM with that number of states. But unless we can apply some outside knowledge about the physics of the system we are studying, the number of states is unknown. We can always fit a model with multiple states to the data, and in fact expect that it will fit the data better than a simple model, since it will have more degrees of freedom in the fit. But we should ask whether such a model really fits the data significantly better than a simple model. In HMM literature, determining the number of states in the underlying system is referred to as *estimating the order* of the model.

Fitting a HMM to a data set is a maximum-likelihood fit, and in doing so we calculate

the maximum likelihood value of the model, fit to the data. When we want to compare the goodness of fit of different models, it is natural to use statistical tools based on the maximum likelihood value, such as the likelihood ratio test or penalized maximum likelihood statistics. The likelihood ratio test is a direct hypothesis test, but in our application its usefulness is limited. Comparing penalized maximum likelihood statistics between different models, while not as formally appealing as applying a direct statistical test, can be applied more generally and does prove to be useful in detecting hidden states.

6.2.6.2 Likelihood ratio test

Consider the problem of comparing the results of fitting two different HMMs to a particular data set $\boldsymbol{y}$. Let one model's parameter $\boldsymbol{\phi}$ belong to the parameter set Φ, and a second model have parameter set Φ_0. The second model is nested in the first if $\Phi_0 \subset \Phi$. If this is the case then one way to select between the two models would be to fit both to the data and compare them with the likelihood ratio statistic [Jam06]. The likelihood ratio statistic Λ is defined as

$$\Lambda(\boldsymbol{y}) = \frac{\max_{\boldsymbol{\phi}\in\Phi_0} p(\boldsymbol{y}|\boldsymbol{\phi})}{\max_{\boldsymbol{\phi}\in\Phi} p(\boldsymbol{y}|\boldsymbol{\phi})}. \tag{6.9}$$

Then the test statistic $-2\log(\Lambda)$ is approximately χ^2 distributed with degrees of freedom equal to the difference in dimensionality between Φ_0 and Φ. The two models can be fit to the data, their maximum likelihoods determined, and the value of Λ computed from the ratio of the two. An ordinary χ^2 statistical test can then be applied to determine if the null hypothesis (the simpler model, Φ_0) is adequate to explain the data or if it should be rejected in favor of the larger model (Φ).

The likelihood ratio test can be used to make statistical tests comparing different forms of HMM in many cases. For example, it can be used to test if two transition rates are equal, or if the signal parameters (μ, σ) have an unusual dependence on the underlying states [GRV00]. But unfortunately is not appropriate for comparing two models with different numbers of states [GRV00]. Although a model with R states is indeed nested in a model with $R+1$

states, there are nuisance variables in the nested model that prevent the test statistic from obeying the χ^2 distribution in all cases. We cannot reliably apply the likelihood ratio test to the problem of identifying the number of states in the underlying process.

6.2.6.3 Penalized maximum likelihood statistics

Since we cannot justify applying the likelihood ratio test directly to the problem of determining the number of states, we can consider using penalized maximum likelihood statistics as an alternative. Two such statistics are known as the Akaike Information Criterion (AIC) and Bayesian Information Criterion (BIC) [KR95]. Both of these statistics have been used for estimating the order of a HMM [WP99a, WP99b]. The AIC is defined as

$$AIC = -2\log[p(\boldsymbol{y}|\hat{\phi})] + 2K \tag{6.10}$$

where $p(\boldsymbol{y}|\hat{\phi})$ is the maximum likelihood value and K is the number of free parameters in the model. The BIC is defined as

$$BIC = -2\log[p(\boldsymbol{y}|\hat{\phi})] + K\log(N) \tag{6.11}$$

where N is the total number of data points. In both cases we select the model with the minimum value of the criterion statistic. The maximum likelihood value is used, but it is "penalized" by adding a quantity proportional to the number of degrees of freedom in the model.

Both AIC and BIC have theoretical justification, and there is much discussion in statistical literature about their relative merits. We do not see a clear reason to prefer either one for our application. One HMM study suggested that the BIC is more reliable than the AIC [WP99a, WP99b]. The BIC is more likely to select the simpler model (without an extra state) than the AIC. Ryden proved that a class of penalized likelihood statistics, including both the AIC and BIC, have the valuable property that they do not overestimate the number of states in the model [Ryd95, Eph02]. MacKay developed a similar penalized likelihood statistic for HMM selection [Mac02]. Since we are trying to demonstrate clearly the ability

to detect a hidden state, we have decided to focus on the statistic which is *less* likely to give such a detection, the BIC.

Our strategy for detecting "hidden" states in RTS data is to fit two models to each data set (*i. e.* the two-state and three-state models described in §6.2.4) and to compute the BIC for each model based on the maximized likelihood value found in the fit and the number of free parameters in each model. The model with the lower value of BIC is selected. So far we have used only the BIC as selection criteria, but the AIC and other model selection criteria could be applied. We have not investigated exactly how the performance of different selection criteria compare. There is reason to believe our model selection strategy could be improved upon in future work.

6.2.7 Confidence intervals for HMM-estimated parameters

Using maximum likelihood estimates we can also construct likelihood ratio confidence intervals for the estimated parameters. As discussed above, the likelihood ratio statistic obeys the χ^2 distribution when two models, one nested in the other, are compared.

For example, after finding the maximum likelihood estimate of the transition matrix for a particular model we would like to establish a confidence interval for a particular transition rate, say rate Q_{ij}. We change Q_{ij} to some sub-optimal value Q'_{ij}, then re-estimate the HMM with this restriction. The restricted model will have a maximum likelihood value less than the original fit. We compute the likelihood ratio statistic for the two models, and note that the restricted model is nested in the original model with one less degree of freedom, so the likelihood ratio statistic obeys the χ^2 distribution with 1 degree of freedom. If the likelihood ratio statistic is equal to the χ^2 value for the confidence level we wish to test (*e.g.*, for a two-tailed 90% confidence interval, the boundary value is $\chi^2 = 3.84$), then the value Q'_{ij} is on the boundary of the confidence interval.

It is computationally very expensive to estimate these confidence intervals because for

each value of the parameter[1]. In practice, rather than trying to find specific values that are on the boundaries, we choose several (seven, usually) fixed values of the parameter near its optimum value, find the maximum likelihood value with respect to the other parameters at each of those points, then fit the results to a parabola and find the points at which the parabola is equal to the desired χ^2 level. This saves us from having to repeat the maximization procedure very many times, to find the exact boundary. We find that the likelihood function is almost always well behaved, like a parabola near the maximum likelihood point, as it is known to be asymptotically [BRR98], except when the transition rate being estimated is very small.

Uncertainties in the transition rates are usually highly correlated, especially between two states in the same class. When estimating the three-state model parameters $\Gamma_{IN}^{\downarrow}$ and $\Gamma_{IN}^{\uparrow}$ we find that the uncertainties are nearly perfectly anti-correlated. The total transition rate $\Gamma_{IN}^{\downarrow} + \Gamma_{IN}^{\uparrow}$ has small uncertainty, but the two individual rates cannot be determined with precision. This is because the two states $|\downarrow\rangle$ and $|\uparrow\rangle$ can't be distinguished directly, and the rates of transition into these two states simply don't contribute much distinct information to the structure of the signal (the rates of tunneling out of the two states do).

6.3 Example analysis

An example of an RTS data set is shown in Fig. 6.3. This data set was taken from the experiment by Li *et al.*, discussed in detail in §6.6. Only a small piece of the RTS data set is shown; the entire sequence is 8 s long. The signal is proportional to the conductance of a point contact that measures the state of a quantum dot. The signal is switching back and forth between two conductance levels as an electron is either on the quantum dot (low signal level) or not (high level).

We fit the data set using the Baum-Welch algorithm to a two-state model. The model pa-

[1]Calculating intervals for all the transition rates of a single model can take up to several hours on a modern desktop computer

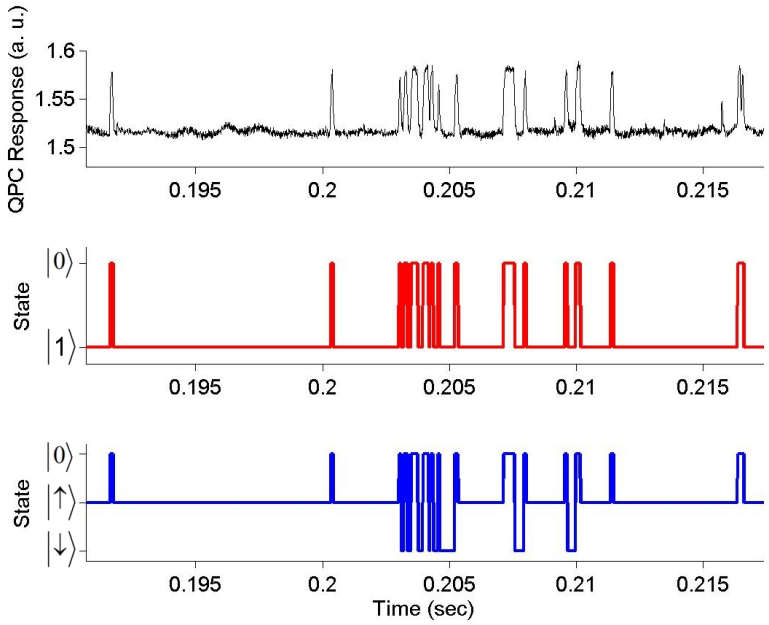

Figure 6.3: (top) Example of an RTS data set. (middle) Viterbi sequence of states found by fitting a two-state model to the data at top. (bottom) Viterbi sequence of states found by fitting a three-state model to the data at top.

rameters that maximize the likelihood function are found to be Γ_{OUT} =537.2 Hz, Γ_{OFF} =8094.9 Hz, μ_0 =1.5695, μ_1 =1.5185, and σ =0.00557. The sequence of states that was reconstructed according to this model, using the Viterbi algorithm, is shown in the middle of Fig. 6.3. This reconstruction faithfully follows the signal, indicating state $|0\rangle$ (no electron) when the signal is high and state $|1\rangle$ (one electron) when the signal is low. These are the most likely states at each point in time, according to the Viterbi criterion.

Next, a three-state model was fit to the data. The maximum likelihood estimates for the parameters found in this case were $\Gamma^{\downarrow}_{OUT}$ = 1334.5 Hz, $\Gamma^{\uparrow}_{OUT}$ = 337.7 Hz, $\Gamma^{\downarrow}_{IN}$ = 3582.8 Hz, $\Gamma^{\uparrow}_{IN}$=4522.7 Hz, $W_{\downarrow\uparrow}$ = 153.3 Hz, $W_{\uparrow\downarrow}$ = 76.3 Hz, μ_0 =1.5695, μ_1 =1.5185, and σ =0.00557. The signal parameters (μ_0, μ_1, and σ) are found to be the same between the two models, as expected. Shown at the bottom of Fig. 6.3 is the Viterbi sequence reconstructed from the data using the three-state model fit. The model predicts state $|0\rangle$ when the signal level is

high and either $|\downarrow\rangle$ or $|\uparrow\rangle$ when the signal level is low. In this example the model indicates that $|\uparrow\rangle$ has a longer lifetime than $|\downarrow\rangle$ (that is, $\Gamma^{\downarrow}_{OUT} > \Gamma^{\uparrow}_{OUT}$), and that is reflected in the Viterbi reconstruction. In those cases where the electron stayed on the dot a relatively long time the model estimates that the system was in state $|\uparrow\rangle$, and in those instances when the electron stays on the quantum dot a relatively short time before tunneling off, $|\downarrow\rangle$ is selected as being more likely. It is the difference in tunnel-out rates between $|\downarrow\rangle$ and $|\uparrow\rangle$ that allows them to be distinguished.

Now we should ask, are we justified in applying the three-state model, or does the two-state model fit well enough to explain the data on its own? A related question is, is the difference in tunneling rates between $|\downarrow\rangle$ and $|\uparrow\rangle$ statistically significant? To address the first question we look to the penalized likelihood criteria AIC and BIC. For the two-state model the logarithm of the maximum likelihood value was found to be 3718581.0. The model has 5 free parameters and the number of data points was 995328, so $AIC = -2(3718581.0) + 2(5) = -7437151.9$ and $BIC = -2(3718581.0) + 5\log(995328) = -7437092.9$. For the three-state model fit, the log of the maximum likelihood was 3718666.3. The model has 9 free parameters, so we have $AIC = -2(3718666.3) + 2(9) = -7437313 = 4.6$ and $BIC = -2(3718666.3) + 9\log(995328) = -7437208.3$. We see that both the AIC and BIC are lower for the three-state model than for the two-state model, so the three-state model is preferred according to both of these selection criteria[2].

6.4 Application to simulated data

In support of the analysis for the Zhang experiment detailed in §6.5, we produced a series of Monte Carlo simulations of RTS data with similar characteristics to the data in the Zhang experiment. For each simulation a set of transition rates and an initial state were chosen, and for each subsequent timestep the state of the quantum dot was chosen randomly, based on the prior state and the probabilities in the transition matrix. Then the RTS signal was

[2]For the purposes of an example I deliberately chose to show one where the three-state model was selected.

generated by taking the signal value that corresponds to the chosen state at each timestep and adding Gaussian white noise. The simulation parameters were chosen to mimic the type of data we have in the Zhang experiment: 200,000 data points were simulated, with a sampling rate of 4096 Hz. For each RTS simulated, the transition rates were chosen randomly so that the probability of transition at each timestep was between 0 and 0.3, which corresponds to transition rates between 0 and 1223 Hz.

6.4.1 Various noise levels simulated

Robustness against noise is a major advantage of the HMM approach relative to previous analysis techniques. To deal with noise, most studies apply a threshold to digitize the data before analysis, or apply a change-detection procedure to the signal to determine when it transitioned from one conductance level to the next [LJP03]. In another approach, Yuzhelevski, *et. al.* [YYJ00] proposed a method for estimating transition rates that is substantially similar to the one presented here, except their method is less general and their algorithm assigns a definite state to the system at each data point. *HMMs determine transition rates more accurately in the presence of noise because they do not assign a definite state to the system at each timestep.* Instead, for each data point the model predicts a finite probability of the system being in each state. This is more flexible than a fixed assignment of the signal state. The final transition rate estimates are weighted averages over every available data point, instead of being unweighted averages over a relatively smaller number of transition events. When the system is assigned a specific state at each data point, even a relatively small number of missed assignments of the state can lead to large errors in estimating transition rates.

To illustrate how errors in removing noise can bias estimates of the transition rates, we made Monte Carlo simulations of a Markov process and compared the HMM estimates of the transition rates to two other estimation techniques, the results of which are shown in Fig. 6.4. Each simulation is of a two-state Markov process, with randomly chosen transition rate Γ_{IN} and Γ_{OUT} for each simulation. The transition probabilities were then estimated from

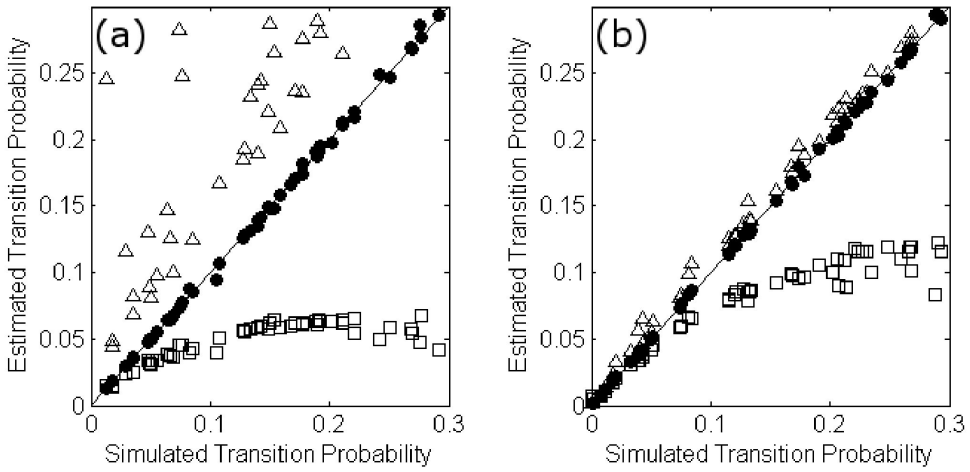

Figure 6.4: Results of applying various data analysis techniques to 100 simulated RTS. The transition rates estimated by three different analysis techniques are plotted against the true transition rate that was used in the simulation. The estimation techniques are HMM (closed circles), digitization by a change-detection algorithm [LJP03] (open squares), and digitization by a threshold determined from a two-Gaussian fit to the data (open triangles). The signal-to-noise ratio is: (a) SNR=3. (b) SNR=5.

the simulated data using three different approaches: fitting to a HMM, digitization by a change-detection algorithm[LJP03], and digitization by a threshold determined from a two-Gaussian fit to the data. The transition rate estimated by each method is plotted against the true transition rate used in the simulation. The change-detection method underestimates transition rates because it tends to fail to detect brief transition events. The threshold method tends to overestimate transition rates because it counts spurious transitions. The HMM approach can estimate transition rates with a signal-to-noise ratio as low as 3, and could do better if longer data sets were used.

6.4.2 Hidden state detection

Another Monte Carlo simulation study evaluated how much difference there needs to be between transition rates before a hidden state could be detected. Two groups of 100 RTS data sets were simulated, one group being a simulation of a two-state system and the other a three-state system (containing one hidden state). For each simulation the transition rates were chosen randomly, as previously discussed. Two discrete-time HMMs were then fit to each simulated data set, a two-state model and a three-state model. The BIC of these two fits was then compared, with the model having the lower BIC value being preferred.

For the 100 data sets which simulated a two-state system, the two state model was *always* chosen. In no case were there errors of model selection where the three-state model was preferred. This is consistent with Ryden's theorem which states that (asymptotically) HMM model selection by BIC will never overestimate the number of states in the system [Ryd95].

For the 100 data sets which simulated a three-state system, the three-state model was correctly selected in many cases. Those cases in which it was not chosen were almost all cases in which the two transition rates for electrons to tunnel *out* of the quantum dot were very similar. This is illustrated in Fig. 6.5. Each data point on the plot represents the result of one simulation. An open red circle is used in those cases where the three-state model was correctly selected, closed blue circles indicate where the two-state model was selected. The x-axis is the ratio of the two transition rates for an electron to transition *out* of the 1-electron states, and the y-axis is the ratio of the two transition rates for tunneling *in* to each of the 1-electron states. The plot shows that the correct assignment was made with a high degree of certainty, provided that the two transition rates *out* of the 1-electron states were different enough. In these simulations, if the two OUT transition rates were different by about a factor of 2 or more, the extra state could be detected with a high degree of certainty. When those two rates were too similar, the hidden state was not detected. The ability to detect the hidden state did not depend significantly on the IN rates.

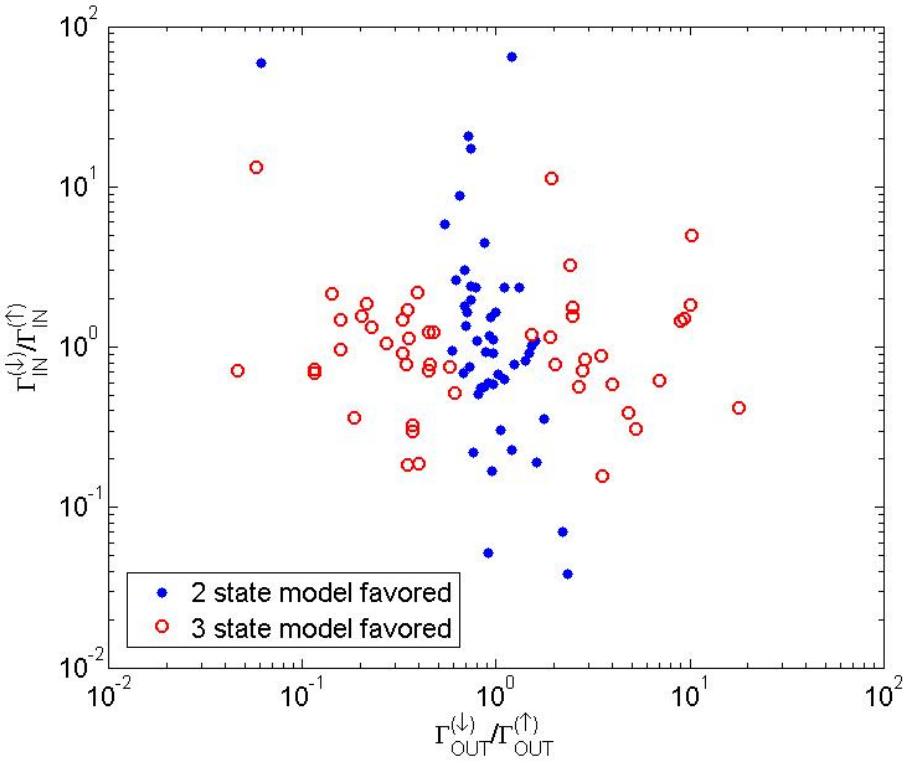

Figure 6.5: Results of fitting two HMMs to simulated data and comparing their BIC to see if the three-state model could be correctly selected. Points are plotted against the ratio of two transition rates in the simulation, as described in the text.

6.5 Zhang, *et al.* experiment

6.5.1 Experiment description

One data set to which we have applied discrete HMM analysis was taken from an experiment performed by Zhang, *et al.*, in our lab [ZMB09]. In this experiment a lateral quantum dot was defined by depletion gates in a two-dimensional electron gas in a GaAs/AlGaAs heterostructure, shown in Fig. 6.6. The dot was coupled to a single lead by a tunnel barrier between gates T and M to a 2DEG reservoir of electrons at the left side of the figure. The Fermi level of the lead was tuned so that one electron remains fixed on the dot while a second

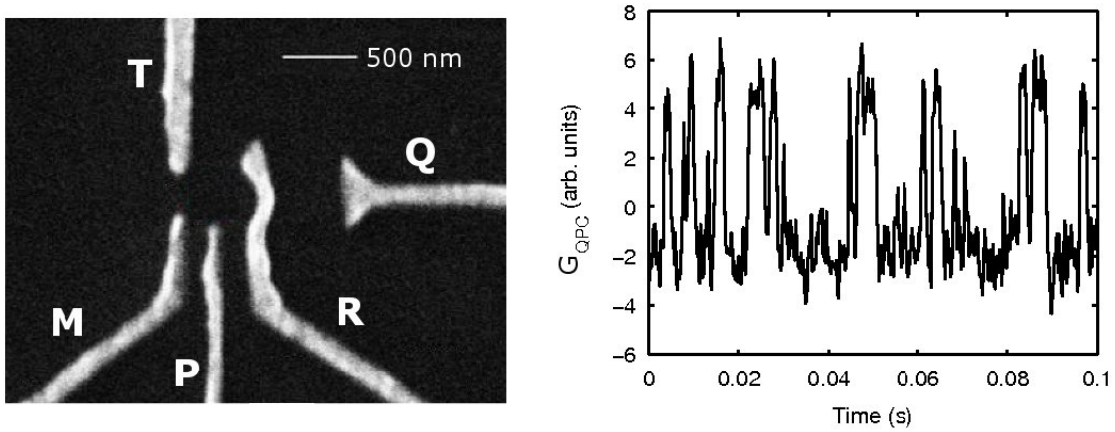

Figure 6.6: (left) SEM image of the quantum dot structure used in the Zhang experiment. Negative voltages on the metal gates deplete the 2DEG (dark areas, below the gates), forming a quantum dot in the center of gates M, P, R and T. A tunnel barrier is formed between gates M and T so that electrons can tunnel to/from the lead (dark area to the left). A QPC is formed between gates R and Q; the current passing between them is sensitive to the presence of electrons on the dot. (right) Example of charge sensor data set from the Zhang experiment. The QPC conductance alternates between two distinct levels as electrons enter and leave the quantum dot. In this case the upper level corresponds to $N = 1$ electron on the quantum dot and the lower level corresponds to $N = 2$.

electron may tunnel to and from the dot ($N = 1 \leftrightarrow N = 2$ transition). The transitions are observed by measuring the current through a nearby QPC, between gates Q and R. An example of such a data set is shown in Fig. 6.6. The chemical potential of the quantum dot states can be changed relative to the Fermi level of the reservoir by changing the voltage V_P on the plunger gate, P.

6.5.2 HMM analysis

Assuming the quantum dot transitions between just two states, state 1 having $N = 1$ electrons and state 2 having $N = 2$, the discrete time transition matrix of the system is of

the form

$$A = \begin{pmatrix} 1 - p_{OUT} & p_{OUT} \\ p_{IN} & 1 - p_{IN} \end{pmatrix} \tag{6.12}$$

where p_{IN} and p_{OUT} are the probability of an electron tunneling onto and off of the dot, respectively, at each timestep. For each value of V_P, 50 seconds of RTS data were taken at a sampling rate of 4096 Hz ($\Delta t = 0.244$ ms) and the Baum-Welch algorithm was used to estimate the transition matrix. The transition rates $\Gamma_{ON/OFF}$ can be determined from the transition matrix by taking the matrix logarithm of A, as discussed in §6.2.3.

The transition rates extracted by fitting the two-state model to the data are shown in Fig. 6.7. These transition rates were determined by fitting the QPC data to the purely mathematical HMM; next we fit them to a physical model. Electrons tunnel to and from the lead at a rate Γ_0 multiplied by the fraction of occupied (unoccupied) states in the lead for transitions on (off) the dot,

$$\Gamma_{ON/OFF} = \Gamma_0 f\left(\frac{\pm(\Delta\mu - \alpha e V_P)}{k_B T}\right), \tag{6.13}$$

where $\Delta\mu = E_f - \mu_D$ is the difference between the Fermi level E_f of the lead and the chemical potential of the dot μ_D at $V_P = 0$, and α is the relative capacitance between the dot and gate P, which was determined from Coulomb diamond measurements to be $\alpha = 0.011$ for this device. The electron temperature was $T = 0.5$ K. f is the Fermi distribution, which represents the occupation of electron states in the lead. The results of fitting the transition rates to this model are shown in Fig. 6.7. The transition rates fit the thermal reservoir model well except for the tail of the Γ_{OFF} rates, which do not go to zero as expected but level off at about 15-20 Hz. It appears that there is an unexpected slow process by which electrons leave the quantum dot that is independent of V_P. This process has been identified with inelastic back-action of the QPC charge sensor acting on the electron on the quantum dot [LXC12, LXC11]. It is worth pointing out that HMM analysis clearly revealed this very small effect, while the original statistical analysis done for this experiment did not.

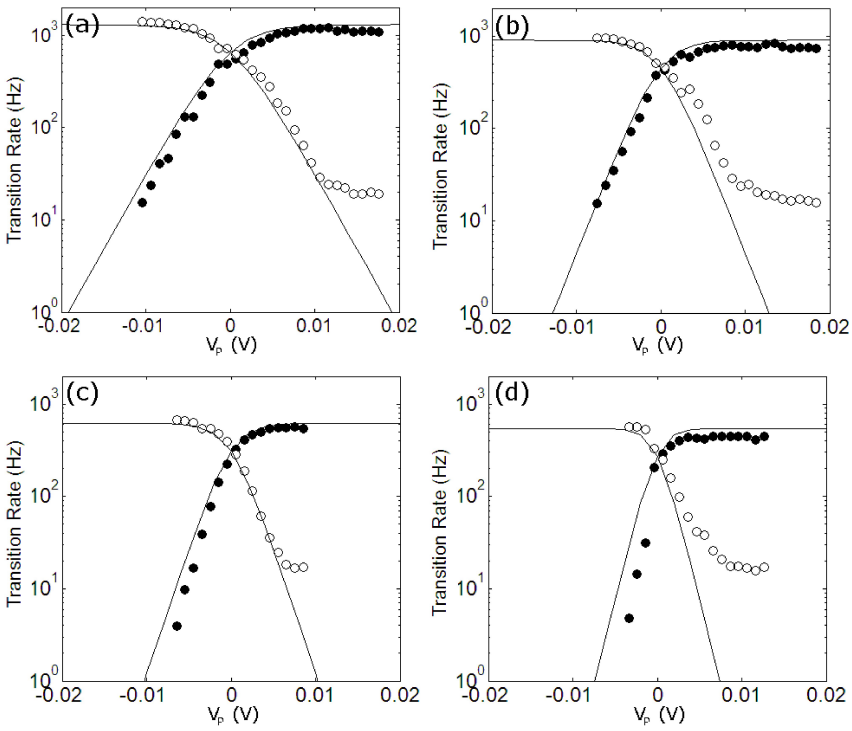

Figure 6.7: Electron transition rates Γ_{ON} (closed circles) and Γ_{OFF} (open circles) determined from HMM analysis. The voltage V_P is varied in each plot, which changes the chemical potential for the electron to tunnel onto the dot relative to the Fermi level of the lead. Four different values of the voltage on gate M are shown: (a) $V_M = -775$ meV. (b) $V_M = -800$ meV.(c) $V_M = -825$ meV. (d) $V_M = -850$ meV. Lowering the voltage on gate M raises the tunnel barrier to the lead and lowers the tunnel rate. Solid lines show fits to a Fermi distribution as described in the text.

6.5.3 Tests for additional states

As discussed in §6.2.6, if the transition rates of these states are significantly different from one another, HMM analysis should be able to detect the additional state. For the data sets presented here we applied different HMMs: one model containing an extra 1-electron state, one model containing an extra 2-electron state, and a four-state model that had an extra state for both 1-electron and 2-electron configurations. Each different model was fit to the data sets, and the BIC of the resulting fit calculated. In all cases the BIC of the simple

two-state model was smallest. We conclude that in this experiment there is not sufficient evidence in the data to justify a model with more than two states. Here we had a simple situation without additional quantum states.

6.6 Li, *et al.* experiment

6.6.1 Experiment description

Another experiment to which we have applied HMM analysis was performed by Hai Ou Li, Ming Xiao, and their colleagues at the University of Science and Technology of China [LXC12, LXC11, CXL11]. These collaborators conducted a series of experiments on GaAs quantum dots in which they collected a large number of RTS data sets and used them to study what appears to be an inelastic back-action effect the QPC imparts on the quantum dot [LXC12], an effect which was actually first seen when we analyzed the Zhang, *et al.*, experiment, as mentioned in §6.5 and in [HZJ09]. At that time we did not understand the effect well enough to assign a physical mechanism to it, but the USTC experiments have shed some light on it.

For HMM analysis of these RTS data sets, we chose to focus on the $0 \leftrightarrow 1$ electron transition because it should have physics which is easiest to understand. The 0 electron charge state should not have any "excited" states and should stand alone, while the 1 electron state should at least have one "hidden" state because the electron can be either spin-up or spin-down. At zero magnetic field the two spin states are degenerate, but by applying a magnetic field the two spin states are split in energy by the Zeeman effect and exhibit distinct dynamics. We use HMM analysis to observe the effect of the "hidden" spin state on the RTS statistics, and to determine the dynamics of the two spins independently.

In this experiment a QD with a nearby QPC was fabricated in a GaAs/AlGaAs heterostructure. The quantum well was 95 nm below the surface, having an electron density of 3.2×10^{11} cm^{-2} and a mobility of 1.5×10^{5} cm^2 V^{-1} s^{-1}. Fig. 6.8 shows an SEM image of

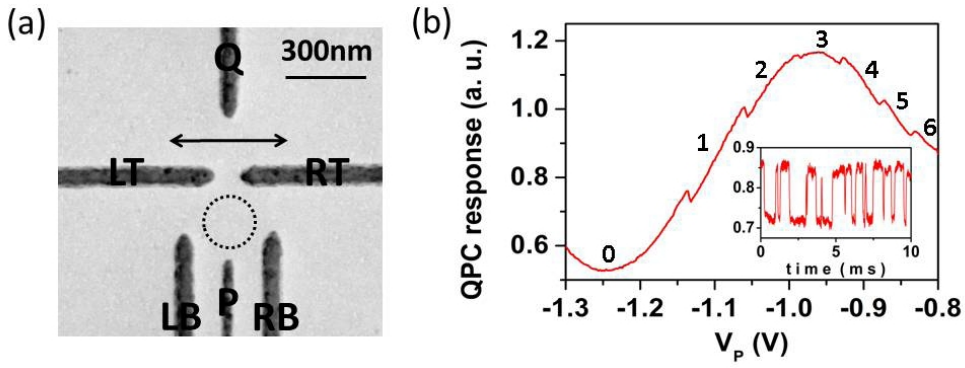

Figure 6.8: (left) SEM image of the device used in the Li experiment. A quantum dot is formed in the circled region. Above the quantum dot, a QPC channel is formed between gates Q, LT, and RT. (right) Example trace of the QPC conductance as a function of gate voltage V_P, which shows a broad oscillation which is the QPC response to the gate voltage, with small kinks that are cause by electron transitions to/from the quantum dot. The inset shows an example of a RTS data set.

the surface gates. The quantum dot is defined in the area circled in the image by the five gates LT, RT, LB, RB, and P. Gates Q, LT, and RT form a QPC channel for sensing the charges on the quantum dot. A small gap between LT and RT was created to maximize the sensitivity of the QPC to charges on the quantum dot (but V_{LT} and V_{RT} were tuned so there was no tunneling of electrons through this gap). The experiment was performed in a ^{3}He refrigerator operating at a base temperature of 240 mK.

In these experiments the quantum dot was tuned so that the tunnel barrier between LB and LT was completely closed, and the barrier between RB and RT was open enough that electrons were allowed to tunnel back and forth between the quantum dot and the reservoir to the bottom right of the image. Fig. 6.8 shows a trace of the QPC conductance as a function of the voltage on gate P. Each small "bump" in the curve corresponds to a single electron transition onto (off of) the dot as the voltage is raised (lowered). The last electron is seen to leave the dot near V_P =-1.15 V. The dot was tuned close to this 0 electron $\leftrightarrow$ 1 electron transition point, and the voltage on gate RB was adjusted so that the tunneling rate between the quantum dot and the lead was smaller than the bandwidth of the measurement

channel, 30 kHz. A Coulomb diamond plot was taken to measure the capacitive coupling strength of gate P acting on the quantum dot, which was found to be $\alpha = 0.022$ eV / V. The lever arm α was used to determine the absolute electrochemical potential scale of the quantum dot relative to changes in V_P.

To generate RTS data sets, V_P was tuned so that the chemical potential of the dot was close to the Fermi level of the lead for the 0↔1 electron transition so that one electron would tunnel on and off the dot and form an RTS. The real-time data was sampled at 131.1 kHz and collected for 7.6 seconds, for a total of 995328 data points in each RTS data set. After each RTS data set was taken, the voltage V_P was stepped to change the detuning of the quantum dot's chemical potential relative to the Fermi level of the reservoir, and another RTS data set was taken. Each RTS was then fit to two HMMs, the two-state and three-state models described above.

6.6.2 Tunnel rate physics

We understand the tunneling rates in this experiment using the following model:

$$\Gamma_{IN}^{\downarrow} = \quad \overline{\Gamma^{\downarrow}} e^{-\beta(\mu - E_f - \Delta_Z)} f\left(\mu - E_f - \Delta_Z\right) \tag{6.14}$$

$$\Gamma_{IN}^{\uparrow} = \quad \overline{\Gamma^{\uparrow}} e^{-\beta(\mu - E_f + \Delta_Z)} f\left(\mu - E_f + \Delta_Z\right) \tag{6.15}$$

$$\Gamma_{OUT}^{\downarrow} = \overline{\Gamma^{\downarrow}} e^{-\beta(\mu - E_f - \Delta_Z)} \left[1 - f\left(\mu - E_f - \Delta_Z\right)\right] \tag{6.16}$$

$$\Gamma_{OUT}^{\uparrow} = \overline{\Gamma^{\uparrow}} e^{-\beta(\mu - E_f + \Delta_Z)} \left[1 - f\left(\mu - E_f + \Delta_Z\right)\right]. \tag{6.17}$$

Here $\Delta_Z = g\mu_B B/2$ is the Zeeman energy, β is a factor which is due to the energy dependence of the tunneling rate [MAR07]. The rates $\overline{\Gamma^{\downarrow}}$ and $\overline{\Gamma^{\uparrow}}$ we call the gross tunnel rates, which are independent of the detuning $\mu - E_f$. The gross tunnel rates depend on the geometrical details of the tunnel barrier between the quantum dot and the reservoir. Amasha, *et al.* found that there is a spin-dependence of the gross tunnel rate at finite magnetic field, so we allow for there to be two independent gross tunnel rates for the two spins [AMR08b]. The parameter β and the exponential factor in which it appears characterizes the energy dependence of the tunnel rate [MAR07]. The third factor in each equation is the fraction of

states in the lead that are occupied, for tunneling in, or unoccupied for tunneling out rates. In each case the detuning of the quantum dot relative to the Fermi level of the lead, $\mu - E_f$ is modified by the Zeeman energy for each spin state. Since in GaAs $g = -0.44$ is negative, the spin-up state is lower in energy than spin down.

6.6.3 Results at B=0 T

The results of fitting the two types of HMM to one series of RTS is shown in Fig. 6.9. These data were taken at zero magnetic field. The horizontal axis is the detuning, the difference between the chemical potential of the quantum dot μ and the Fermi level of the reservoir, E_f. Subplots (a) and (b) show the results of the two-state model, which estimates the total tunneling rates Γ_{IN} and Γ_{OUT}. As expected, Γ_{IN} is high at negative detuning and goes to zero at positive detunings, while Γ_{OUT} has nearly the opposite behavior. The solid lines show the physical model described by Eq. 6.14, fit to the HMM-estimated data points. We see that there is a good agreement with the expected physics, except for an unexpectedly high Γ_{OUT} at negative detuning. There Γ_{OUT} levels off instead of decaying exponentially as a function of detuning. This effect is connected with inelastic back-action of the QPC on the quantum dot [LXC12].

The three-state model transition rate estimates on the same data sets are shown in Fig 6.9, subplots (c), (d), and (e). There are a total of six transition rates between the three states that are estimated by the model: two rates for the electron to tunnel in to the dot shown in (c), two rates for the electron to tunnel out shown in (d), and two rates for the electron to change from one spin to the other shown in (e).

Fig. 6.9 (f) is shown the difference in the model selection statistics AIC and BIC for the two models. The quantity plotted is the AIC (BIC) for the three-state model subtracted by the AIC (BIC) of the two-state model fit. When this quantity is positive, the two-state model is selected, and when it is negative there is significant reason to select the three-state model instead. In this case we find that at all detunings the BIC is positive, and the AIC is

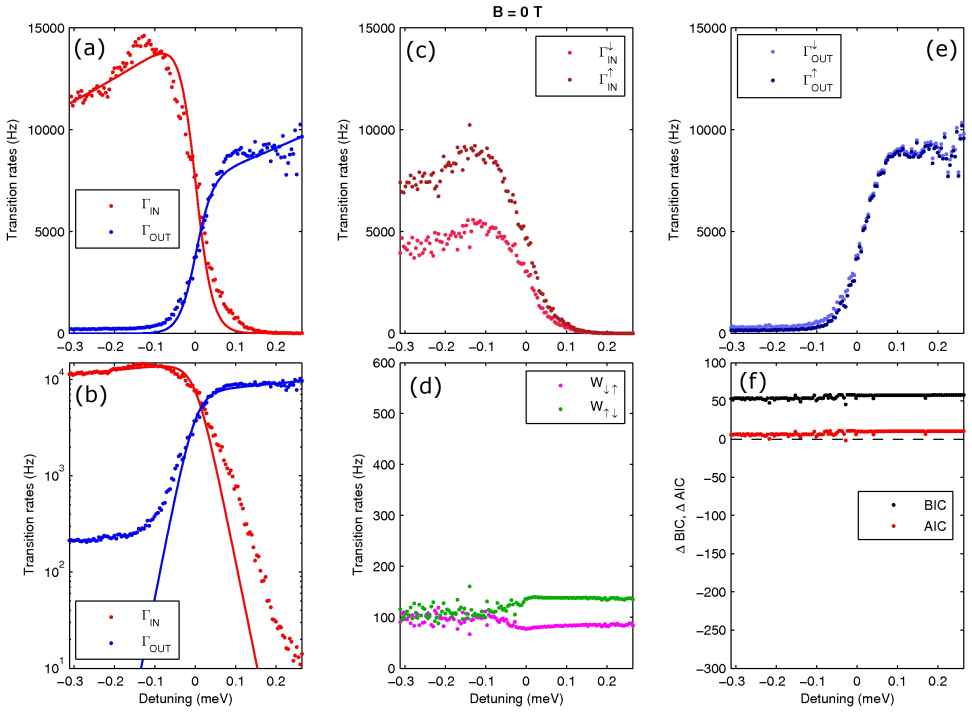

Figure 6.9: HMM transition rate estimates obtained at $B = 0$ T. (a) Results of the two-state model. Solid lines indicate fits to the total tunnel rates as described in the text. (b) Results of the two-state model, same as (a) but on a logarithmic scale to emphasize the back-action effect. (c) Three-state model estimates for the IN tunneling rates for two spins. (d) Three-state model estimates for the spin-flip transition rates $W_{\downarrow\uparrow}$ and $W_{\uparrow\downarrow}$. (e) Three-state model estimates for the OUT tunneling rates for two spins. (f) Differences in the AIC and BIC statistics for the two models.

negative only at one or two points that are probably statistical fluctuations.

These two tunnel-in rates $\Gamma_{IN}^{\downarrow}$ and $\Gamma_{IN}^{\uparrow}$ shown in Fig. 6.9 (c) appear to be different, but since the selection criteria favor the two-state model we can conclude that this difference is not statistically significant. Their sum matches the total tunneling-in rate determined by the two-state model, $\Gamma_{IN} = \Gamma_{IN}^{\downarrow} + \Gamma_{IN}^{\uparrow}$, but the two rates cannot be determined independently. The probability of each spin state after a tunneling-in event is independent of the amount of time it takes for the tunneling event to occur. The tunneling-in rates simply don't contribute much information entropy to the RTS. Most of the information about the two spin states is encoded in the tunneling-out times.

Fig. 6.9 (d) shows the two tunneling-out rates $\Gamma_{OUT}^{\downarrow}$ and $\Gamma_{OUT}^{\uparrow}$ estimated by the three-state model. In this case the two rates are almost identical and equal to the tunnel-out rate found by the two state model, Γ_{OUT}. This is to be expected, since at zero magnetic field the two states are degenerate and should have the same tunneling rate.

Fig. 6.9 (e) shows the rates for transitions between the two spin states, the spin relaxation rate $W_{\downarrow\uparrow}$ and the spin excitation rate $W_{\uparrow\downarrow}$. Since we cannot favor the three-state model over the two-state model they do not have statistical significance.

6.6.4 Spin state detection

At zero magnetic field there is no reason to be able to detect the presence of two distinct spin states in a single RTS, because they are degenerate and have the same tunneling rates. Applying a magnetic field in the plane of the quantum well introduces a Zeeman energy difference between the two spin states, which means each state interacts with a different occupancy of states in the lead and has a different net tunneling rate.

Like Amasha, *et al.*, we found that applying a magnetic field reduced the gross tunneling rates (for both spin states), so at high magnetic field ($\geq$5 T) we adjusted the tunneling barrier by raising the voltage on gate RB to keep the tunneling rate in the kHz regime, high enough to give a good number of electron transitions in the RTS. It is not clear why the

magnetic field influences the gross tunneling rate; it may be due to the sample not being precisely positioned in-plane with the magnetic field.

Figure 6.10 shows HMM fit results for four data series taken at $B = 0$, 1, 2, and 3 T applied magnetic field. For each series the upper plot shows the two tunnel-out transition rates determined by fitting the three-state model, and the model selection statistics in the lower plot, each as a function of the detuning. At $B = 0$ T the two tunneling rates are the same and the AIC and BIC statistics favor the two-state model, so the two spin states cannot be distinguished. But when a finite magnetic field is applied the two spin states have different tunnel rates, and this can be detected. We see that at $B = 1$ T there is a small window in detuning where the two spin states are measured to have distinct tunneling rates, and the AIC and BIC statistics favor the three-state model (the AIC/BIC difference is negative). As the magnetic field is increased the separation in tunnel rates between the two spin states increases and the difference in AIC/BIC statistics becomes larger.

In those cases where the AIC or BIC is less for the three-state model (negative on the plots), we may confidently say that a simple two-state model is insufficient to explain the statistics of the RTS. There must be an additional state present (in this case, a spin state) with a unique tunnel-out rate to sufficiently explain the data. Thus, we have demonstrated that using this approach we can detect the presence of a "hidden" state in a single RTS, provided that there are enough electron transitions observed to build up statistics, and the transition rates *out* of the two states with the same number of electrons are distinct.

In all of these data sets, the spin state can be reliably detected only at negative detuning, roughly in the range $-\Delta_Z < \mu - E_f < 0$. This is because it is at modest negative detunings where there is significant participation in the fluctuation by both spin states. The ground state always has a higher tunnel-in rate, so there are always plenty of electron transitions involving the ground state but not always the excited state. This is especially true at positive detunings, where the net tunnel rate for the ground state is much higher than the excited state. At negative detuning the occupancy of states in the reservoir at the potential level of the excited state is significant, so it also can participate. At far negative detunings, the

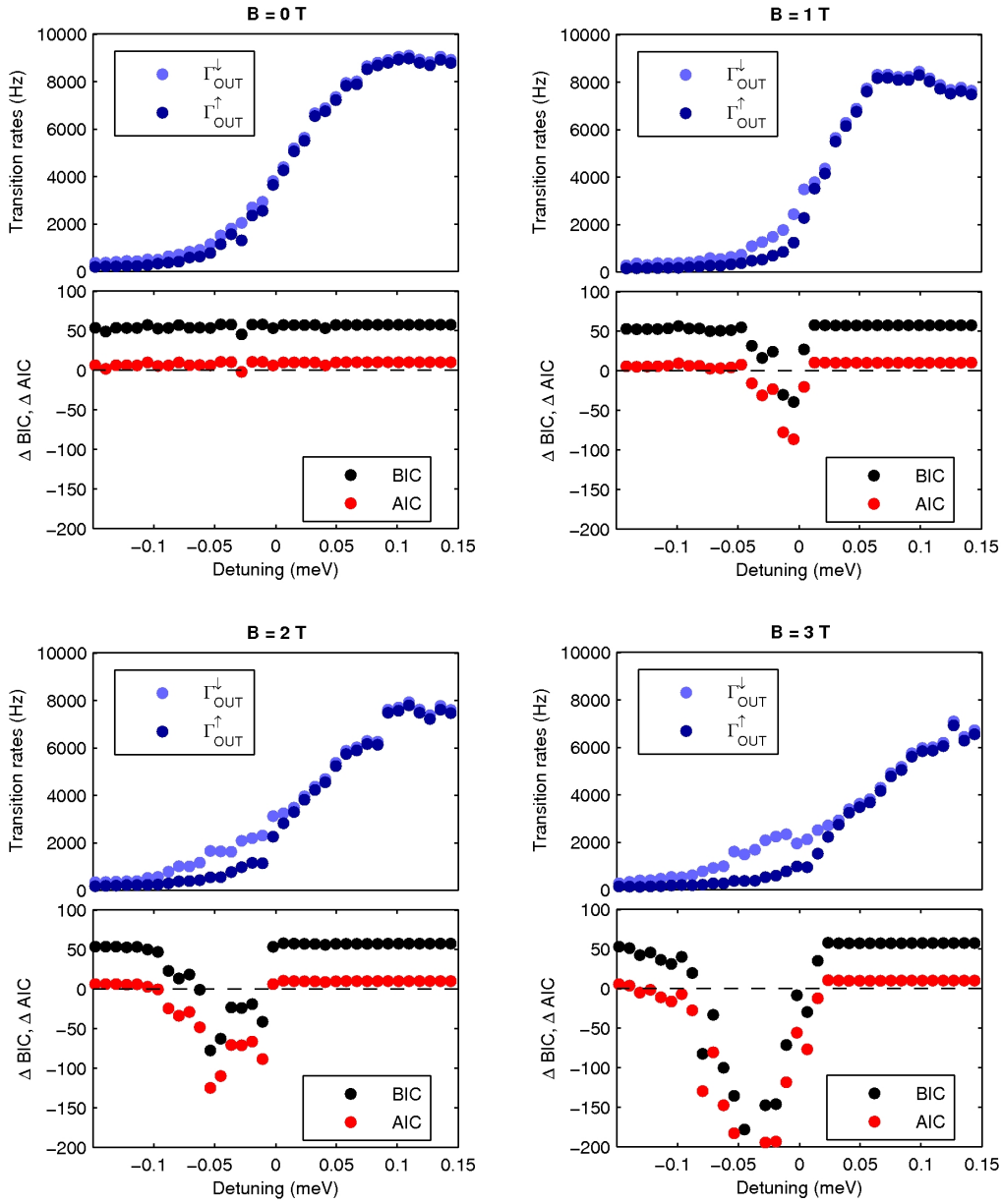

Figure 6.10: Tunnel-out transition rates and model selection statistics for four magnetic fields 0, 1, 2, and 3 T. The upper plots show two tunnel-out rates for the two spin states, as determined by fit to the three-state model. The lower plots show the difference in AIC and BIC statistics between the three-state model and the two-state model.

dot is occupied most of the time and the total number of transitions is less. In principle we could overcome these limitations by acquiring longer RTS data sets.

6.6.5 Spin-dependence of tunnel rates

Amasha, *et al.*, found that a Zeeman energy splitting introduced an unexpected spin-dependence of the gross tunneling rates (in our notation, $\overline{\Gamma^{\downarrow}} \neq \overline{\Gamma^{\uparrow}}$) [AMR08b]. A possible theoretical explanation for this effect is that the electron g factor in the lead may be significantly different than the quantum dot [SJ10], but it is not a well understood phenomenon. We can study it in two ways: first, similar to Amasha, *et al.* we can use measurements of the total tunneling rates Γ_{IN} and Γ_{OUT} as a function of detuning to deduce the gross tunnel rates of the individual spins. Second, we can use a three-state HMM to determine the tunnel-out rates $\Gamma_{OUT}^{\downarrow}$ and $\Gamma_{OUT}^{\uparrow}$ independently for the two spin states.

The total tunnel-in rate Γ_{IN} is simply the sum of the two rates for the two spins,

$$\Gamma_{IN} = \Gamma_{IN}^{\downarrow} + \Gamma_{IN}^{\uparrow}. \tag{6.18}$$

The total observed tunnel-out rate is the average of the two tunnel-out rates for each spin, weighted by the average time the electron spends in each spin state. It can be found in full generality from Eq. 6.27. If $W_{\downarrow\uparrow} = W_{\uparrow\downarrow} = 0$, it simplifies to

$$\Gamma_{OUT} = (\Gamma_{IN}^{\downarrow}\Gamma_{OUT}^{\downarrow} + \Gamma_{IN}^{\uparrow}\Gamma_{OUT}^{\uparrow})/(\Gamma_{IN}^{\downarrow} + \Gamma_{IN}^{\uparrow}). \tag{6.19}$$

These two equations give us a way to relate the total observed tunnel rates with the individual spin rates. Along with Eqs. 6.14, we can state them as a function of the detuning of the quantum dot. Fig. 6.11 shows the total tunnel rates Γ_{IN} and Γ_{OUT} determined by fitting each RTS to the two-state model results. The parameters $\overline{\Gamma^{\downarrow}}$, $\overline{\Gamma^{\uparrow}}$, and the zero-detuning voltage V_0 were determined by least-squares fit. The energy dependence parameter β was found to be approximately the same at every magnetic field, about 835 meV^{-1}. The electron temperature was assumed to be the same as the refrigerator base temperature, 240 mK. The gross tunnel rates determined by this fit at magnetic fields from 1 T to 8 T are shown in Fig. 6.13 (a).

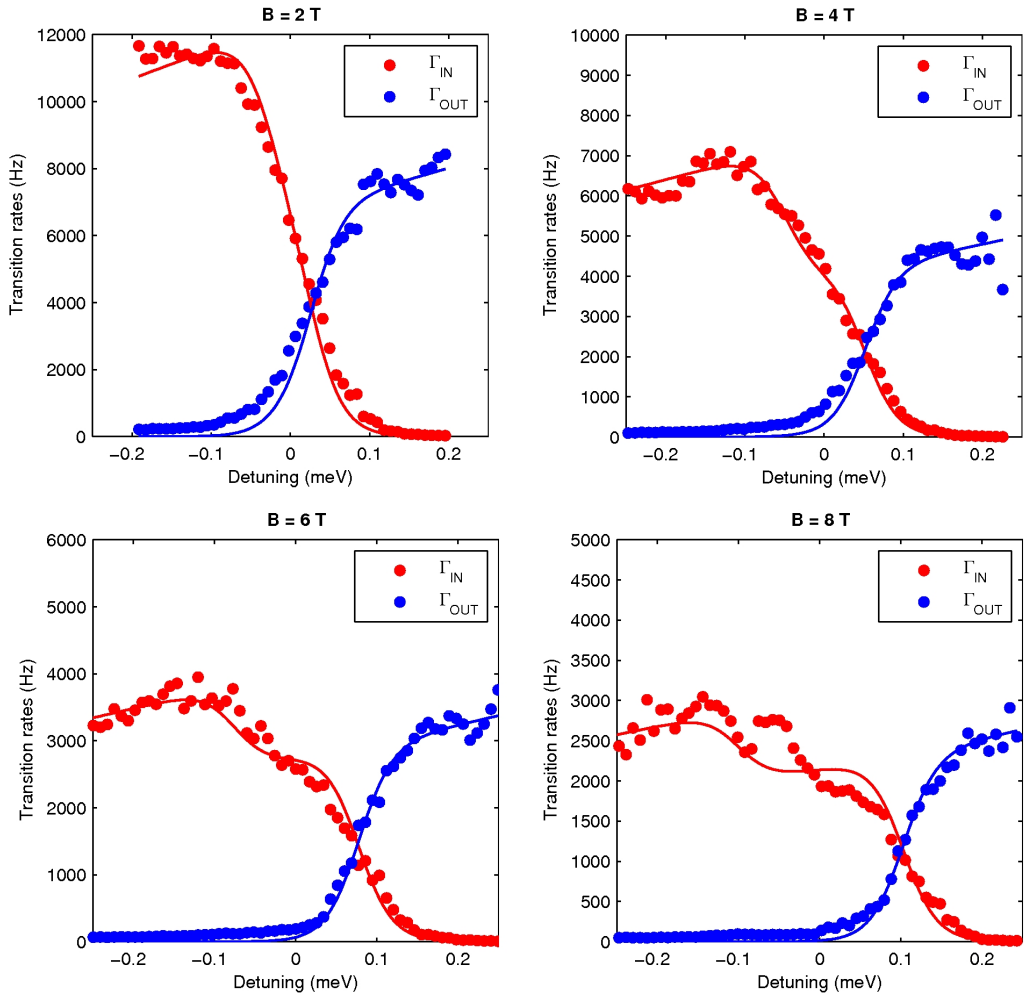

Figure 6.11: Total tunnel rates Γ_{IN} and Γ_{OUT} measured by a two-state HMM as a function of detuning, for four different magnetic fields. Circles are the rates extracted from RTS data sets. The solid line is a fit to the physical model as described in the text.

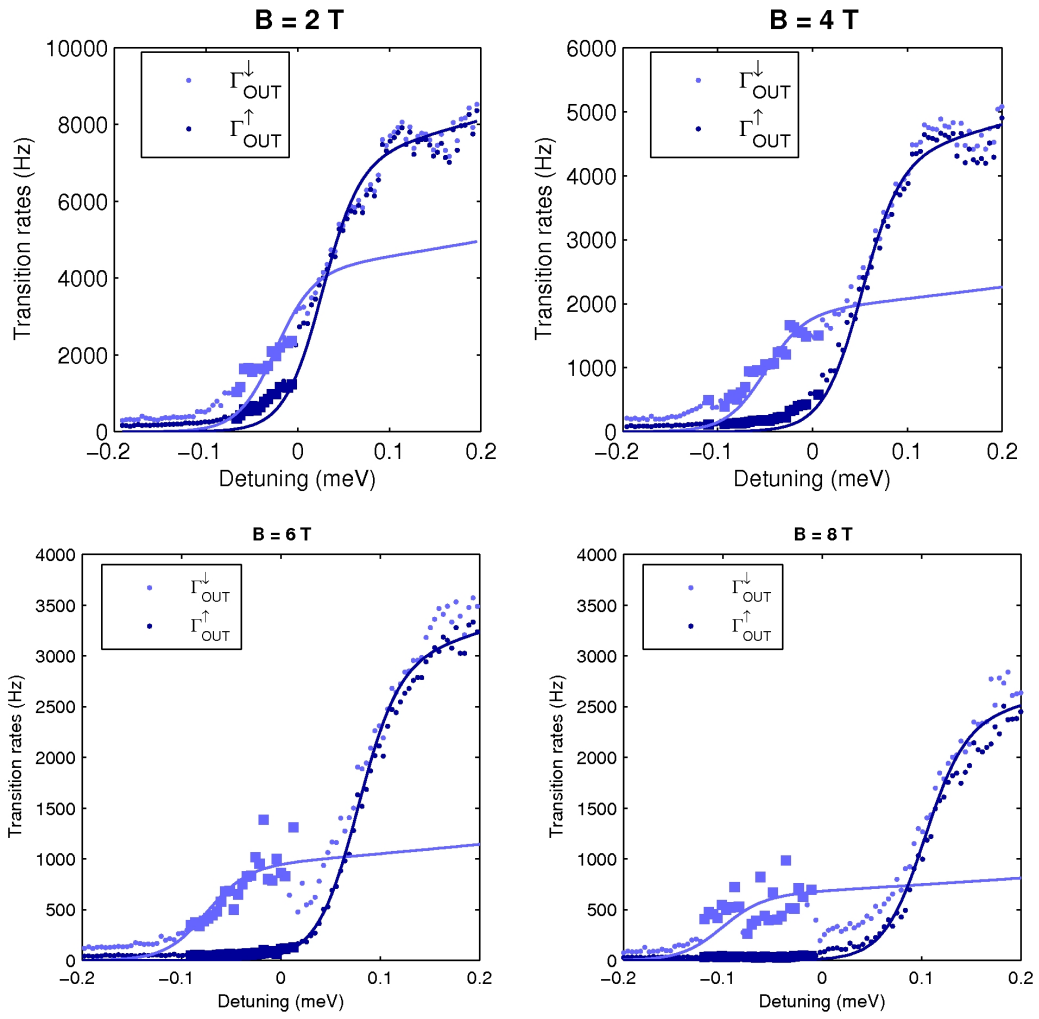

Figure 6.12: Tunnel-out rates for two spins $\Gamma^{\downarrow}_{OUT}$ and $\Gamma^{\uparrow}_{OUT}$ plotted as a function of detuning. Larger, square data point markers indicate the points for which the three-state model was selected. Solid lines indicate the fits to the physical model as described in the text.

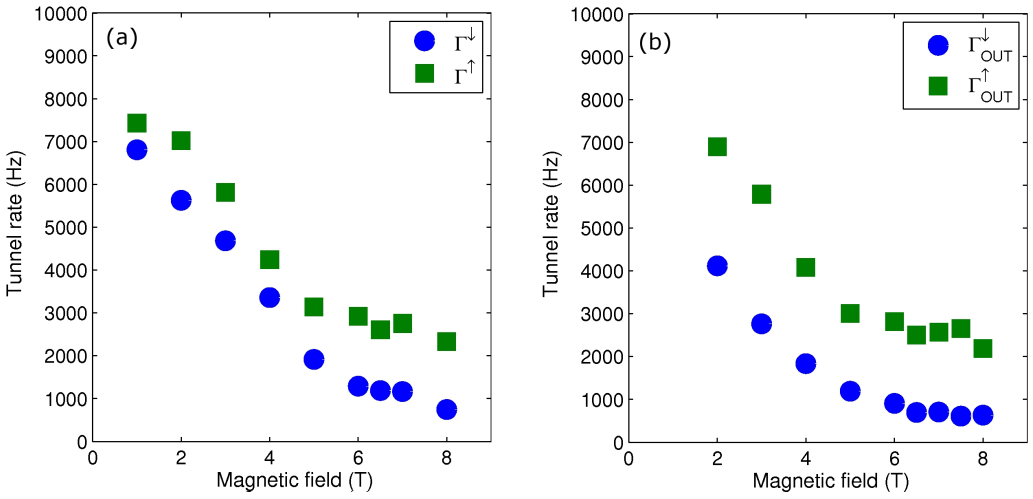

Figure 6.13: (a) Gross tunnel rates for each spin state as a function of magnetic field determined by fitting to the net tunnel rates $\Gamma^{\downarrow}$ and $\Gamma^{\uparrow}$. (b) Gross tunnel rates for each spin state as a function of magnetic field as determined by fitting to the tunnel-out rates $\Gamma^{\downarrow}_{OUT}$ and $\Gamma^{\uparrow}_{OUT}$.

Fig. 6.12 shows the tunnel-out rates $\Gamma^{\downarrow}_{OUT}$ and $\Gamma^{\uparrow}_{OUT}$ determined by the three-state HMM. The smaller, circular data points are those for which the two-state model was selected (by BIC), so the two rates cannot be distinguished. In those cases, both rates tend to match the ground-state tunnel rate (most of the electron transitions being from the ground state). Larger squares indicate those data points for which the three-state model was selected, and the excited state tunnel rate $\Gamma^{\downarrow}_{OUT}$ is distinguishable. The solid lines indicate fits of Eq. (6.14) to these data; the spin-up rate was fit to all of the spin-up data points, while the spin-down rate was fit only to those data points for which the three-state model was selected. The gross tunnel rates found in this fit are shown in Fig. 6.13 (b). The spin-up tunnel rate is almost exactly the same as was found by fitting to the total tunneling rates, but the spin-down tunnel rate is generally smaller than those found from the total tunnel rates.

Amasha, *et al.* discussed the difference in spin tunnel rates in terms of the ratio $\chi = \Gamma^{\downarrow}/\Gamma^{\uparrow}$. In Fig. 6.14 we plot this ratio, obtained in two different ways discussed above, as a function of magnetic field. Both methods show a significant dependence of the tunnel rate on

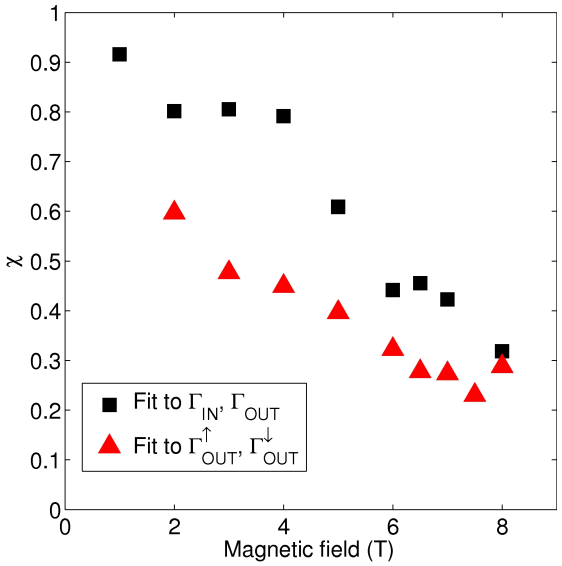

Figure 6.14: The ratio of tunnel rates for the two spin states, $\chi = \Gamma^{\downarrow}/\Gamma^{\uparrow}$ plotted as a function of magnetic field. Two sets of results are plotted, for two different methods of measuring the tunnel rates of the individual spins.

the spin state, which increases at high magnetic field, similar to what was found by Amasha, *et al.*. They observed χ to decrease approximately linearly until it was zero at about $B = 7.5$ T. We see similar behavior here, except that χ is not going to zero as rapidly; if it is a linear dependence, χ=0 may occur around B = 10-12 T. Since the specific tuning of the dot can have a strong influence on the spin dependence χ, it is not surprising that our results agree qualitatively, but not quantitatively, with those of Amasha, *et al.* [AMR08b].

The two methods of determining χ do not completely agree. Both methods agree about the tunnel rate of the ground state $\Gamma^{\uparrow}$, but the three-state model's values for $\Gamma^{\downarrow}$ are consistently smaller than those found by fitting to the total tunnel rates (from the two-state model). This may be because the tunnel-out rates are different from the tunnel-in rates. Such a difference would imply that the quantum dot is not in thermal equilibrium with the reservoir, which may be true due to the back-action of the QPC on the quantum dot [LXC12]. It may also be the case that either fitting these tunnel rate equations to the total

tunneling rates overestimates the gross tunnel rate $\Gamma^{\downarrow}$, the three-state HMM underestimates the same quantity, or that the physical model we have used for tunneling, Eq. 6.14 is not correct in some way.

6.6.6 Testing for other possible state configurations

We believed *a priori* that there are no more than three electron states of the quantum dot when it is tuned this way, but in order to test that assumption we also constructed two additional types of HMMs. One was a three-state model in which the 1-electron charge state had no hidden state but the 0-electron state did have a hidden (or excited) state. This is obviously an unphysical model according to the interpretation we have given so far, so it should not fit the data better than either of the two models we discussed above. This HMM was fit to all data sets and it was verified that for every RTS the BIC of the fit to this model was greater than either the two-state or three-state models described above.

Another model that was tried was a four-state model in which the 1-electron charge state had two hidden states. Again, in all cases we did not see statistical evidence in favor of this model, as judged by BIC. The best model was always either the two-state model or the three-state model.

6.7 New directions in RTS analysis

Above we have detailed the strategies we have developed for using HMMs to analyze RTS data, showed how we have successfully applied them. In this section we introduce two new concepts that we have been developing for RTS analysis. These are new theoretical ideas that have not been fully applied yet.

6.7.1 RTS as an aggregated Markov process

A RTS, without noise, belongs to a category of statistical processes known as an aggregated Markov process (AMP) [FMR85, FR86, FR92, The05]. Like an HMM, an AMP is based on a Markov process. In AMP formalism, the state of the system is known, except that some of the states of the system cannot be distinguished from one another. They are said to belong to the same *aggregate* or *class*. In our application, any two states with the same number of electrons belong to the same class since they can't be distinguished directly by the charge sensor. For example, in the three-state model, the states have two observation classes:

$$\begin{array}{cc} \left\{ \begin{array}{c} N=1,\downarrow \\ N=1,\uparrow \end{array} \right\} & \text{Conductance class } a \\ N=0 & \text{Conductance class } b \end{array}$$

With the three states broken down into two conductance classes, we can partition the transition matrix 6.8 into submatrices in the following way:

$$Q_{aa} = \begin{pmatrix} -\Gamma^{\downarrow}_{OUT} - W_{\downarrow\uparrow} & W_{\downarrow\uparrow} \\ W_{\uparrow\downarrow} & -W_{\uparrow\downarrow} - \Gamma^{\uparrow}_{OUT} \end{pmatrix} \tag{6.20}$$

$$Q_{ab} = \begin{pmatrix} \Gamma^{\downarrow}_{OUT} \\ \Gamma^{\uparrow}_{OUT} \end{pmatrix} \tag{6.21}$$

$$Q_{ab} = \begin{pmatrix} \Gamma^{\downarrow}_{IN} & \Gamma^{\uparrow}_{IN} \end{pmatrix} \tag{6.22}$$

$$Q_{bb} = \begin{pmatrix} -\Gamma^{\downarrow}_{IN} - \Gamma^{\uparrow}_{IN} \end{pmatrix} \tag{6.23}$$

so that Q_{aa} is the transition matrix describing transitions between states within class a, Q_{bb} is the matrix for transitions within class b[3], and Q_{ab} and Q_{ba} are the matrices for transitions between classes. The probability of the system entering into each state $|\downarrow\rangle$ and $|\uparrow\rangle$, given that we have just observed it enter class a, obeys the equation [Kie89]:

$$\boldsymbol{\pi_a} = \boldsymbol{\pi_a} Q_{aa}^{-1} Q_{ab} Q_{bb}^{-1} Q_{ba}. \tag{6.24}$$

[3]In our case since there is only one state in class b, it is a 1x1 matrix.

To find the probabilities $\boldsymbol{\pi_a}$, we solve this eigenvector equation (for eigenvalue 1). For the present model,

$$Q_{aa}^{-1}Q_{ab}Q_{bb}^{-1}Q_{ba} = \frac{1}{\Gamma_{IN}^{\downarrow}+\Gamma_{IN}^{\uparrow}}\begin{pmatrix}\Gamma_{IN}^{\downarrow} & \Gamma_{IN}^{\downarrow}\\ \Gamma_{IN}^{\uparrow} & \Gamma_{IN}^{\uparrow}\end{pmatrix} \tag{6.25}$$

which leads to

$$\boldsymbol{\pi}_{\boldsymbol{a}}^{T} = \frac{1}{\Gamma_{IN}^{\downarrow}+\Gamma_{IN}^{\uparrow}}\begin{pmatrix}\Gamma_{IN}^{\downarrow}\\ \Gamma_{IN}^{\uparrow}\end{pmatrix}. \tag{6.26}$$

The probability density of the electron staying in the dot for a dwell time t_a before tunneling out is,

$$p(t_a) = \boldsymbol{\pi_a}\exp[Q_{aa}t_a]Q_{ab}\boldsymbol{u_a} \tag{6.27}$$

where $\boldsymbol{u_a}$ is a vector of appropriate length whose elements are all 1. If $W_{\downarrow\uparrow} = W_{\uparrow\downarrow} = 0$, we get the simplification

$$p(t_a) = \frac{\Gamma_{IN}^{\downarrow}\Gamma_{OUT}^{\downarrow}\exp[-\Gamma_{OUT}^{\downarrow}t_a] + \Gamma_{IN}^{\uparrow}\Gamma_{OUT}^{\uparrow}\exp[-\Gamma_{OUT}^{\uparrow}t_a]}{\Gamma_{IN}^{\downarrow}+\Gamma_{IN}^{\uparrow}}. \tag{6.28}$$

This is a bi-exponential distribution. We can now see how the presence of the extra hidden state can be detected statistically: the distribution $p(t_a)$ is bi-exponential if two states with distinct tunneling-out rates are present, but if only one state is present, the distribution would be a simple exponential. If the two tunneling rates are the same, the distribution reduces to a simple exponential, the same form as if there was no hidden state.

For the 0-electron conductance class, $\boldsymbol{\pi_b} = \mathbf{1}$ trivially and

$$p(t_b) = \boldsymbol{\pi_b}\exp[Q_{bb}t_b]Q_{ba}\boldsymbol{u_b} = (\Gamma_{IN}^{\downarrow}+\Gamma_{IN}^{\uparrow})\exp[-(\Gamma_{IN}^{\downarrow}+\Gamma_{IN}^{\uparrow})t_b]. \tag{6.29}$$

Unlike the tunnel-out rate distribution above, this distribution is a simple exponential. This explains why the two states cannot be distinguished by the rate of transition into these states: the exponential distribution here is the same distribution we would get if there was a single state with an tunnel-in rate $\Gamma_{IN} = \Gamma_{IN}^{\downarrow} + \Gamma_{IN}^{\uparrow}$. Thus, the total tunnel-in rate is encoded in $p(t_b)$, but the rates of the individual spins are not.

The joint probability of a dwell time of length t_a in the 1-electron class followed immediately by a dwell time of t_b in the 0-electron class is

$$p(t_a, t_b) = \boldsymbol{\pi_a} \exp[Q_{aa} t_a] Q_{ab} \exp[Q_{bb} t_b] Q_{ba} \boldsymbol{u_a}. \tag{6.30}$$

Likewise the joint probability for the opposite sequence is

$$p(t_b, t_a) = \boldsymbol{\pi_b} \exp[Q_{bb} t_b] Q_{ba} \exp[Q_{aa} t_a] Q_{ab} \boldsymbol{u_b}. \tag{6.31}$$

Since class b has only one state, the matrix Q_{ab} has rank 1, these expressions factor out and there is no correlation between t_a and t_b [The05]:

$$p(t_a, t_b) = p(t_b, t_a) = p(t_a) p(t_b). \tag{6.32}$$

Thus, if we detect significant correlation between t_a and t_b, we could conclude that there are at least *four* states participating in the RTS, two for each class.

AMP theory is more straightforward than HMM and it is easier to make comparisons between experimental results and theory. The biggest drawback of using an AMP to represent the system compared to an HMM is that it cannot incorporate the signal noise into the model directly, as we can with HMM. For this reason we have found it practically difficult to apply AMP theory (*i. e.* by forming histograms of dwell times and comparing to distributions 6.27 and 6.29), but the theory is very useful for understanding the statistics of RTS. In the future it might be possible to obtain data with high enough signal-to-noise ratio that the noise does not matter, or to find a better way of handling noise so that good quality histograms can be made.

6.7.2 Quantum mechanical RTS model

The hidden Markov model was developed in response to statistical problems independent of quantum physics and so are based on the Markov model, one of the simplest stochastic processes. It is appropriate to the problem of RTS analysis as described above, provided that the system in question does not exhibit quantum coherent behavior at the timescale of

the transition rates. In the experiments described in this chapter, the transition rates are on the order of 10 kHz or less, while the dephasing rate $(T_2^*)^{-1}$ is on the order of 100 MHz or more for spin states in in GaAs [PJT05]. The coherent behavior of the system decays away much faster than we could observe it, so representing the system as a classical Markov process is appropriate. In future experiments the coherent evolution of the system may be an important part of the dynamics we wish to model and to measure. In this section we sketch an approach to expanding the theory of HMM to include quantum coherent behavior.

The quantum mechanical analog of the Markov equation is the Lindblad equation,

$$\frac{d}{dt}\rho = -\frac{i}{\hbar}\left[H, \rho\right] + \sum_{n,m=1}^{N^2-1} h_{n,m}\left(-\rho L_m^\dagger L_n - L_m^\dagger L_n \rho + 2 L_n L_m^\dagger\right) \tag{6.33}$$

where ρ is the density matrix of the system, H is the Hamiltonian, and the remaining terms at the right represent the non-unitary evolution of the system, for example capturing the interaction of the system with extra degrees of freedom in the environment. This equation describes the time evolution of the coherent system in analogy to the continuous time Markov equation, Eq. 6.4. We can construct a quantum version of the hidden Markov model based on the Lindblad equation.

To begin to develop such an idea, we leave out the terms leading to non-unitary evolution and reduce Eq. (6.33) to the fully coherent form

$$\frac{d}{dt}\rho = -\frac{i}{\hbar}\left[H, \rho\right] = -\frac{i}{\hbar}\left(H\rho - \rho H\right) \tag{6.34}$$

which is the von Neumann equation, or quantum Liouville equation. There is a direct analogy between the probability vector $\boldsymbol{p}$ in the HMM and the density matrix ρ in the quantum version. The continuous time transition matrix Q is analogous to the Hamiltonian H, and the discrete time transition matrix A is analogous to the unitary time evolution operator U, where $U = \exp(-iH\Delta t/\hbar)$.

Suppose that at regular intervals Δt a strong, instantaneous measurement is made on the quantum system represented by ρ. Let the times at which measurements are made be $t_n = n\Delta t$, and the set of measurement results be y_n. The operators which describe the

possible measurement outcomes are Y_k and their corresponding eigenvalues y_k. We would like to construct the likelihood function of the data sequence, which is $p(\boldsymbol{y}|H, \rho_0)$ where ρ_0 is the initial value of the density matrix at $t = 0$. We need to do this in such a way that the likelihood function can be calculated efficiently, as it is in the forward-backward procedure for HMMs [Rab89].

The probability of observing the value y_n at time t_n is

$$p(y_n = y_k) = Tr\left[\rho(t_n^{(-)})Y_k\right]. \tag{6.35}$$

where $\rho(t_n^{(-)})$ is the density matrix immediately before the measurement at time t_n. The measurement changes the density matrix from $\rho(t_n^{(-)})$ to $\rho(t_n^{(+)})$ immediately after, which are related according to the measurement outcome by

$$\rho(t_n^{(+)}) = \frac{P_k\rho(t_n^{(-)})P_k}{Tr\left[P_k\rho(t_n^{(-)})\right]} \tag{6.36}$$

where P_k are the Lüders projection operators of the measurement. Here we have assumed that Y_k has a unique projection operator. Between two measurement times t_n and t_{n+1} the system evolves according to,

$$\rho(t_{n+1}^{(-)}) = U\rho(t_n^{(+)})U^\dagger \tag{6.37}$$

Now to calculate the likelihood function efficiently we note that we can construct the same "forward variables" as are used in computing the likelihood function of an HMM. Let the forward variables α_n be defined as

$$\alpha_n = p(y_1, y_2, \ldots, y_n|H, \rho_0). \tag{6.38}$$

From the expressions above we can see that there is a recursive relationship between the α values

$$\alpha_n = Tr(P_{y_n}\rho_n^{(-)})\alpha_{n-1} \tag{6.39}$$

which means that the complete likelihood function $p(\boldsymbol{y}|H, \rho_0) = \alpha_N$ can be computed recursively, as it is for ordinary HMMs. Given the ability to compute the likelihood function,

we can find the parameters H and ρ_0 that maximize the likelihood using any appropriate optimization algorithm. The EM algorithm is not needed in this case, but might be useful.

Here we have shown that the likelihood function has a similar recursive structure to a classical HMM, so it should be possible to calculate the likelihood function efficiently and from there build up a fully quantum mechanical theory. So far we have left out a number of important details, such as how to handle non-unitary operators, measurement operators with non-unique eigenvalues, scaling the forward variables, and more. Producing a complete and useful theory will require more development than we have made so far, but here we shown that it is possible and have outlined a path for such development.

6.8 Conclusions

RTSs are a widespread phenomenon in condensed matter physics, arising from ordinary fluctuations of charges in small traps. Lateral quantum dots are one example of a trap which can experience a single charge fluctuation, a particularly interesting system because of the degree of control we have over the energy levels, tunnel coupling, and symmetry of the trap. Thus RTS in quantum dots are interesting to study as a model system for other charge traps, as well as being a potentially useful technology in its own right. In particular, we are interested in using the spin of the electron trapped in a quantum dot for quantum information processing purposes and studies of quantum coherence. For that reason we wish to understand the spin dynamics of these quantum dots as much as possible. Here we have described a new approach to analyzing RTS based on the HMM which can distinguish the spin states and determine their dynamics directly.

Fitting the RTS to HMMs allows us to apply a simple mathematical model to the data, without making any assumptions about the physics of the system other than the number of quantum states it has and the Markov condition. In cases where the transition rates between states are distinct, the presence of "hidden" states such as spin can be detected by an objective statistical criterion, and at least some of the transition rates of these states

can be determined. This allows us to study spin-state dependence of tunneling rates, and spin relaxation rates, *even though the charge sensor is not directly sensitive to the spin state of the electron.* The construction of the HMM is designed to make this type of inference possible.

As part of the process of developing these analysis techniques we deliberately focused on a simple case, of a zero-electron or one-electron quantum dot with no more than three possible states. It is easy to imagine that this approach could be applied much more broadly, to study RTS which appear in different contexts, and may have more complicated dynamics than we have studied so far (*i. e.* having more "hidden" states). We outlined some directions for further theoretical development of these ideas. There is much room for further development, both theoretically and in applications.

CHAPTER 7

Conclusions

It's what you learn after you know it all that counts.

- J. R. Wooden

The proposal by Loss and DiVincenzo in 1998 to use semiconductor quantum dots as a basis for quantum information processing has inspired a great deal of research interest over the past decade or more, including all of the work presented in this dissertation [LD98]. The crucial idea they proposed was to use the exchange interaction between two electrons to manipulate their spin states. The exchange interaction potentially overcomes one of the crucial issues that limits our ability to control the quantum states of microscopic systems: generally, those systems which can be easily manipulated also have relatively strong interactions with their environment and so lose their coherence rapidly. We are usually forced to choose between systems which can be easily controlled but have poor coherence (*e. g.* charge qubits), or those which maintain their coherence well but their state can't be controlled quickly or easily (*e. g.* nuclear spins). The exchange interaction provides a way to take a spin, which is fundamentally magnetic and has weak interactions with the environment, and manipulate it with electric signals. The turn-on of the exchange interaction between two electrons in a double quantum dot is exponential with respect to the gate voltage that controls the barrier between them, which means that the interaction strength can be orders of magnitude stronger than the magnetic dipole interactions of the spins when they are separated. We can turn the interaction between two spins on and off with high fidelity using a simple voltage pulse on an electrode. No other quantum system offers the same degree of control over an interaction at the microscopic level in such a simple way.

The overall goal of our research group's efforts over the past five years and more has been to contribute to the technology and scientific understanding of these quantum dots that will lead help make progress towards their use in future quantum information processing technology. Researchers in our lab and around the world have demonstrated detection, manipulation, and read-out of single spins in solid state systems. Since humanity already has the ability to pattern highly detailed circuits and MEMS elements in solid state materials, there is a definite possibility that these single-spin qubits can be scaled up into a quantum computer with enough complexity to do meaningful calculations. Such a machine is still many years away, but basic physics and proof-of-principle experiments that pave the way for such a computer are presently being done.

The particular system which we have developed and studied has been the silicon MOS quantum dot. These devices were developed and first demonstrated by M. Xiao in our lab, and we continue to use his recipe with only small modifications today. We have demonstrated single dots [XHJ10a, XHJ10b], double dots [HPX11], and recently triple dots [H. Pan, *et al.*, in review] in the silicon MOSFET structure. We designed and developed QPC-like charge sensing channels and techniques for reading out the charge state of these quantum dots and applied many of the techniques developed for GaAs quantum dots to study these new devices. We have demonstrated that our silicon MOS quantum dots, while having some unique challenges, are able to confine and control electrons in much the same way that lateral quantum dots in GaAs quantum wells do.

Charge sensing of the electron state of the quantum dot was crucial to the success of our experiment to measure the spin relaxation time of the electron, T_1. Using the spin state read-out technique pioneered by Elzermann, *et al.*, we were able to measure the decay of the spin-excited-state population over time and assign a relaxation time to the decay, at various magnetic fields. At high magnetic field, we observed that the spin relaxation time decays rapidly as a function of magnetic field, as expected if the dominant relaxation mechanism is by the emission of a longitudinal acoustic phonon. At lower magnetic fields, we saw T_1 saturate at about 30 ms. We do not know the reason for this limit, but other researchers

have seen a similar effect that was device-dependent. Since we measured only one device, it is possible this limit is not fundamental. Other researchers have measured T_1 longer than 1 second [SPV11, MPZ10] in similar silicon systems.

Coupling quantum systems to photons in a resonant cavity, cavity quantum electrodynamics, has been a highly successful method for studying the interactions between matter and light, and has a great deal of promise as well in quantum information processing applications. This has been demonstrated in past few years with great success using superconducting qubits constructed from Josephson junction devices, coupled to superconducting microwave resonant cavities. We have developed a similar system, using a semiconductor double quantum dot as the charge qubit instead of a superconducting qubit. Such a system potentially has all of the advantages of a semiconductor qubit, especially the long coherence time of the spin state. To date we have demonstrated interactions between the microwave resonator and electrons in the MOSFET channel, but have not yet established clear evidence of the quantum dot interacting with the resonator. A redesigned device is being developed and studied by our collaborators at UC Berkeley to better isolate the quantum dot from its surrounding MOSFET channel, so that its interactions with the resonator can be seen independently.

In another approach to studying the spin state dynamics in semiconductor quantum dots, we developed a method for extracting information about electron spin states and their dynamics from random telegraph signal data. Our techniques allow us to detect the presence of spin states with distinct tunnel rates, and to measure their dynamics indirectly. Other ways of measuring electron spin dynamics require that the Zeeman energy difference between the two spin states be larger than the thermal energy, but our strategy of studying random telegraph signals works at energies comparable to or less than the thermal energy scale. This allows us to probe a new energy regime of the quantum dot. We confirmed that at finite magnetic field the tunneling rates of the two spin states of the electron are not the same, and this is true even at magnetic fields lower than the thermal energy. The approach we developed for modeling and analyzing random telegraph signal data has significant promise for future development.

To conclude, we should acknowledge that the study of single-electron devices and single-spin systems in the solid state has a bright future, in silicon quantum dots and many other such systems. Much progress has been made in developing and understanding these systems in the past decade or two, and there is every reason to believe that progress will continue into the future. In the present era of condensed matter science we are gaining the ability to directly prepare, manipulate, and measure quantum-coherent systems in the solid state. There are any number of scientific and technological advancements that will follow, some of which are not yet imagined.

APPENDIX A

Fabrication recipes

Here is a summary of some recipes for fabrication of silicon MOS quantum dot devices. Fabrication is described in more detail in chapter 2.

A.1 Positive photoresist recipe for AZ5214

1. **Spin on HMDS:** 5 seconds @ 500 RPM, 50 seconds @ 4000 RPM.
2. **Spin on AZ5214-EIR:** 5 seconds @ 500 RPM, 50 seconds @ 400 RPM.
3. **Pre-bake:** 60 seconds on a hotplate at 100 °C.
4. **Expose:** 13 seconds exposure time on Karl Suss MA6 mask aligner, 365 nm radiation at 8.0 mW/cm^2.
5. **Develop:** 30 seconds in AZ400K 1 : 4 deionized water. Rinse 1 minute in DI water, blow dry with N_2.
6. **Post-bake:** 120 seconds on hotplate at 100 °C.

A.2 Image reversal (negative) photoresist recipe for AZ5214

1. **Spin on HMDS:** 5 seconds @ 500 RPM, 50 seconds @ 4000 RPM.
2. **Spin on AZ5214-EIR:** 5 seconds @ 500 RPM, 60 seconds @ 400 RPM.
3. **Pre-bake:** 60 seconds on a hotplate at 100 °C.

4. **Pattern expose:** With mask in place, expose 6 seconds on Karl Suss MA6 mask aligner, 365 nm radiation at 8.0 mW/cm^2.

5. **Inversion-bake:** 75 seconds on hotplate at 110 °C.

6. **Flood exposure:** Flood expose entire sample (no mask) 75 seconds on Karl Suss MA6 mask aligner, 365 nm radiation at 8.0 mW/cm^2.

7. **Develop:** 30 seconds in AZ400K 1 : 4 deionized water. Rinse in deionized water 60 seconds, blow dry with N_2.

8. **Post-bake:** 120 seconds on hotplate at 100 °C.

A.3 Electron beam lithography recipe

1. **Spin on PMMA:** PMMA 950 C2 resist, 5 seconds at 500 RPM, 50 seconds at 4500 RPM

2. **Pre-bake:** 15 minutes on hotplate at 145 °C.

3. **Expose:** Exposed on Hitachi S-3000H SEM equipped with NPGS. Electron energy 30 keV. Dosages used depending on feature size:

    - 40 nm: line exposure, 1.3 nC/cm
    - 50-100 nm: area exposure, 750 nC/cm^2
    - 100-250 nm: 600 nC/cm^2
    - 250-500 nm: 500 nC/cm^2
    - 500-1000 nm: 400 nC/cm^2
    - ¿1000 nm: 300 nC/cm^2

4. **Develop:** MIBK 1 : 3 IPA developer for 50 seconds. Rinse thoroughly in IPA, blow dry with N_2.

A.4 Si MOS quantum dot fabrication procedures

This is the standard fabrication recipe for double-gated Si MOS quantum dot devices with Cr/Au metallization for the depletion gates.

1. Etch SiO_2 for ohmic contact windows and alignment markers
   (a) Photolithography to define etch windows (AZ5214 positive recipe)
   (b) Etch SiO_2 with BOE 1:6, 60 seconds
   (c) Remove photoresist by 20 minutes soak in acetone
2. Define n^+ doped regions for ohmic contacts to 2DEG by ion implantation
   (a) Photolithography to define implantation windows (AZ5214 positive)
   (b) Implantation of phosphorus ions, $2 \cdot 10^{15}$ cm^2 dosage at 40 keV (Performed by Leonard Kroko, Inc., 2822-D Walnut Ave., Tustin CA 92780).
   (c) Remove photoresist by 20 minutes soak in acetone
   (d) Anneal in high vacuum oven, 35 minutes at 950 °C.
3. Metallization 1: depletion gate leads, SEM alignment marks
   (a) Photolithography to define lift-off windows (AZ5214, positive)
   (b) Deposit 5 nm Cr + 50 nm Au by thermal evaporation
   (c) Lift-off in acetone
4. Metallization 2: quantum dot depletion gates
   (a) E-beam lithography (PMMA 950 C2) to define depletion gates
   (b) Deposit 5 nm Cr + 50 nm Au by thermal evaporation
   (c) Lift-off in PG remover, soaked overnight at 70 °C.
5. Aluminum oxide layer

(a) Deposit 100 nm Al_2O_3 by ALD, 910 layers

(b) Photolithography to define Al_2O_3 etch windows (AZ5214, positive)

(c) Etch in Transene Transetch-N @ 155 °C. (hotplate temperature), two dunks in etchant, 5 sec. each

(d) Remove photoresist by 20 minute soak in acetone

6. Metallization 3: top gate, ohmic contact pads

(a) Photolithography to open lift-off windows (AZ5214, positive)

(b) Deposit 300 nm Al by thermal evaporation

(c) Lift-off in acetone

7. Anneal for Al_2O_3 and ohmic contacts in forming gas (15% H_2, pressure 15" Hg) @ 430 C., 30 minutes

8. Dice, mount, and bond sample to chip carrier

A.5 Si MOS quantum dot fabrication procedures for aluminum depletion gates

This recipe was used for devices requiring aluminum metallization for the depletion gate layer, including the devices that incorporated a superconducting microwave resonator.

1. Etch SiO_2 for ohmic contact windows and alignment markers

(a) Photolithography to define etch windows (AZ5214 positive recipe)

(b) Etch SiO_2 with BOE 1:6, 60 seconds

(c) Remove photoresist by 20 minutes soak in acetone

2. Define n^+ doped regions for ohmic contacts to 2DEG by ion implantation

(a) Photolithography to define implantation windows (AZ5214 positive)

(b) Implantation of phosphorus ions, $2 \cdot 10^{15}$ cm^2 dosage at 40 keV (Performed by Leonard Kroko, Inc., 2822-D Walnut Ave., Tustin CA 92780).

(c) Remove photoresist by 20 minutes soak in acetone

(d) Anneal in high vacuum oven, 35 minutes at 950 °C.

3. Metallization 1: depletion gate leads, SEM alignment marks

(a) Photolithography to define lift-off windows (AZ5214, positive)

(b) Deposit 5 nm Cr + 50 nm Au by thermal evaporation

(c) Lift-off in acetone

4. Metallization 2: quantum dot depletion gates

(a) E-beam lithography (PMMA 950 C2) to define depletion gates lift-off windows.

(b) Deposit 50 nm Al by thermal evaporation

(c) Lift-off in PG remover, soaked overnight at 70 °C.

5. Metallization 3: resonator, resonator feeds

(a) Photolithography to define lift-off windows (AZ5214, positive)

(b) In-situ exposure to Ar plasma: 0.05 torr Ar gas pressure, 30 watts forward RF power, 8 minutes.

(c) Deposit 50 nm Al by thermal evaporation

(d) Lift-off in acetone

6. Metallization 4: Al2O3 etchant protective layer

(a) Photolithography to define Au protection layer (AZ5214, positive)

(b) Deposit 5 nm Al, 80 nm Au by thermal evaporation

(c) Lift-off in acetone

7. Aluminum oxide layer

    (a) Deposit 100 nm Al_2O_3 by ALD, 910 layers

    (b) Photolithography to define Al2O3 etch windows (AZ5214, positive)

    (c) Etch in Transene Transetch-N @ 155 C. (hotplate temperature), two dunks in etchant, 5 sec. each

    (d) Remove photoresist by 20 minute soak in acetone

8. Remove Al2O3 etchant protective layer

    (a) Photolithography to define protection layer etch windows (AZ5214, positive)

    (b) 15 seconds etch in Transene Type TFA gold etchant

    (c) Remove photoresist by 20 minutes soak in acetone

9. Metallization 5: top gate, ohmic contact pads

    (a) Photolithography to open lift-off windows (AZ5214, large markers)

    (b) Deposit 300 nm Al by thermal evaporation

    (c) Lift-off in acetone

10. Anneal for Al_2O_3 and ohmic contacts in forming gas (15% H_2, pressure 15" Hg) @ 430 C., 30 minutes

11. Dice, mount, and bond sample to chip carrier

References

[ABG02] I.L. Aleiner, P.W. Brouwer, and L.I. Glazman. "Quantum effects in Coulomb blockade." *Physics Reports*, **358**(56):309 – 440, 2002.

[AFS82] T. Ando, A. B. Fowler, and F. Stern. "Electronic properties of two-dimensional systems." *Rev. Mod. Phys.*, **54**(2):437–672, 1982.

[AKN11] R. Amsüss, Ch. Koller, T. Nöbauer, S. Putz, S. Rotter, K. Sandner, S. Schneider, M. Schramböck, G. Steinhauser, H. Ritsch, J. Schmiedmayer, and J. Majer. "Cavity QED with Magnetically Coupled Collective Spin States." *Phys. Rev. Lett.*, **107**:060502, Aug 2011.

[AM76] N. W. Ashcroft and N. D. Mermin. *Solid State Physics*. Thomson Learning, Inc., 1976.

[Ama08] S. Amasha. *Electron Tunneling and Spin Relaxation in a Lateral Quantum Dot*. PhD thesis, Massachusetts Institute of Technology, December 2008.

[AMR08a] S. Amasha, K. MacLean, I. P. Radu, D. M. Zumbuhl, M. A. Kastner, M. P. Hanson, and A. C. Gossard. "Electrical Control of Spin Relaxation in a Quantum Dot." *Phys. Rev. Lett.*, **100**:046803, 2008.

[AMR08b] S. Amasha, K. MacLean, Iuliana P. Radu, D. M. Zumbühl, M. A. Kastner, M. P. Hanson, and A. C. Gossard. "Spin-dependent tunneling of single electrons into an empty quantum dot." *Phys. Rev. B*, **78**:041306, Jul 2008.

[ANP06] O. Astafiev, Y. Nakamura, Yu. A. Pashkin, T. Yamamoto, and J. S. Tsai. "Comment on "Charge-Qubit Operation of an Isolated Double Quantum Dot"." *Phys. Rev. Lett.*, **97**:208901, Nov 2006.

[APC11] Lucy V. C. Assali, Helena M. Petrilli, Rodrigo B. Capaz, Belita Koiller, Xuedong Hu, and S. Das Sarma. "Hyperfine interactions in silicon quantum dots." *Phys. Rev. B*, **83**:165301, Apr 2011.

[Bar10] C. Barthel. *Control and fast Measurement of Spin Qubits*. PhD thesis, Massachusetts Institute of Technology, 2010.

[BDS96] Charles H. Bennett, David P. DiVincenzo, John A. Smolin, and William K. Wootters. "Mixed-state entanglement and quantum error correction." *Phys. Rev. A*, **54**:3824–3851, Nov 1996.

[BE68] L. E. Baum and J. A. Egon. "Growth functions for transformations on manifolds." *Pac. J. Math.*, **27**(2):211–227, 1968.

[BFB09] R. Bianchetti, S. Filipp, M. Baur, J. M. Fink, M. Göppl, P. J. Leek, L. Steffen, A. Blais, and A. Wallraff. "Dynamics of dispersive single-qubit readout in circuit quantum electrodynamics." *Phys. Rev. A*, **80**:043840, Oct 2009.

[BH04] R. Bhar and S. Hamori. *Hidden Markov models: Applications to financial economics*. Kluwer Academic, Boston, Mass., 2004.

[BHW04] Alexandre Blais, Ren-Shou Huang, Andreas Wallraff, S. M. Girvin, and R. J. Schoelkopf. "Cavity quantum electrodynamics for superconducting electrical circuits: An architecture for quantum computation." *Phys. Rev. A*, **69**:062320, Jun 2004.

[BI06] Guido Burkard and Atac Imamoglu. "Ultra-long-distance interaction between spin qubits." *Phys. Rev. B*, **74**:041307, Jul 2006.

[BKE04] Timothy B. Boykin, Gerhard Klimeck, M. A. Eriksson, Mark Friesen, S. N. Coppersmith, Paul von Allmen, Fabiano Oyafuso, and Seungwon Lee. "Valley splitting in strained silicon quantum wells." *Applied Physics Letters*, **84**(1):115–117, 2004.

[BRR98] P. J. Bickel, Y. Ritov, and T. Ryden. "Asymptotic Normality of the Maximum-Likelihood Estimator for General Hidden Markov Models." **26**(4):1614–1635, 1998.

[BSP06] P. Becker, D. Schiel, H-J Pohl, A. K. Kaliteevski, O. N. Godisov, M. F. Churbanov, G. G. Devyatykh, A. V. Gusev, A. D. Bulanov, S. A. Adamchik, V. A. Gavva, I. D. Kovalev, N. V. Abrosimov, B. Hallmann-Seiffert, H. Riemann, S. Valkiers, P. Taylor, P. De Bievre, and E. M. Dianov. "Large-scale production of highly enriched 28Si for the precise determination of the Avogadro constant." *Meas. Sci. Technol.*, **17**:1854–1860, 2006.

[But90] M. Buttiker. "Quantized transmission of a saddle-point constriction." *Phys. Rev. B*, **41**(11):7906–7909, 1990.

[CDC07] M. C. Cassidy, A. S. Dzurak, R. G. Clark, K. D. Petersson, I. Farrer, D. A. Ritchie, and C. G. Smith. "Single shot charge detection using a radio-frequency quantum point contact." *Appl. Phys. Lett.*, **91**:222104, 2007.

[CDG92] C. Cohen-Tannoudji, J. Dupont-Roc, and G. Grynberg. *Atom-Photon Interactions*. John Wiley and Sons, Inc., Hoboken, NJ, 1992.

[CMR05] O. Cappe, E. Moulines, and T. Ryden. *Inference in Hidden Markov Models*. Springer, New York, 2005.

[CnL10] Dimitrie Culcer, Łukasz Cywiński, Qiuzi Li, Xuedong Hu, and S. Das Sarma. "Quantum dot spin qubits in silicon: Multivalley physics." *Phys. Rev. B*, **82**:155312, Oct 2010.

[CSK12] Dimitrie Culcer, A. L. Saraiva, Belita Koiller, Xuedong Hu, and S. Das Sarma. "Valley-Based Noise-Resistant Quantum Computation Using Si Quantum Dots." *Phys. Rev. Lett.*, **108**:126804, Mar 2012.

[CWP12] S. J. Chorley, J. Wabnig, Z. V. Penfold-Fitch, K. D. Petersson, J. Frake, C. G. Smith, and M. R. Buitelaar. "Measuring the Complex Admittance of a Carbon Nanotube Double Quantum Dot." *Phys. Rev. Lett.*, **108**:036802, Jan 2012.

[CXL11] G. Cao, M. Xiao, H. O. Li, C. Zhou, R. N. Shang, T. Tu, G. C. Guo, G. P. Guo, and H. W. Jiang. "Back-action Driven Electron Spin Singlet-Triplet Excitation in a Single Quantum Dot." *arXiv*, **cond-mat**:1109.5734v2, 2011.

[DCG09] L. DiCarlo, J. M. Chow, J. M. Gambetta, L. S. Bishop, B. R. Johnson, D. I. Schuster, J. Majer, A. Blais, L. Frunzio, S. M. Girvin, and R. J. Schoelkopf. "Demonstration of two-qubit algorithms with a superconducting quantum processor." *Nature*, **460**:240–244, 2009.

[DiV00] D. P. DiVincenzo. "The Physical Implementation of Quantum Computation." *Fortschr. Phys.*, **48**:771–783, 2000.

[DLJ04] L. DiCarlo, H. J. Lynch, A. C. Johnson, L. I. Childress, K. Crockett, C. M. Marcus, M. P. Hanson, and A. C. Gossard. "Differential Charge Sensing and Charge Delocalization in a Tunable Double Quantum Dot." *Phys. Rev. Lett.*, **92**:226801, Jun 2004.

[DLR77] A. P. Dempster, N. M. Laird, and D. B. Rubin. "Maximum Likelihood from Incomplete Data via the EM Algorithm." *Journal of the Royal Statistical Society. Series B (Methodological)*, **39**(1):pp. 1–38, 1977.

[Dre55] G. Dresselhaus. "Spin-Orbit Coupling Effects in Zinc Blende Structures." *Phys. Rev.*, **100**:580–586, Oct 1955.

[DSP11] M. R. Delbecq, V. Schmitt, F. D. Parmentier, N. Roch, J. J. Viennot, G. Fève, B. Huard, C. Mora, A. Cottet, and T. Kontos. "Coupling a Quantum Dot, Fermionic Leads, and a Microwave Cavity on a Chip." *Phys. Rev. Lett.*, **107**:256804, Dec 2011.

[Dut05] S. M. Dutra. *Cavity Quantum Electrodynamics.* John Wiley and Sons, Inc., Hoboken, NJ, 2005.

[EHB04a] J. M. Elzerman, R. Hanson, L. H. Willems van Beveren, L. M. K. Vandersypen, and L. P. Kouwenhoven. "Excited-state spectroscopy on a nearly closed quantum dot via charge detection." **84**(23):4617–4619, 2004.

[EHB04b] J. M. Elzerman, R. Hanson, L. H. Willems van Beveren, L. M. K. Vandersypen, and L. P. Kouwenhoven. "Excited-state spectroscopy on a nearly closed quantum dot via charge detection." **84**(23):4617–4619, 2004.

[EHB05] J. M. Elzerman, R. Hanson, L. H. W. van Beveren, S. Tarucha, L. M. K. Vandersypen, and L. P. Kouwenhoven. "Semiconductor Few-Electron Quantum Dots as Spin Qubits." *Let. Notes Phys.*, **667**:25–95, 2005.

[Eph02] Y. Ephraim. "Hidden Markov Processes." *IEEE Trans. Inf. Theory*, **40**(6):1518–1569, 2002.

[FAT03] T. Fujisawa, D. G. Austing, Y. Tokura, Y. Hirayama, and S. Tarucha. "Electrical pulse measurement, inelastic relaxation, and non-equilibrium transport in a quantum dot." *J. of Phys.: Cond. Mat.*, **15**:R1395–R1428, 2003.

[FD87] T. A. Fulton and G. J. Dolan. "Observation of Single-Electron Charging Effects in Small Tunnel Junctions." *Phys. Rev. Lett.*, **59**(1):109–112, 1987.

[FFH09] C. Flindt, C. Fricke, F. Hohls, T. Novotny, K. Netocny, T. Brandes, and R. J. Haug. "Universal oscillations in counting statistics." *Proc. Natl. Acad. Sci.*, **106**(25):10116–10119, 2009.

[FH00] T. Fujisawa and Y. Hirayama. "Charge noise analysis of an AlGaAs/GaAs quantum dot using transmission-type radio-frequency single-electron transistor technique." *Appl. Phys. Lett.*, **77**:543, 2000.

[FHS06] Toshimasa Fujisawa, Toshiaki Hayashi, and Satoshi Sasaki. "Time-dependent single-electron transport through quantum dots." *Reports on Progress in Physics*, **69**(3):759, 2006.

[FLB11] T. Frey, P. J. Leek, M. Beck, K. Ensslin, A. Wallraff, and T. Ihn. "Characterization of a microwave frequency resonator via a nearby quantum dot." *Appl. Phys. Lett.*, **98**:262105, 2011.

[FLB12] T. Frey, P. J. Leek, M. Beck, A. Blais, T. Ihn, K. Ensslin, and A. Wallraff. "Dipole Coupling of a Double Quantum Dot to a Microwave Resonator." *Phys. Rev. Lett.*, **108**:046807, 2012.

[FMR85] D. R. Fredkin, M. Montal, and J. A. Rice. *Identification of aggregated Markovian models: appliation to the nicotinic acetylcholine receptor*, volume 1, pp. 269–289. 1985.

[FR86] D. R. Fredkin and J. A. Rice. "On Aggregated Markov Processes." *J. Appl. Prob.*, **23**(1):208–214, 1986.

[FR92] D. R. Fredkin and J. A. Rice. "Maximum likelihood estimation and identification directly from single-channel recordings." *Proc. R. Soc. Lond B*, **249**:125–132, 1992.

[GHW05] J. Gorman, D. G. Hasko, and D. A. Williams. "Charge-Qubit Operation of an Isolated Double Quantum Dot." *Phys. Rev. Lett.*, **95**:090502, Aug 2005.

[GKL04] V. N. Golovach, A. Khaetskii, and D. Loss. "Phonon-Induced Decay of the Electron Spin in Quantum Dots." *Phys. Rev. Lett.*, **93**(1):016601, 2004.

[GLS09] S. Gustavsson, R. Leturcq, M. Studer, I. Shorubalko, T Ihn, K Ensslin, D. C. Driscoll, and A. C. Gossard. "Electron counting in quantum dots." *Surf. Sci. Rep.*, **64**:191–232, 2009.

[GRV00] P. Giudici, T. Ryden, and P. Vandekerkhove. "Likelihoo-Ratio Tests for Hidden Markov Models." *Biometrics*, **56**:742–747, 2000.

[GSF07] S. Goswami, K. A. Slinker, M. Friesen, L. M. McGuire, J. L. Truitt, C. Tahan, L. J. Klein, J. O. Chu, P. M. Mooney, D. W. van der Weide, R. Joynt, S. N. Coppersmith, and M. A. Eriksson. "Controllable valley splitting in silicon quantum devices." *Nat. Phys.*, **3**:41–45, 2007.

[Han05] R. Hanson. *Electron spins in semiconductor quantum dots.* PhD thesis, Technische Universiteit Delft, February 2005.

[Hay12] W. M. Haynes, editor. *CRC Handbook of Chemistry and Physics.* CRC, 92nd edition, 2012.

[HBW07] K. Hennessy, A. Badolato, M. Winger, D. Gerace, M. Atature, S. Gulde, S. Falt, E. L. Hu, and A. Imamoglu. "Quantum nature of a strongly coupled single quantum dot-cavity system." *Nature*, **445**:896–899, 2007.

[HFC03] T. Hayashi, T. Fujisawa, H. D. Cheong, Y. H. Jeong, and Y. Hirayama. "Coherent Manipulation of Electronic States in a Double Quantum Dot." *Phys. Rev. Lett.*, **91**:226804, Nov 2003.

[HKB09] R. R. Hayes, A. A. Kiselev, M. G. Borselli, S. S. Bui, E. T. Croke, P. W. Deelman, B. M. Maune, I. Milosavljevic, J.-S. Moon, R. S. Ross, A. E. Schmitz, M. F. Gyure, and A. T. Hunter. "Lifetime measurements (T1) of electron spins in Si/SiGe quantum dots." *arXiv*, **cond-mat**:0908.0173v1, 2009.

[HKP07] R. Hanson, L. P. Kouwenhoven, J. R. Petta, S. Tarucha, and L. M. K. Vandersypen. "Spins in few-electron quantum dots." *Rev. Mod. Phys.*, **79**(4):1217–1265, Oct 2007.

[HPX11] M. G. House, H. Pan, M. Xiao, and H. W. Jiang. "Non-equilibrium charge stability diagrams of a silicon double quantum dot." *Applied Physics Letters*, **99**(11):112116, 2011.

[HWA08] M. Hofheinz, E. M. Weig, M. Ansmann, R. C. Bialczak, E. Lucero, M. Neely, A. D. O'Connell, H. Wang, J. M. Martinis, and A. N. Cleland. "Generation of Fock states in a superconducting quantum circuit." *Nature*, **454**:310–314, 2008.

[HZJ09] M. G. House, X. C. Zhang, and H. W. Jiang. "Analysis of electron tunneling events with the hidden Markov model." *Phys. Rev. B*, **80**:113308, Sep 2009.

[IAB99] A. Imamoglu, D. D. Awschalom, G. Burkard, D. P. DiVincenzo, D. Loss, M. Sherwin, and A. Small. "Quantum Information Processing Using Quantum Dot Spins and Cavity QED." *Phys. Rev. Lett.*, **83**:4204–4207, Nov 1999.

[IRW01] RB Israel, JS Rosenthal, and JZ Wei. "Finding generators for Markov chains via empirical transition matrices, with applications to credit ratings." *MATHEMATICAL FINANCE*, **11**(2):245–265, APR 2001.

[Jam06] F. James. *Statistical Methods in Experimental Physics*. World Scientific, Singapore, 2nd edition, 2006.

[JMC11] Pei-Qing Jin, Michael Marthaler, Jared H. Cole, Alexander Shnirman, and Gerd Schön. "Lasing and transport in a quantum-dot resonator circuit." *Phys. Rev. B*, **84**:035322, Jul 2011.

[Joh05] A. C. Johnson. *Charge Sensing and Spin Dynamics in GaAs Quantum Dots*. PhD thesis, Massachusetts Institute of Technology, September 2005.

[KAT01] L. P. Kouwenhoven, D. G. Austing, and S. Tarucha. "Few-electron quantum dots." *Rep. Prog. Phys*, **64**:701–736, 2001.

[KBT06] F. H. L. Koppens, C. Buizert, K. J. Tielrooij, I. T. Vink, K. C. Nowack, T. Meunier, L. P. Kouwenhoven, and L. M. K. Vandersypen. "Driven coherent oscillations of a single electron spin in a quantum dot." *Nature*, **442**:766–771, 2006.

[KDW89] K. Kandiah, M. O. Deighton, and F. B. Whiting. "A physical model for random telegraph signal currents in semiconductor devices." *Journal of Applied Physics*, **66**(2):937–948, 1989.

[KGK06] G. Khitrova, H. M. Gibbs, M. Kira, S. W. Koch, and A. Scherer. "Vacuum Rabi splitting in semiconductors." *Nature Physics*, **2**:81–90, 2006.

[Kie89] P. Kienker. "Equivalence of Aggregated Markov Models of Ion-Channel Gating." *Proc. R. Soc. Lond. B*, **236**:269–309, 1989.

[KLV00] Emanuel Knill, Raymond Laflamme, and Lorenza Viola. "Theory of Quantum Error Correction for General Noise." *Phys. Rev. Lett.*, **84**:2525–2528, Mar 2000.

[KMM97] L. P. Kouwenhoven, C. M. Marcus, P. L. McEuen, S. Tarucha, R. M. Westervelt, and N. S. Wingreen. *Electron transport in quantum dots*, pp. 105–214. Kluwer Academic, Dordrecht, 1997.

[KN01] A. V. Khaetskii and Y. V. Nazarov. "Spin-flip transitions between Zeeman sublevels in semiconductor quantum dots." **64**:125316, 2001.

[KOB10] Y. Kubo, F. R. Ong, P. Bertet, D. Vion, V. Jacques, D. Zheng, A. Dréau, J.-F. Roch, A. Auffeves, F. Jelezko, J. Wrachtrup, M. F. Barthe, P. Bergonzo, and D. Esteve. "Strong Coupling of a Spin Ensemble to a Superconducting Resonator." *Phys. Rev. Lett.*, **105**:140502, Sep 2010.

[KR95] R. E. Kass and A. E. Raftery. "Bayes Factors." *J. Amer. Stat. Assoc.*, **90**(430):773–795, 1995.

[LD98] Daniel Loss and David P. DiVincenzo. "Quantum computation with quantum dots." *Phys. Rev. A*, **57**:120–126, Jan 1998.

[Ler92] B.G. Leroux. "Maximum-likelihood estimation for hidden Markov models." *Stochastic Processes and their Applications*, **40**:127–143, 1992.

[LJP03] W. Lu, Z. Ji, L. Pfeiffer, K. W. West, and A. J. Rimberg. "Real-time detection of electron tunneling in a quantum dot." *Nature*, **423**:422–425, 2003.

[LPW91] P. Lafarge, H. Pothier, E. R. Williams, D. Esteve, C. Urbina, and M. H. Devoret. "Direct observation of macroscopic charge quantization." *Z. Phys. B*, **85**:327–332, 1991.

[LTD10] E. A. Laird, J. M. Taylor, D. P. DiVincenzo, C. M. Marcus, M. P. Hanson, and A. C. Gossard. "Coherent spin manipulation in an exchange-only qubit." *Phys. Rev. B*, **82**:075403, Aug 2010.

[LXC11] H. O. Li, M. Xiao, G. Cao, C. Zhou, R. N. Shang, T. Tu, G. C. Guo, H. W. Jiang, and G. P. Guo. "Electron Spin Excited States Spectroscopy in a Quantum Dot Probed by QPC Back-action." *arXiv*, **cond-mat**:1112.2354v1, 2011.

[LXC12] HaiOu Li, Ming Xiao, Gang Cao, Cheng Zhou, RuNan Shang, Tao Tu, Guang-Can Guo, HongWen Jiang, and GuoPing Guo. "Back-action-induced non-equilibrium effect in electron charge counting statistics." *Applied Physics Letters*, **100**(9):092112, 2012.

[LYZ11] W. H. Lim, C. H. Yang, F. A. Zwanenburg, and A. S. Dzurak. "Spin filling of valley-orbit states in a silicon quantum dot." *Nanotechnology*, **22**:335704, 2011.

[Mac02] R. J. MacKay. "Estimating the Order of a Hidden Markov Model." *The Canadian Journal of Statistics*, **30**(4):573–589, 2002.

[MAR07] K. MacLean, S. Amasha, Iuliana P. Radu, D. M. Zumbühl, M. A. Kastner, M. P. Hanson, and A. C. Gossard. "Energy-Dependent Tunneling in a Quantum Dot." *Phys. Rev. Lett.*, **98**:036802, Jan 2007.

[MBH12] B. M. Maune, M. G. Borselli, B. Huang, T. D. Ladd, P. W. Deelman, K. S. Holabird, A. A. Kiselev, I. Alvarado-Rodriguez, R. S. Ross, A. E. Schmitz, M. Sokolich, C. A. Watson, M. F. Gyure, and A. T. Hunter. "Coherent singlet-triplet oscillations in a silicon-based double quantum dot." *Nature*, **481**(7381):344–347, 2012.

[MCG07] J. Majer, J. M. Chow, J. M. Gambetta, J. Koch, B. R. Johnson, J. A. Schreier, L. Frunzio, D. I. Schuster, A. A. Houck, A. Wallraff, A. Blais, M. H. Devoret,

S. M. Girvin, and R. J. Schoelkopf. "Coupling superconducting qubits via a cavity bus." *Nature*, **449**:443–447, 2007.

[Mer07] N. D. Mermin. *Quantum Computer Science: An Introduction.* Cambridge University Press, London, 2007.

[MNB05] R. Miller, T. E. Northup, K. M. Birnbaum, A. D. Boozer, and H. J. Kimble. "Trapped atoms in cavity QED: coupling quantized light and matter." *J. Phys. B: At. Mol. Opt. Phys.*, **38**:S551–S565, 2005.

[MPZ10] A. Morello, J. J. Pla, F. A. Zwanenburg, K. W. Chan, K. Y. Tan, H. Huebl, M. Mottonen, C. D. Nugroho, C. Yang, J. A. van Donkelaar, A. D. C. Alves, D. N. Jamieson, C. C. Escott, L. C. L. Hollenberg, R. G. Clark, and A. S. Dzurak. "Single-shot readout of an electron spin in silicon." *Nature*, **467**:687–691, 2010.

[NC04] M. A. Nielsen and I. L. Chuang. *Quantum Computation and Quantum Information.* Cambridge University Press, London, 2004.

[ND90] John A. Nixon and John H. Davies. "Potential fluctuations in heterostructure devices." *Phys. Rev. B*, **41**:7929–7932, Apr 1990.

[PJT05] J. R. Petta, A. C. Johnson, J. M. Taylor, E. A. Laird, A. Yacoby, M. D. Lukin, C. M. Marcus, M. P. Hanson, and A. C. Gossard. "Coherent Manipulation of Coupled Electron Spins in Semiconductor Quantum Dots." *Science*, **309**(5744):2180–2184, 2005.

[Poz04] D. M. Pozar. *Microwave Engineering.* John Wiley and Sons, Inc., Hoboken, NJ, 3rd ed. edition, 2004.

[PPL10] K. D. Petersson, J. R. Petta, H. Lu, and A. C. Gossard. "Quantum Coherence in a One-Electron Semiconductor Charge Qubit." *Phys. Rev. Lett.*, **105**:246804, Dec 2010.

[QAS00] F. Qin, A. Auerbach, and F. Sachs. "A Direct Optimization Approach to Hidden Markov Modeling for Single Channel Kinetics." *Biophys. J.*, **79**:1915–1927, 2000.

[Rab89] L. R. Rabiner. "A Tutorial on Hidden Markov Models and Selected Applications in Speech Recognition." *Proc. of the IEEE*, **77**(2):257–286, 1989.

[RE08] W. J. J. Roberts and Y. Ephraim. "An EM Algorithm for Ion-Channel Current Estimation." *IEEE Trans. on Sig. Proc.*, **56**(1):26–33, 2008.

[RM02] S. M. Reimann and M. Manninen. "Electronic structure of quantum dots." *Rev. Mod. Phys.*, **74**(4):1283–1342, 2002.

[RSL04] J. P. Reithmaier, G. Sek, A. Loffler, C. Hofmann, S. Kuhn, S. Reitzenstein, L. V. Keldysh, V. D. Kulakovskii, T. L. Reinecke, and A. Forchel. "Strong coupling in a single quantum dot-semiconductor microcavity system." *Nature*, **432**:197–200, 2004.

[Ryd95] Tobias Rydn. "Estimating the Order of Hidden Markov Models." *Statistics*, **26**(4):345–354, 1995.

[SFH05] S. Sasaki, T. Fujisawa, T. Hayashi, and Y. Hirayama. "Electrical Pump-and-Probe Study of Spin Singlet-Triplet Relaxation in a Quantum Dot." *Phys. Rev. Lett.*, **95**:056803, Jul 2005.

[Sho97] P. W. Shor. "Polynomial-Time Algorithms for Prime Factorization and Discrete Logarithms on a Quantum Computer." *SIAM J. Sci. Statist. Comput.*, **26**:1484, 1997.

[SIM99] Mark S. Sherwin, Atac Imamoglu, and Thomas Montroy. "Quantum computation with quantum dots and terahertz cavity quantum electrodynamics." *Phys. Rev. A*, **60**:3508–3514, Nov 1999.

[SJ10] Peter Stano and Philippe Jacquod. "Spin-dependent tunneling into an empty lateral quantum dot." *Phys. Rev. B*, **82**:125309, Sep 2010.

[SPV11] C. B. Simmons, J. R. Prance, B. J. Van Bael, T. S. Koh, Z. Shi, D. E. Savage, M. G. Lagally, R. Joynt, M. Friesen, S. N. Coppersmith, and M. A. Eriksson. "Tunable Spin Loading and T1 of a Silicon Spin Qubit Measured by Single-Shot Readout." *Phys. Rev. Lett.*, **106**:156804, 2011.

[SSP12] Zhan Shi, C. B. Simmons, J. R. Prance, John King Gamble, Teck Seng Koh, Yun-Pil Shim, Xuedong Hu, D. E. Savage, M. G. Lagally, M. A. Eriksson, Mark Friesen, and S. N. Coppersmith. "Fast Hybrid Silicon Double-Quantum-Dot Qubit." *Phys. Rev. Lett.*, **108**:140503, Apr 2012.

[SWK98] R. J. Schoelkopf, P. Wahlgren, A. A. Kozhevnikov, P. Delsing, and D. E. Prober. "The Radio-Frequency Single-Electron Transistor (RF-SET): A Fast and Ultrasensitive Electrometer." *Science*, **280**(5367):1238–1242, 1998.

[Tah05] C. Tahan. *Silicon in the quantum limit: quantum computing and decoherence in silicon architectures*. PhD thesis, University of Wisconsin - Madison, 2005.

[TFJ02] C. Tahan, M. Friesen, and R. Joynt. "Decoherence of electron spin qubits in Si-based quantum computers." **66**:035314, 2002.

[The05] Y.-K. The. *Analysis of Ion Channels with Hidden Markov Models*. PhD thesis, Albert-Ludwigs-Universitat Freiburg im Breisgau, May 2005.

[TJ05] C. Tahan and R. Joynt. "Rashba spin-orbit coupling and spin relaxation in silicon quantum wells." **71**:075315, 2005.

[TL06] J. M. Taylor and M. D. Lukin. "Cavity quantum electrodynamics with semiconductor double-dot molecules on a chip." *arXiv*, **cond-mat**:0605144v1, 2006.

[TMB06] A. M. Tyryshkin, J. J. L. Morton, S. C. Benjamin, A. Ardavan, G. A. D. Briggs, J. W. Ager, and S. A. Lyon. "Coherence of spin qubits in silicon." *J. Phys.: Condens. Matter*, **18**:S783–S794, 2006.

[TZ12] Ted Thorbeck and Neil M. Zimmerman. "Determining the location and cause of unintentional quantum dots in a nanowire." *Journal of Applied Physics*, **111**(6):064309, 2012.

[Vin08] I. Vink. *Manipulation and Read-out of Spins in Quantum Dots*. PhD thesis, Technische Universiteit Delft, November 2008.

[Vis11] Ingmar Visser. "Seven things to remember about hidden Markov models: A tutorial on Markovian models for time series." *Journal of Mathematical Psychology*, **55**(6):403 – 415, 2011.

[Vit67] A. J. Viterbi. "Error bounds for convolutional codes and an asymptotically optimal decoding algorithm." *IEEE Trans. Informat. Theory*, **13**:260–269, 1967.

[VSB01] L. M. K. Vandersypen, M. Steffen, G. Breyta, C. S. Yannoni, M. H. Sherwood, and I. L. Chuang. "Experimental realization of Shor's quantum factoring algorithm using nuclear magnetic resonance." *Nature*, **414**:883–887, 2001.

[Wan08] Z. M. Wang, editor. *Self-Assembled Quantum Dots*. Springer, New York, 2008.

[WC12] Y. Wu and D. Culcer. "Coherent electrical rotations of valley states in Si quantum dots using the phase of the valley-orbit coupling." *arXiv*, **cond-mat**:1204.2267v1, 2012.

[WCM10] W. M. Witzel, M. S. Carroll, A. Morello, L. Cywinski, and S. Das Sarma. "Electron Spin Decoherence in Isotope-Enriched Silicon." *Phys. Rev. Lett.*, **105**:187602, 2010.

[WDE02] W. G. van der Wiel, S. De Franceschi, J. M. Elzerman, T. Fujisawa, S. Tarucha, and L. P. Kouwenhoven. "Electron transport through double quantum dots." *Rev. Mod. Phys.*, **75**(1):1–22, Dec 2002.

[Wei88] M. B. Weissman. "$\frac{1}{f}$ noise and other slow, nonexponential kinetics in condensed matter." *Rev. Mod. Phys.*, **60**:537–571, Apr 1988.

[WHB88] B. J. van Wees, H. van Houten, C. W. J. Beenakker, J. G. Williamson, L. P. Kouwenhoven, D. van der Marel, and C. T. Foxon. "Quantized Conductance of Point Contacts in a Two-Dimensional Electron Gas." *Phys. Rev. Lett.*, **60**(9):848–850, 1988.

[WHH05] Yue-Min Wan, Kuo-Dong Huang, S. F. Hu, C. L. Sung, and Y. C. Chou. "Coulomb blockade oscillations in ultrathin gate oxide silicon single-electron transistors." *Journal of Applied Physics*, **97**(11):116106, 2005.

[WHM06] J. B. Wang, C. Hines, and R. D. Muhandiramge. *Electronic Structure of Quantum Dots*, pp. 545–604. American Scientific Publishers, 2006.

[WM08] D. F. Walls and G. J. Milburn. *Quantum Optics*. Springer-Verlag, Berlin, 2nd ed. edition, 2008.

[WP99a] Peiming Wang and Martin L. Puterman. "Markov Poisson regression models for discrete time series. Part 1: Methodology." *Journal of Applied Statistics*, **26**(7):855–869, 1999.

[WP99b] Peiming Wang and Martin L. Puterman. "Markov Poisson regression models for discrete time series. Part 2: Applications." *Journal of Applied Statistics*, **26**(7):871–882, 1999.

[WSB04] A. Wallraff, D. I. Schuster, A. Blais, L. Frunzio, R.-S. Huang, J. Majer, S. Kumar, S. M Girvin, and R. J. Schoelkopf. "Strong coupling of a single photon to a superconducting qubit using circuit quantum electrodynamics." *Nature*, **431**:162–167, 2004.

[WVE06] Herbert Walther, Benjamin T H Varcoe, Berthold-Georg Englert, and Thomas Becker. "Cavity quantum electrodynamics." *Reports on Progress in Physics*, **69**(5):1325, 2006.

[XHJ10a] M. Xiao, M. G. House, and H. W. Jiang. "Measurement of the Spin Relaxation Time of Single Electrons in a Silicon Metal-Oxide-Semiconductor-Based Quantum Dot." *Phys. Rev. Lett.*, **104**:096801, Mar 2010.

[XHJ10b] M. Xiao, M. G. House, and H. W. Jiang. "Parallel spin filling and energy spectroscopy in few-electron Si metal-on-semiconductor-based quantum dots." *Appl. Phys. Lett.*, **97**:032103, 2010.

[YSH04] T. Yoshie, A. Scherer, J. Hendrickson, G. Khitrova, H. M. Gibbs, G. Rupper, C. Ell, O. B. Schekin, and D. G. Deppe. "Vacuum Rabi splitting with a single quantum dot in a photonic crystal nanocavity." *Nature*, **432**:200–203, 2004.

[YYJ00] Y. Yuzhelevski, M. Yuzhelevski, and G. Jung. "Random telegraph noise analysis in time domain." *Rev. Sci. Instrum.*, **71**(4):1681–1688, 2000.

[ZHF01] Neil M. Zimmerman, William H. Huber, Akira Fujiwara, and Yasuo Takahashi. "Excellent charge offset stability in a Si-based single-electron tunneling transistor." *Applied Physics Letters*, **79**(19):3188–3190, 2001.

[ZHS08] Neil M. Zimmerman, William H. Huber, Brian Simonds, Emmanouel Hourdakis, Akira Fujiwara, Yukinori Ono, Yasuo Takahashi, Hiroshi Inokawa, Miha Furlan, and Mark W. Keller. "Why the long-term charge offset drift in Si single-electron tunneling transistors is much smaller (better) than in metal-based ones: Two-level fluctuator stability." *Journal of Applied Physics*, **104**(3):033710, 2008.

[ZMB09] X. C. Zhang, G. Mazzeo, A. Brataas, M. Xiao, E. Yablonovitch, and H. W. Jiang. "Tunable electron counting statistics in a quantum dot at thermal equilibrium." **80**:035321, 2009.